Progress in Materials Science 101 (2019) 46–89

Contents lists available at ScienceDirect

Progress in Materials Science

journal homepage: www.elsevier.com/locate/pmatsci

Redox-electrolytes for non-flow electrochemical energy storage: A critical review and best practice

Juhan Lee[a,b], Pattarachai Srimuk[a,b], Simon Fleischmann[a,b], Xiao Su[c], T. Alan Hatton[c], Volker Presser[a,b,*]

[a] INM – Leibniz Institute for New Materials, 66123 Saarbrücken, Germany
[b] Saarland University, 66123 Saarbrücken, Germany
[c] Department of Chemical Engineering, Massachusetts Institute of Technology, Cambridge, USA

ARTICLE INFO

Keywords:
Redox electrolyte
Electrochemical energy storage
Hybrid energy storage
Supercapacitors
Batteries

ABSTRACT

Over recent decades, a new type of electric energy storage system has emerged with the principle that the electric charge can be stored not only at the interface between the electrode and the electrolyte but also in the bulk electrolyte by redox activities of the electrolyte itself. Those redox electrolytes are promising for non-flow hybrid energy storage systems, or redox electrolyte-aided hybrid energy storage (REHES) systems; particularly, when they are combined with highly porous carbon electrodes. In this review paper, critical design considerations for the REHES systems are discussed as well as the effective electrochemical characterization techniques. Appropriate evaluation of the electrochemical performance is discussed thoroughly, including advanced analytical techniques for the determination of the electrochemical stability of the redox electrolytes and self-discharge rate. Additionally, critical summary tables for the recent progress on REHES systems are provided. Furthermore, the unique synergistic combination of porous carbon materials and redox electrolytes is introduced in terms of the diffusion, adsorption, and electrochemical kinetics modulating energy storage in REHES systems.

1. Introduction

Electrochemical energy storage (EES) devices are becoming increasingly important in our daily life. They are applied in small devices such as laptops, tablets, and cell phones, and in larger devices like electric cars to provide efficient and reliable use of energy [1]. Furthermore, EES systems are deemed key technologies for large-scale energy storage to stabilize the power supply of future grids which rely heavily on energy produced from renewable sources, such as solar and wind energy [2–4]. Batteries are one of the most popular EES types and are applied broadly in the world. Through redox reactions at the positive and negative electrodes, either by conversion-type or insertion/intercalation type reactions, batteries provide a stable operating potential with high specific charge storage capacity [5]. State-of-the-art intercalation-type lithium-ion batteries, for instance, offer a nominal cell voltage of 3.6 V with a specific energy of 20–150 Wh/kg (normalized by the device mass) [4,6–8]. The main disadvantages of batteries are the long charging time due to their intrinsically low power handling capability (< 1 kW/kg, normalized by the device mass) and short device cycle life [9–11]. Intensive research activities have increased the specific power of modern batteries; however, the cost of these advanced batteries is high, and they still do not fulfill the power demands of many applications (especially regarding electric vehicles). For energy storage applications requiring high specific power, supercapacitors are more attractive with values typically > 10 kW/kg

* Corresponding author at: INM – Leibniz Institute for New Materials, 66123 Saarbrücken, Germany.
E-mail address: volker.presser@leibniz-inm.de (V. Presser).

https://doi.org/10.1016/j.pmatsci.2018.10.005
Received 21 April 2018; Accepted 28 October 2018
Available online 30 October 2018
0079-6425/ © 2018 The Author(s). Published by Elsevier Ltd. This is an open access article under the CC BY license (http://creativecommons.org/licenses/BY/4.0/).

Nomenclature

Symbols

A	area of the planar electrode in cm^2
a_{Ox}	activity of oxidized species in the electrolyte
a_{Re}	activity of reduced species in the electrolyte
C	capacitance in F
C_c	device specific capacitance in F/g
$C_{\varnothing}$	potential-dependent capacitance in F
c	concentration in mol/cm^3
c_0	initial molar concentration for the impurity redox reaction in mol/cm^3
c_R	molar concentration of the diffusible redox species in mol/cm^3
D	diffusion coefficient in cm^2/s
E_{char}	energy invested during charging
E_{dis}	energy restored during discharge
E_s	specific energy in Wh/kg
F	Faraday constant (96,485.33 C/mol)
i_0	exchange current density in A/cm^2
i_{Diff}	diffusion-limited redox current in cyclic voltammetry
i_{EDL}	current from the double-layer formation in cyclic voltammetry
i_p	redox peak current
i_s	leakage current
i_{TLE}	redox current under thin layer condition in cyclic voltammetry
l	distance from the electrode surface in cm
m_a	mass of the active electrodes in the device
m_b	mass of the electrode and the electrolyte
m_c	mass of the electrode, electrolyte, and separator
m_e	mass of the total electrode mass
n	electron transfer number
n_0	number of electrons transferred before the rate handling step
P_s	specific power in kW/kg
Q	accumulated electric charge during the cell operation
Q_a	charge accumulated due to the anodic current
Q_c	charge accumulated due to the cathodic current
q_1	charge for the formation or desorption of a monolayer of the intermediate
R	universal gas constant (8.31 J/K·mol)
R_s	short-circuiting resistance element in Ohm
S_a	S-value for the anodic limit
S_c	S-value for the cathodic limit
T	temperature in Kelvin
t_{dis}	discharging time
t_0	integration constant
U_t	volume of the thin layer in cm^3
U_c	volume of the electrode, electrolyte, and separator
V_a	applied potential
V_c	cell voltage
V_i	initial potential
V_t	time-dependent open-circuit potential
v	scan rate in V/s
x	the charge state of the redox species
$[Ox]$	concentration of the oxidized species at the electrode surface
$[Re]$	concentration of the reduced species at the electrode surface
α	transfer coefficient
Γ	fractional surface coverage
$\Delta\varphi_p$	peak-to-peak separation determined by cyclic voltammetry
ε_E	energy efficiency
η	overpotential
θ	areal fractional coverage
φ_0	standard electrode potential
φ_e	potential of the half-cell
φ_f	formal redox potential
φ_{V0}	electrode potential at cell potential of zero
φ_+	potential of the positive electrode
φ_-	potential of the negative electrode

Abbreviations

[EMIm]BF_4	1-ethyl-3-methylimidazolium tetrafluoroborate
[EMIm]Br	1-ethyl-3-methylimidazolium bromide
[FcNTf]	ferrocenylsulfonyl-(trifluoromethylsulfonyl)-imide
[TEA]TFSI	triethylammonium bis(trifluoromethane)sulfonimid
AC	activated carbon
ACF	activated carbon fiber
AEM	anion exchange membrane
AN	acetonitrile
AQ	anthraquinone
AQDS	anthraquinone-2,7-disulphonate
BET	Brunauer-Emmett-Teller
BQ	benzoquinone
CB	carbon black
CC	carbon cloth
CEM	cation exchange membrane
CF	carbon fiber
CFP	carbon fiber paper
CNT	carbon nanotubes
CV	cyclic voltammogram
CWT	conductive woven textile
DCA	deoxycholic acid
DMG	dimethylglyoxime
DN	diamond network
EDL	electrical double-layer
EDLC	electrical double-layer capacitor
EES	electric energy storage
EIS	electrochemical impedance spectroscopy
ESR	equivalent series resistance
EV	ethyl viologen
GCPL	galvanostatic cycling with potential limitation
GHG	graphene hydrogel
GITT	galvanostatic intermittent titration technique
GNS	graphene-supported nanosheet
GP	graphite
HER	hydrogen evolution reaction
HQ	hydroquinone
$HVBr_2$	1,1′-diheptyl-4,4′-bipyridinium dibromide
IHP	inner Helmholtz layer
IL	ionic liquid
ISM	ion selective membranes

LDH	layered double hydroxide	PNA	*p*-nitroaniline
LTO	lithium titanate	PPD	*p*-phenylenediamine
MC	microporous carbon (i.e., pores <2 nm)	PS	porous separator
MGP	modified graphite	Q	quinone
MPD	*m*-phenylenediamine	REHES	redox electrolyte-aided hybrid energy storage
MWCNT	multi-walled carbon nanotubes	RGO	reduced graphene oxide
NMC	nitrogen-doped microporous carbon	SPANI	sulfonated polyaniline
OCP	open-circuit potential	SPD	selective permeability diaphragm
OER	oxygen evolution reaction	SPM	semi-permeable membrane
OHP	outer Helmholtz layer	SSA	specific surface area
PANI	polyaniline	TEG	thermally exfoliated graphene
PCMS	porous carbon micro-sphere	TEMPO	2,2,6,6-tetramethyl-piperidinyl-1-oxyl
PEB	polyaniline emeraldine-base	TLE	thin-layer electrochemistry
PEM	proton exchange membrane	TPAB	tetrapropylammonium bromide
PFC	potassium ferricyanide	TPAI	tetrapropylammonium iodide

when normalized by the device mass [12]. In general, they provide high cyclic stability ($>10{,}000$ cycles), but the low energy storage capacity (<10 Wh/kg, normalized by the device mass) is a severe limitation of these supercapacitive systems [12]. According to the charge storage mechanism and device configuration, supercapacitors can be differentiated either as electrical double-layer capacitors (EDLC), pseudocapacitors, or corresponding hybrids thereof.

The different performance of EES systems originates from different charge storage mechanisms. In principle, four different mechanisms can be identified, as shown schematically in Fig. 1A (after Ref. [13]): (i) electrical double-layer (EDL) formation, (ii) bulk redox reaction of the electrode, (iii) redox reaction near the electrode surface, and (iv) redox activity of the bulk electrolyte. EDL formation is the dominant operational principle for the electrical double-layer capacitor (EDLC, Fig. 2A), which is the most common type of supercapacitor. When the electrode is charged, oppositely charged ions are adsorbed on the electrode surface to balance the charge while the ions are released during discharge (Fig. 1A, type-i mechanism). This fast, electrostatic sorption of dissolved ions allows high power handling performance of EDLCs since it occurs without chemical reactions or solid-state diffusion. Accordingly, EDL formation is a non-Faradaic process, which means it does not involve an electron transfer process from the electrode to the electrolyte (or

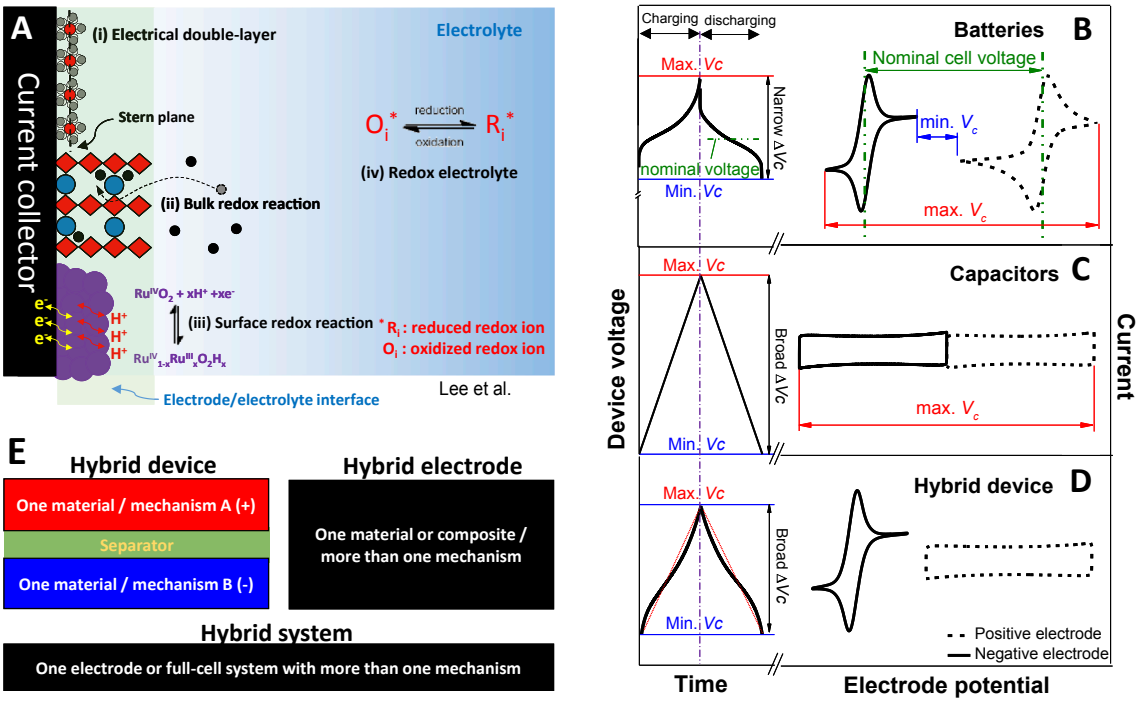

Fig. 1. Charge storage mechanisms for electric energy storage (EES) devices and the types of EES devices with their characteristic electrochemical behavior. (A) Schematic descriptions of the four major mechanisms: the electrical double-layer formation, the bulk redox reaction, the surface near redox reaction, and the redox activity of the electrolyte. Adapted from Ref. [13]. Published by the Royal Society of Chemistry. (B–D) Cyclic voltammograms of various materials and galvanostatic charging/discharge curves of various devices. (E) The definitions for hybrid devices, hybrid electrodes, and hybrid systems.

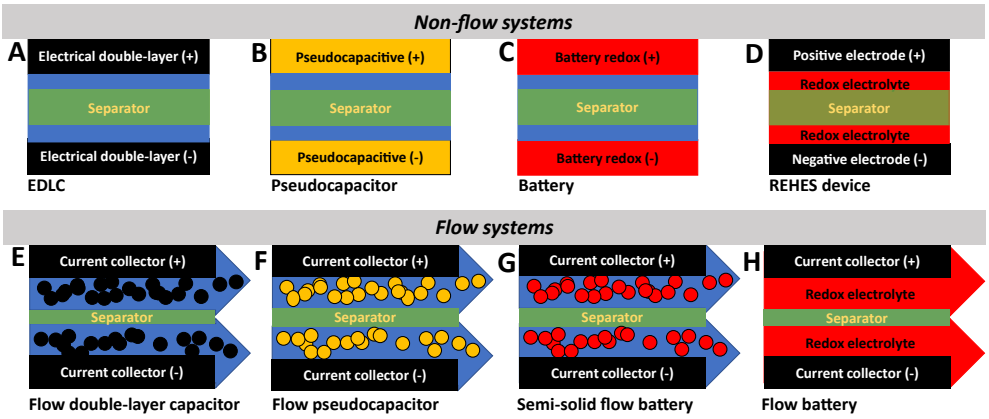

Fig. 2. Device configurations of selected electric energy storage (EES) systems under flow and non-flow condition: (A) electrical double-layer capacitor (EDLC), (B) pseudocapacitor, (C) battery, (D) redox electrolyte-aided hybrid energy storage (REHES) device, (E) flow double-layer capacitor, (F) flow pseudocapacitor, (G) semi-solid flow battery, and (H) flow battery.

in reverse) during energy storage and recovery. Since the ion sorption process does not involve significant structural changes of the electrode materials (in the ideal case), high cyclic stability can be achieved. By contrast, batteries (Fig. 2C) employ Faradaic reactions of the bulk electrode material which can be of the conversion or insertion/intercalation type (Fig. 1A, type-ii mechanism). For instance, lithium-ion batteries store energy by the insertion or intercalation of lithium ions into the bulk electrode material. The structural changes of the bulk electrode material through the insertion/intercalation process builds up fatigue and degradation over time; therefore, the cyclic stability of the EES device based on the bulk redox reaction of the electrode material is limited.

When a Faradaic reaction occurs only near the electrode surface (Fig. 1A, type-iii mechanism), the reaction is less diffusion-controlled but more surface-controlled which leads to fast redox reactions [14]. These reactions can be either (i) underpotential deposition or (ii) Faradaic adsorption of ions near the surface of the material. In the case of underpotential deposition, a metal is deposited on a second metal in a process that requires less energy (underpotential) than the redox potential of the metal for deposition; an example is the underpotential deposition of lead on gold [15]. In the case of hydrous RuO_2 in aqueous solution, a proton can be adsorbed Faradaically near the surface of the electrode [16]. Despite its Faradaic reaction origin, the hydrous RuO_2 material exhibits a capacitor-like behavior [17]. For this reason, this type of electrode materials is classified as *intrinsically* pseudocapacitive [14,18]. The capacitor-like features can also be observed with electrodes with bulk redox reactions when the size of the reaction layer in the electrode is reduced to the nanometer range. These materials can be classified as *extrinsically* pseudocapacitive materials [18,19]. When pseudocapacitive materials are used to build a device, the device is classified as a pseudocapacitor (Fig. 2B).

Unlike the three charge storage mechanisms described above, the charge storage capacity of the bulk redox electrolyte system is not limited by the electrode/electrolyte interface (Fig. 1A, type-iv mechanism). After electron transfer from the electrode to the redox active ions dissolved in the electrolyte, the ions diffuse away from the fluid/solid interface and back to the bulk electrolyte volume. Thereby, the oxidation state of the electrolyte changes. Redox flow batteries (Fig. 2H) rely on this charge storage mechanism. Their main advantage is that the redox electrolyte can be stored separately in a scalable reservoir after charging in the cell with the aid of pumping devices [20–22]. Thus, facile scalability is enabled by adjusting the number of cell stacks and the size of the electrolyte reservoir to adjust the power and the energy storage capacity of the system, respectively [20]. The main drawback of redox flow batteries is the lower specific energy relative to that of modern batteries and the lower specific power compared to that of supercapacitors [23]. Nonetheless, redox flow battery technologies have been employed for large-scale energy storage in grid-level applications since volume and size of the individual devices are less of a concern [24].

Functionally, EES devices can be classified into capacitors, batteries, and their hybrids [25]. For instance, a battery device (Fig. 1B) provides stable operating cell voltage (reported as the nominal cell voltage) due to the strong bulk redox activities at the positive and negative electrodes. The redox activities of battery materials can be seen in cyclic voltammograms (CV) as characterized by reduction and oxidation peaks (Fig. 1B, *right*). During charging of a battery, the negative electrode is reduced while the positive electrode is oxidized. The potential difference between the two electrodes corresponds to the device potential, or cell voltage (Fig. 1B, *left*). In the case of an ideal capacitor (Fig. 1C), the device exhibits a linear relationship between the cell voltage and the accumulated charge which corresponds to a potential-independent, constant current response in CVs. Therefore, for capacitors and capacitor-like devices, it is reasonable to report the charge storage capacity as a capacitance (F) which is the slope of the voltage and the accumulated charge profile [9,12]. Along with the capacitance value, a relatively broad cell voltage window ($\Delta V > 0.8$ V) can be used for a capacitor device relative to the narrow operating cell voltages typical of battery devices [26].

For the continuing development of EES systems, key target parameters are: (i) high specific energy, (ii) high specific power, (iii) long cycle life, (iv) low cost, and (v) environmental friendliness. For that, the most recent research activities have focused on the developments of nano-engineered materials for batteries and supercapacitors [1,4,27,28]. As an alternative solution, hybrid devices provide desired specific power and energy by combining two different negative and positive electrode materials with different charge storage mechanisms (Fig. 1E). For instance, a lithium-ion capacitor combines a porous carbon positive electrode and a negative electrode with battery-type redox reaction (i.e., insertion, intercalation, or conversion reaction) [29]. The cell voltage of lithium-ion

capacitors is mostly controlled by the capacitive potential change at the positive electrode, while the negative battery electrode operates only within a narrow potential range (Fig. 1D). In this case, the galvanostatic (constant current) potential profile exhibits a linear-like feature. Because of this nearly linear correlation between voltage and charge, the system can be called capacitor-like.

Hybridization can also be realized at the electrode level instead of the device level. A hybrid electrode (Fig. 1E) may consist of a homogeneous material or inhomogeneous mixture material (composite) to capitalize on more than one charge storage mechanism. For instance, a composite of porous carbon and a battery material such as lithium titanium oxide (LTO) yields, in regards to performance, a hybrid electrode which shows the characteristics of both batteries and capacitors [30,31]. In contrast, a composite of LTO and a conductive additive is not considered to be a hybrid electrode since it relies mostly on just one charge storage mechanism (lithium intercalation).

For a clear distinction, in this review paper, a hybrid *device* is defined as a device consisting of one electrode material with a certain charge storage mechanism and a second electrode material with different charge storage mechanism (Fig. 1E). Further, we define a hybrid *system* as consisting of one electrode or of a full-cell (device) containing more than single charge storage mechanism. Hence, the term *hybrid system* can be applied to both a single hybrid electrode and a hybrid device. For instance, a hybrid electrode of LTO and microporous carbon (MC) and a hybrid device with an LTO-MC hybrid electrode and graphite negative electrode can be both seen as hybrid systems. Hybrid systems with hybrid electrodes exhibit a more complicated electrochemical behavior than do hybrid devices. While lithium-ion capacitors (hybrid device) show a capacitor-like behavior, graphite|LTO-MC hybrid systems exhibit both capacitor-like and battery-like regimes over different potential ranges due to the hybridized feature of the LTO-MC electrode [30].

Various new types of hybrid systems have been introduced over the past few decades, and new EES systems have emerged based on flowable electrodes/electrolytes for batteries and supercapacitors (Fig. 2E–G). On the one hand, semi-solid flow batteries and flow capacitors share features with redox flow batteries in that the active electrode materials are not confined to the cell but can be pumped through the cell. On the other hand, semi-solid flow batteries and flow capacitors differ from redox flow batteries in the physical state of the active material. For redox flow batteries, the active materials are liquid, while dispersed phases such as slurries or suspensions are used in semi-solid flow batteries and flow capacitors. Depending on the origin of the charge storage mechanism, flow capacitors can be further classified either as flow double-layer capacitors [32,33] or flow pseudocapacitors [34]. Critical issues for slurry- or suspension-based flow EES systems are the high resistance of the cell due to particle-particle contact resistance, membrane contamination by carbon particles, and reduction of pumping energy [32,35].

Among other hybrid systems, non-flow redox electrolyte-aided hybrid energy storage (REHES) systems are particularly promising for next-generation EES technologies [12,25,36–38]. Most hybrid systems focus on the mixing of two different materials, or on the coupling of electrodes with different charge storage mechanisms at the electrode/electrolyte interface. REHES systems extend the concept of hybridization by adding charge storage capacity beyond the electrode/electrolyte interface through the redox activity of the electrolyte [36]. To enable the redox activity of the electrolyte, the only requirement is an electrically conductive electrode to accomplish the electron transfer between the electrode and electrolyte (Fig. 2D). Therefore, REHES can be used in different EES systems as, for example, in battery systems or with porous carbon electrodes (EDLC).

Once a redox electrolyte has been hybridized with another EES system, the total charge storage capacity is the sum of both charge storage mechanisms. For instance, when a redox electrolyte containing potassium ferricyanide (PFC) is combined with a symmetric (MC|MC) electrical double-layer capacitor (Fig. 3A), the system exhibits characteristics of both redox reaction of PFC (a current peak pair) and EDL formation (a rectangular shape current response) [39]. The latter occurs by the reversible adsorption and desorption of cations (potassium) at the negative electrode and anions (ferrocyanide/ferricyanide) at the positive electrode during cell charging and discharge.

Fig. 3B illustrates schematically the adsorption of ferrocyanide at the positive electrode during cell charging. When the redox potential is reached, the electrons are transferred from the electrolyte to the MC electrode, and ferrocyanide is oxidized to ferricyanide. Since the oxidized ferricyanide can diffuse to the bulk electrolyte, the charge storage capacity of the system has contributions not only due to EDL formation at the electrode/electrolyte interface, but also from the bulk electrolyte beyond the interface. The latter is effectively enabled by the high pore volume of the MC electrode. By contrast, the charge storage capacity of

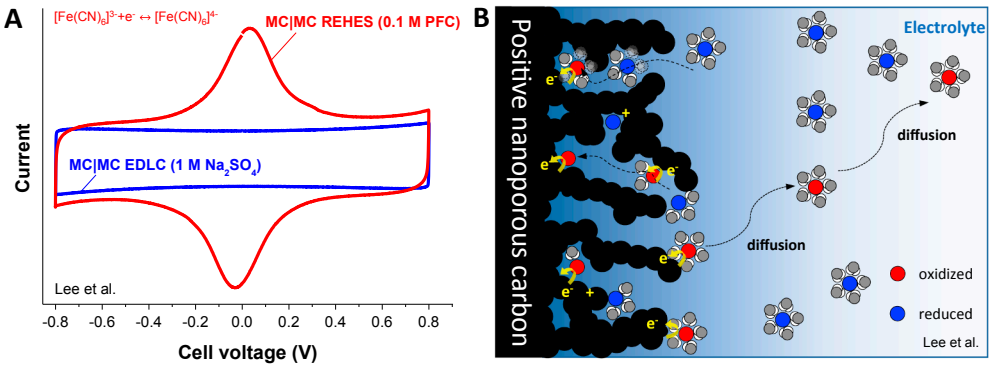

Fig. 3. Working principles of the redox electrolyte-aided hybrid energy storage systems. Adapted with permission from Ref. [39]. Copyright (2017) American Chemical Society. (A) Cyclic voltammograms of the symmetric microporous carbon electrodes (MC|MC) systems in potassium ferricyanide (PFC) and sodium sulfate aqueous solutions. (B) Schematic illustration of the working principles of the redox electrolyte-aided hybrid energy storage system with a porous carbon electrode.

conventional hybrid electrodes like LTO-MC electrodes is limited by the electrode/electrolyte interface. For instance, when the battery-like feature is intensified by increases in the relative amount of LTO, the capacitor-like feature is decreased because of the reduced portion of MC of the hybrid electrode [40,41].

The use of MC electrodes for REHES systems is beneficial not only in providing a reservoir for the redox electrolyte, but also for effective charge transfer [27,39,42]. First, the large specific surface area of MC provides a high number of active sites for the electron transfer reactions at the electrode/electrolyte interface. Second, the redox reactions of the electrolyte occur in the confined space of carbon micropores. Thus, in contrast to conventional electrochemistry on flat electrodes, the REHES systems with MC exhibit electrochemical kinetics for the reaction of the redox electrolyte in carbon micropores without diffusion limitations [43]. Such diffusion-less kinetics are essential for fast reactions during cell charging and discharge. In virtue of the unique redox kinetics of the electrolyte in carbon micropores, REHES systems with MC electrodes not only provide enhanced specific energy (up to ca. 200 Wh/kg, normalized by the electrode mass), but also high specific power (>1 kW/kg, normalized by the electrode mass) [13,43–46]. This particular high power performance distinguishes REHES systems from redox flow batteries. For the latter systems, instead of confinement in micropores, redox electrolytes are preferably circulated through meso-/macropores under flow conditions in the cell [22]. Without confinement of the redox electrolyte, costly ion exchange membranes would be required to prevent the redox shuttling phenomenon. Furthermore, REHES systems are less limited than redox flow batteries in application since pumping devices and reservoirs with their space requirements are not necessary. Additionally, REHES systems may provide robust cyclic stability similar to that observed with EDLCs when the applied redox electrolyte is electrochemically stable over the operating cell voltage window [39,44].

One of the essential features of the REHES systems is the charge storage capacity beyond that of the electrode/electrolyte interface by redox reactions of the bulk electrolyte. Therefore, we propose the following definition of REHES systems:

> *REHES is a non-flow hybrid system, where charge storage is accomplished both by the electrode material and the redox electrolyte. The oxidation state of the latter changes in the liquid phase through electron transfer between the electrode and electrolyte.*

According to this definition, deposition-type transition metal redox couples should not be classified as REHES systems. For instance, there is no significant change in the oxidation state of the zinc-containing electrolyte in the Zn(s)/Zn^{2+} redox couple when applied at the negative electrode (only a small change of the formal potential following a change in concentration of dissolved zinc is observed). Therefore, the energy storage capacity is limited by the electrode/electrolyte interface, where the boundary of the interface changes during the reaction through the deposition/dissolution of zinc. For that reason, unlike other redox flow batteries, the capacity of zinc bromide flow batteries is limited by the cell volume at the negative electrode where deposited zinc can be confined.

Following the above definition, the first REHES system reported in the literature is the zinc iodide battery described by Yamamoto in 1981 [47]. This work focused on polymer-iodine adducts for the positive electrode with a ZnI_2 electrolyte for primary batteries [47–49]. Additionally, the MgI_2 electrolyte was investigated for secondary batteries [47]. Later, in 1984, Yamamoto et al. investigated the Zn|ZnI_2|polymer system in more detail with a focus on its performance as a secondary battery [50]. The latter work avoided redox shuttling of iodides by use of a cation exchange membrane (CEM) in the cell. Thereby, the oxidation state of iodide in the electrolyte changes only at the positive electrode compartment during cell charging and discharge, while the oxidation state of zinc in the electrolyte is always Zn^{2+}.

$$\text{Anode: } I_3^- + 2e^- \leftrightarrow 3I^-, \quad \varphi_0 = +0.536 \text{ V vs SHE} \tag{1}$$

$$\text{Cathode: } Zn \leftrightarrow Zn^{2+} + 2e^-, \quad \varphi_0 = -0.763 \text{ V vs SHE} \tag{2}$$

$$\text{Overall: } I_3^- + Zn \leftrightarrow 3I^- + Zn^{2+}, \quad V_c = 1.299 \text{ V} \tag{3}$$

where φ_0 is the standard electrode potential, and V_c is the cell voltage.

Based on the change in the oxidation state of iodide in the electrolyte, the Zn|ZnI_2|polymer system can be classified as REHES. Polyaniline electrodes for polymer-based REHES have been further investigated by Mengoli et al. who compared zinc iodide and zinc bromide electrolytes [51–53]. The zinc halide systems were benchmarked for different positive electrode materials, such as conducting clay/porous carbon composite [54], polyethers [55], 6-nylon [55], polyacrylamide-carbon composite [56], and ferrocene-deoxycholic acid-based inclusion compounds [57]. The zinc halide REHES works from 1981 to 1993 focused on the use of polymer-based electrodes; the latter have significant drawbacks due to poor cycle life and high resistance as compared to carbon-based electrodes [43,58,59].

After a 14 -year hiatus, the first REHES work published after 1993 was a 2007 study based on highly porous carbon electrodes (BET specific surface area $> 2500\ m^2/g$) in which a Fe^{2+}/Fe^{3+} redox electrolyte was combined with Cu(s)/Cu^{2+} redox reactions [60]. The application of porous carbon re-energized the REHES research; follow-up works revisited the earlier halide systems [61,62] and explored new systems, such as the hydroquinone/quinone (HQ/Q) redox couple [63,64], vanadium complexes [13,45,46], and ferrocyanide/ferricyanide [39,65,66]. The choice of the electrolytes has also been extended from aqueous to non-aqueous systems, including organic solutions and ionic liquids (IL). In 2009, Tachibana et al. reported an organic REHES system (propylene carbonate and γ-butyrolactone) containing redox active N,N′-diphenyl-phenylene-diamine [67]. In 2010, Sun et al. introduced a REHES system with copper-containing IL where the oxidation state of the copper in the IL changes from Cu^+/Cu^{2+} [68].

In the following, Section 2 will discuss the distinctive features of batteries, capacitors, and hybrid devices including the appropriate terminologies for REHES systems. Next, critical design considerations are given in Section 3. In Section 4, electrochemical characterization techniques will be discussed which are particularly useful for the REHES research. In Section 5, a broad summary of recent research activity will be given for both aqueous and non-aqueous REHES systems, particularly, with the perspectives on electrochemical kinetics, diffusion, and adsorption of the redox ions. Finally, Section 6 concludes with a summary and provides an outlook for future developments in this field.

2. Distinctions between batteries, capacitors, and hybrids

Fundamentally, a cathode is the electrode at which a chemical reduction occurs, while at the anode, oxidation is encountered. Therefore, the fundamental definition of cathode and anode is according to the direction of electron flow in the system. For instance, electrolysis is a non-spontaneous reaction that requires an energy input or electric charging process. Once the cell is being charged, oxidation occurs at one positively polarized electrode (anode, electrons flow out) while reduction occurs at the one negatively polarized electrode (cathode, electrons flow in). Since this charging process is of importance for the products of the electrolysis process, the cathode and anode assignments are made during the charging process for notation. Historically, research on batteries started with primary batteries, where the reaction is spontaneous during cell discharge. For that reason, the cathode and the anode are defined based on the discharging process. Thus, the cathodic reaction occurs at the positively polarized electrode, while the anodic reaction occurs at the negatively polarized electrode. However, the direction of electrons during discharge is opposite that of the non-spontaneous reaction of electrolysis. Following the development of the secondary batteries, this nomenclature remained unchanged even though the cathode, in fact, becomes anode and anode becomes the cathode during the charging process when applying the primary definition for the electrode assignment.

An issue arises in the case of electrical double-layer capacitors where energy storage is accomplished by the reversible electrosorption of ions without chemical reduction or oxidation. Furthermore, the terminology of cathode and anode becomes problematic when describing energy storage systems during charging, because the terminology was initially based on the discharge process. Therefore, in this review paper, we use the terms “positive electrode” and “negative electrode” to describe the positively polarized electrode (the conventional cathode for a battery system) and negatively polarized electrode (the conventional anode for a battery system). For the description of the fundamental electrochemistry, the term anodic and cathodic will be still used to express the oxidation and reduction, respectively.

Capitalizing on Faradaic reactions of the electrolyte, REHES devices often exhibit battery-like features as evidenced by redox peaks during electrochemical voltage sweeping. The identification of battery-like or capacitor-like behavior is vital for clear target applications and data comparison. In many cases, battery-like systems are treated as a capacitive device [25,69–71]. However, clear differentiation between battery-like and capacitor-like behavior may be complicated due to the following reasons:

(i) The system behavior depends on the applied potential window.
(ii) No clear quantitative criteria have been established for linearity of the capacitor-like system.

The electrochemical behavior of REHES systems depends on the applied cell voltage window and may vary over different ranges. For instance, with bromide and viologen-based redox electrolytes combined with highly porous activated carbon (AC) electrodes (Fig. 4A) [71], a capacitive regime can be seen over a low cell voltage range (0–1 V), while a strong potential plateau occurs at around 1.2 V. Thus, if the

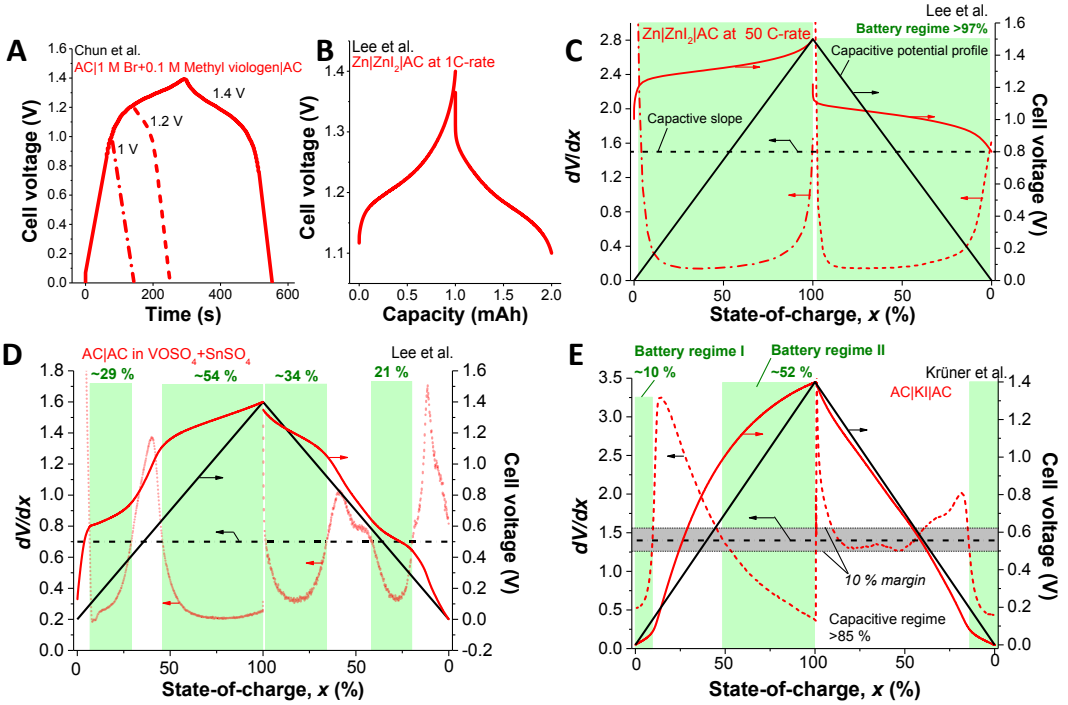

Fig. 4. Galvanostatic profiles of AC|AC in KBr + methyl viologen dichloride ($MVCl_2$) system reported from Ref. [71](A) and Zn|ZnI_2|AC system from Ref. [43] (B). Derivative analysis (dV/dx) for Zn|ZnI_2|AC system from Ref. [43] (C), AC|AC in $VOSO_4$ + $SnSO_4$ system from Ref. [13] (D), and AC|KI|AC system from Ref. [44] (E). Red dotted lines indicate the derivative values, red solid lines represent the cell voltage of each system. The black dotted line is a derivative for a capacitive system in case of 1.4 V voltage window.

device operates only at 0–1 V, it will appear as a capacitor, while characterization over the range 1.0–1.4 V shows that the device is a battery. In this regard, clear criteria must be mentioned according to the electrochemical features of REHES devices. For instance, the device (Fig. 4A) should be operated in the potential window from 0- to 1 V for capacitive applications, while the range for battery applications is 1.0–1.4 V.

The definition of capacitive behavior is a linear relation between the cell voltage and the accumulated charge (quantifiable by the unit of Farad = Coulomb/Volt). Often, the potential plateau from the battery material is interpreted as pseudocapacitive behavior because a linear-like behavior can be observed within the potential plateau over a narrow window. For instance, when the ZnI_2 system with a Zn negative electrode and AC positive electrode, or Zn|ZnI_2|AC (Fig. 4B), is operated over a narrow cell voltage window of 1.1–1.4 V, the potential plateau appears to be capacitor-like. The potential plateau is governed by the Nernst equation which is a non-linear function of $\log[(1-x)/x]$, where x is the state-of-charge of the redox species at the electrode/electrolyte interface. In general, the potential variation in the plateau regime is around 100–200 mV for one battery electrode and 200–400 mV for the cell with two battery electrodes. Hence, for the precise characterization of the potential plateau regime, the cell voltage range for the test should be larger than 500 mV.

In several recent works, the differentiation between capacitor-like and battery-like behavior has been discussed [25,37,38]. However, no clear quantitative criteria have been established on how to distinguish capacitor-like from battery-like behavior. For the identification of battery-like or capacitor-like behavior, an analysis can be carried out based on the derivative of the cell voltage with respect to the state-of-charge. In general, the slope of a capacitor with a maximum cell voltage of a V will be a. For the capacitive feature in the cell voltage window of 1.4 V, for instance, the derivative, or the slope of the potential and the state-of-charge, is 1.4 (Fig. 4C, *black dotted line labeled 'Capacitive slope'*). When a Faradaic reaction occurs, the derivative (Fig. 4C, red dotted line) will be below 1.4 due to the enhanced charge capacity in the system, while a slope higher than 1.4 indicates a capacitive contribution. When the derivative (dV/dx) is plotted versus the state-of-charge in a hybrid device, for instance, the Zn|ZnI_2|AC system [43], two regimes can be distinguished from the intersection between the derivative curve and the line with a constant value of 1.4 (Fig. 4C). The regime with the derivative lower than 1.4 matches with the potential plateau range in the cell voltage versus the state-of-charge plot; therefore, this regime represents the range that is dominated by the battery-like Faradaic reaction. Applying this way of differentiation, we can quantify that the system behaves over 97% battery-like in the tested cell voltage window. Therefore, the Zn|ZnI_2|AC REHES system can be classified as a battery with a nominal cell voltage of ca. 1.2 V.

When a hybrid device contains more than two potential plateaus, the dV/dx analyses can be applied effectively. For the AC|AC in $VOSO_4$ + $SnSO_4$ REHES system (Fig. 4D) [13], the device can be classified as battery-like because it shows over 50% contribution of battery-like Faradaic reactions in the tested cell voltage window. In the case of the AC|KI|AC REHES system (Fig. 4E) [44], higher linearity can be observed during discharge. Despite the Faradaic contribution over the potential range from 0.6 V to 1.0 V, the discharge profile appears linear with a slope close to 1.4. It is reasonable to assume a ± 10% error range for the determination of linear-like behavior; thereby, the AC|KI|AC REHES system (Fig. 4E) can be labeled capacitor-like based on its discharge profile. With these criteria, many of the hybrid devices can be classified quantitatively as capacitor-like devices despite their battery-like Faradaic origin. In short, the criteria for the capacitor-like and battery-like behavior are suggested in this review to be:

(i) For the capacitor-like system, the linear regime in the cell voltage window should be larger than 0.5 V.
(ii) Even if the slope is lower than the ideal capacitive slope, the regime can still be considered as linear when the value is within ± 10% error range of the capacitive slope.
(iii) Battery-like Faradaic behavior occurs when the slope is lower than the capacitive slope (including a ± 10% error range).

From these suggested criteria, an explicit assignment to capacitor or battery devices can be made. When a device has a 90% capacitor-like contribution with a continuous linear-like slope and 10% battery-like contribution, for instance, the device can be considered to be a capacitor. In that case, the operating potential should not cross the battery-like regime. Otherwise, the device should be labeled as a hybrid energy storage unit for the entire cell voltage window, including the capacitor-like and battery-like regimes. Similarly, when a device contains 90% battery-like and 10% capacitor-like regimes, the device can be considered as a battery, and the nominal cell voltage should be given. This approach follows commercial batteries where, for example, the cell voltage of a phone close to the capacitive regime will signal the device to be "empty". The rapid potential change below or above the operating potential is not appropriate for battery applications.

3. Design considerations for REHES systems

3.1. Selection of redox couples

The first step for REHES system design is to select the redox electrolyte. The standard redox potentials of the known redox couples (Fig. 5A) determine which redox couples can be used [71]. The actual redox potentials of the redox couples, however, can deviate from those determined under standard conditions. The key factors for this deviation in aqueous media are the pH value and the concentration of the electrolyte. For instance, the VO^{2+}/VO_2^{+} reaction can occur over a stable potential window at low pH values even though the standard redox potential of the VO^{2+}/VO_2^{+} couple is above the water stability window (Fig. 5B). The reason for this phenomenon is the potential up-shift of the oxygen evolution potential at low pH value (OER, Fig. 5C) [72]. Accordingly, evaluation of the corresponding Pourbaix diagram, or E_h-pH diagram, which shows the dependency on pH value and concentrations, considerably helps for the selection of the redox couples. Depending on the pH value of the aqueous electrolyte, the redox species can have different phases even when in the same oxidation state. For instance, Fe^{3+} may be present as a soluble ionic species in the electrolyte at low pH value but also exists as the solid phase Fe_2O_3 (Fig. 5C). The influence of the concentration on the redox potential must also be considered and can be assessed by use of the Nernst equation (Eq. (4)):

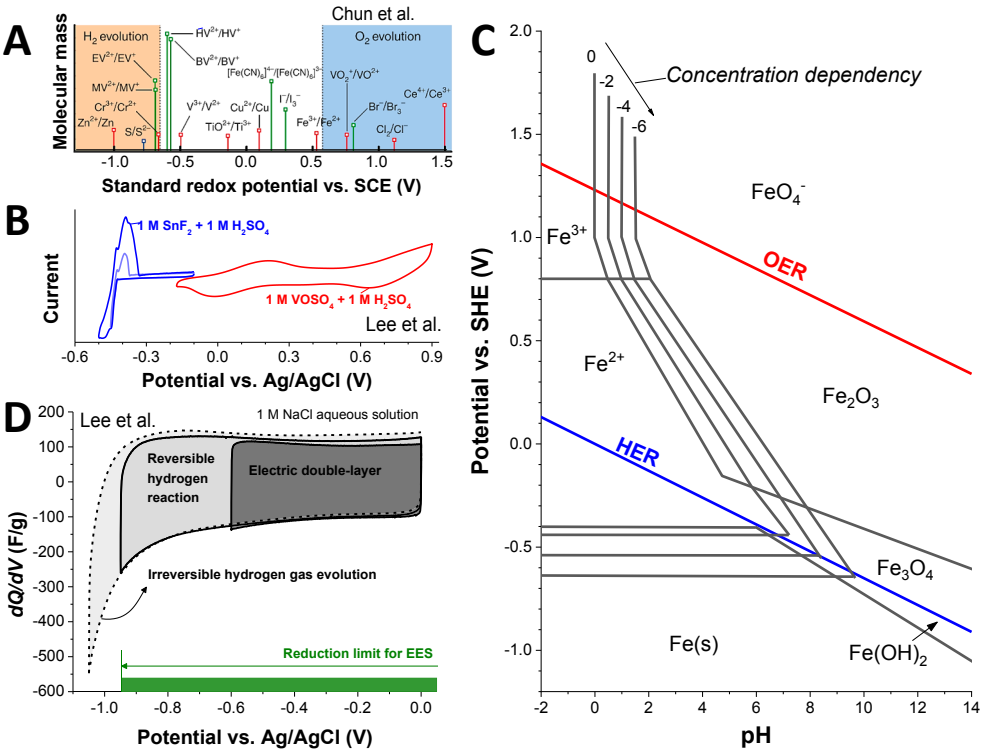

Fig. 5. Selected aspects of the selection of redox couples for the REHES systems. (A) Standard redox potentials for various redox couples. Reproduced with permission from Ref. [71] (B) Cyclic voltammograms of SnF_2 and $VOSO_4$ systems at low pH value. Adapted from Ref. [45] with permission from the Royal Society of Chemistry. (C) Pourbaix diagram for the aqueous iron system. (D) Cyclic voltammograms for microporous carbon electrodes in NaCl aqueous solution. Adapted from Ref. [107] with permission from John Wiley and Sons.

$$\varphi_e = \varphi_f(Ox/Re) + \frac{RT}{nF} ln\left(\frac{[Ox]}{[Re]}\right) \tag{4}$$

In this equation, φ_e is the potential of the half-cell with a redox couple having the oxidized form *Ox* and the reduced form *Re*, *R* is the universal gas constant (8.31 J/K·mol), *T* is the temperature in Kelvin, *n* is the electron transfer number, *F* is the Faraday constant (96,485.33 C/mol), and [*Ox*] and [*Re*] are the respective concentrations of the oxidized and reduced species at the electrode surface. The formal potential (φ_f) is defined via Eq. (5):

$$\varphi_f = \varphi_0(Ox/Re) + \frac{RT}{nF} ln\left(\frac{a_{Ox}}{a_{Re}}\right) \tag{5}$$

where a_{Ox} and a_{Re} are the activities of oxidized and reduced species, respectively. Depending on the activities of the oxidized and reduced species in the electrolyte, the formal potential shifts when the ionic strength of the electrolyte changes. For instance, the formal potential for Fe^{2+}/Fe_2O_3 (Fig. 5C) up-shifts at a fixed pH value when the concentration decreases according to Eq. (5).

The standard redox potentials for oxygen and hydrogen evolution also depend on the pH value. As the pH value increases, the OER and the hydrogen evolution reaction (HER) potentials shift towards more negative potentials (Fig. 5C). To understand the redox potential of hydrogen and oxygen reactions, one must consider catalytic effects as well. The following reported activity orders for HER and OER are useful to understand REHES systems:

(i) HER: Pb > Sn > Zn > Cd > Cu > Ti > Fe > Ag > Ni > Al > Co > Pd > Pt in alkaline media [73].
(ii) OER: Ru > Pd > Rh > Pt > Au > Nb > Zr ~ Ti ~ Ta in acidic media [74,75].

Higher catalytic activities of the electrodes lead to a lower stable operating potential for the actual EES device. Therefore, not only should the catalytic effects of pure metals be considered for the design of REHES systems, but also those of other materials such as metal oxides, metal sulfides, or heteroatom-doped carbons. For instance, heteroatom-doped carbons (e.g., doped with S, P, B, or N) [76] and MoS_2 [77] have recently been reported as promising catalysts to modify the HER and OER activities. The OER catalytic activity is also changed by FeO_x, CoO_x, MnO_x, or Fe-Ni alloys [74]. Hence, when electrode materials known for catalytic activities for the HER or OER are applied for REHES systems, the electrochemical stability window of the redox electrolyte must be carefully investigated. Under many circumstances, the desired redox reaction would ideally occur without crossing the actual OER and HER potentials in the system,

especially in the context of ion adsorption [78]. For instance, the HER was suppressed by modifying the interface of the cathode through functionalization with a cobalt-containing metallopolymer, which had a redox couple at a potential more favorable than that of HER. At the same time, reactions at the anode were controlled by the presence of an oxidation favorable redox metallopolymer to enhance ion capacity and selectivity. The final asymmetric redox system (poly(vinyl)ferrocene at the anode, (poly(2-(methacryloyloxy)ethyl cobaltocenium at the cathode) enhanced the electrochemical performance by limiting the voltage window within HER and OER [78]. For a variety of applications in both ion-adsorption and energy storage, it has been shown that the selection of redox configurations of the electrochemical cell can have beneficial outcomes for electrochemical current efficiencies, charge storage and electrochemical stability – mainly due to restriction of undesired electrocatalytic reactions and enhancement of desired Faradaic processes [79].

Another important aspect in REHES design is adjustments of the charge balance between the positive and negative electrode to enable the highest overall charge storage capacity in the cell to be attained. In the case of a device with one redox species, the potential development of the individual electrodes can be significantly different since the charge storage capacity of one electrode may be much larger than that of the other electrode when most of the redox reaction occurs at that electrode. When limited to the potential range of the positive electrode, systems such as Cu/Cu^{2+} [80], ferricyanide/ferrocyanide [65], and multiple redox reactions with iodide [61], capitalize on the reversible hydrogen reaction at the negative microporous carbon electrode [81–87]. Due to their redox activities at the positive electrode, the potential at the negative electrode rapidly increases until it reaches the potential for the $H_2(g)/2H^+$ reaction. Within carbon nanopores, the carbon surface can efficiently adsorb the dihydrogen intermediate through $C\text{-}H_{ad}/H^+$ reaction which can be back-oxidized reversibly to protons [83,85,88]. As thoroughly investigated by electrochemical and in-situ gas analyses [13,35,82,85,89], hydrogens can be stored reversibly in carbon micropores until actual gas evolution occurs at higher voltages (Fig. 5D, AC in 1 M NaCl aqueous solution). This reversible hydrogen reaction is the fundamental origin for high potential aqueous supercapacitors which operate over the cell voltage range of 1.2–1.8 V [90–94]. While it does contribute to the charge storage capacity, the central concern of reversible electrochemical hydrogen storage is that the energy efficiency of the overall process is reduced [95].

Another target in the selection of redox couples is maximization of the specific *energy*, which should be distinguished from the specific *capacity*. As initially demonstrated by Roldan et al., [64] the HQ/H system has a high specific capacity of around 63 mAh/g (converted from 901 F/g, since Farad is an incorrect unit to quantify a battery-like system). However, due to the redox reaction occurring at the cell voltage around 0 V, the energy enhancement of this system is ineffective since the specific energy measured during discharge is the area underneath the galvanostatic discharge curve (Fig. 6). Despite the three-fold enhancement of the specific capacity, the specific energy is barely doubled after introducing HQ/H redox couple into the system (note: the values in Fig. 6 are recalculated based on the discharge profiles from Ref. [64]). For an effective enhancement of specific energy, the redox couples should be selected to provide a maximum potential difference between the redox potentials of the electrolytes at the negative and positive electrodes. For example, Chun et al. and Evanko et al. carefully chose bromide and pentyl viologen which could give a redox potential difference of over 1 V with a cell voltage plateau region of 0.9–1.1 V (Fig. 6) [70,71]. One can clearly see the difference in specific energy by comparing the area underneath the cell voltage profile in Fig. 6.

In short, for the selection of redox couples, the standard redox potential (Fig. 5A) can guide to the balancing of redox activities of the electrolytes of the positive and negative electrodes. For a comprehensive selection of redox couples, the concentration and pH influence should be considered with the help of Pourbaix diagrams (Fig. 5C). After the selection of redox couples, the redox potential and the thermodynamic limits (such as precipitation and corrosion) should be determined experimentally. Particularly, the unique conditions of nanoconfinement in micropores may lead to variations in the redox reactions compared to theoretical expectations. Additionally, issues relating to toxicity, safety, material costs, and environmental influences should also be considered, as well as the intended temperature range for device operation.

3.2. Prevention of redox shuttling

The high mobility of soluble redox species may cause severe self-discharge of a REHES device. As demonstrated by Tachibana et al., the cell voltage of the REHES system with acetylferrocene rapidly approaches 0 V within just a few hours after having been charged

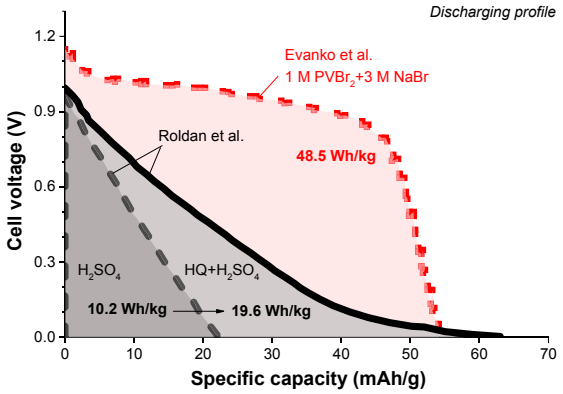

Fig. 6. Discharge galvanostatic profiles of the HQ/H REHES system from Ref. [64] and of the REHES system containing pentyl viologen ($PVBr_2$) and sodium bromide from Ref. [70] in AC|AC configuration.

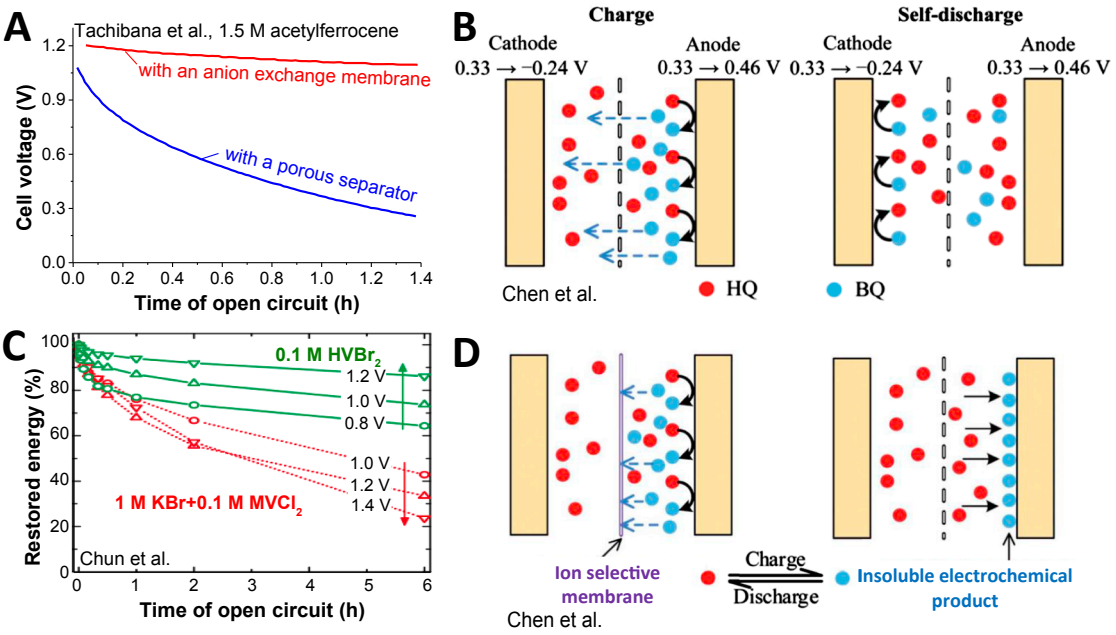

Fig. 7. Redox shuttling in the REHES systems and the known methods for the prevention. (A) High rate of self-discharge by the redox shuttling of ferrocenium cations through a porous separator and its prevention by an anion exchange membrane from Ref. [96]. Redox shuttling phenomenon by the hydroquinone/p-benzoquinone (BQ) redox couple for a porous separator (B) and the prevention of redox shuttling by introducing an ion selective membrane or an insoluble redox couple (D). Adapted from Ref. [103]. Published by The Royal Society of Chemistry. (C) Prevention of redox shuttling by the adsorption of bromide and viologen ions at the porous carbon material. The restored energy values are obtained from the AC|AC cells in 0.1 M 1,1′-diheptyl-4,4′-bipyridinium dibromide ($HVBr_2$) and 1 M KBr + 0.1 M $MVCl_2$. Adapted from Ref. [71].

(Fig. 7A) [96]. To suppress the self-discharge process, Tachibana et al. used an anion exchange membrane as it effectively hindered the mobility of ferrocenium cations from the positive electrode to the negative electrode. The latter case is known as redox shuttling, and it causes the reduction of ferrocenium cations which are oxidized initially during charging. In Fig. 7B, the self-discharge process by redox shuttling is described schematically for the HQ/*p*-benzoquinone (BQ) redox couple. After being oxidized from HQ during charging, BQ diffuses through the porous separator to the other compartment, and the cell is self-discharged as BQ reduces back to HQ.

Since self-discharge is closely related to the energy efficiency of the system, prevention or suppression of redox shuttling is of vital importance to any EES system. If the origin of the self-discharge is the diffusion of the redox species from one compartment to the other, redox shuttling must be reduced by inhibition of the diffusion of the soluble species. One approach is to apply ion selective membranes to suppress the diffusion of the reduced/oxidized ions or molecules after charging the cell (Fig. 7D, *left*).

To prevent cation diffusion, for example, of VO_2^+ and VO^{2+} [13,45], anion exchange membranes can be applied; vice versa, cation exchange membranes effectively stop the ion shuttling of anions, such as iodide and bromide [44]. When both cation and anion species occur, or neutrally charged molecules such as HQ, proton exchange membranes can be used [46]. Another approach is to apply soluble redox species that undergo solid phase conversion during charging, as demonstrated by Chen et al. (Fig. 7D, *right*) with Cu(s)/Cu^{2+} redox couple. As the conversion into a solid phase prevents diffusion, the self-discharge rate can be reduced effectively. Nevertheless, such redox electrolytes with solid phase conversion do not fit the strict definition of REHES given in Section 1.

Alternatively, the diffusion of soluble redox species can also be reduced when they are adsorbed on the electrode surface. As reported by Chun et al., [71] the strong adsorption of bromide in carbon micropores significantly suppresses the diffusion rate of oxidized bromide ions from the positive electrode to the negative electrode (Fig. 7C). However, the reported bromide system still shows an energy loss of 10–20% 6 h after charging. Although this is a higher loss rate than observed with conventional batteries, the bromide REHES system is still promising for applications where fast charge/discharge is required (5–10 h intervals). Albeit very important from an application point of view, self-discharge rates of REHES systems have been investigated only by a few researchers.

4. Critical characterization of redox electrolyte systems

4.1. Energy and power performance

The specific energy (E_s in Wh/kg) is one of the most critical performance metrics of EES devices. The specific energy can be calculated by Eq. (6):

$$E_s = \frac{1}{3600 \cdot m_a} \int V_c I dt \tag{6}$$

where m_a is the mass of the active electrodes in the device in kg, which actively contributes to the charge storage capacity, I is the discharging current in A, and t in seconds. Typically, the specific energy is derived from data during the discharge of the device. The energy efficiency (ε_E) can be calculated according to Eq. (7):

$$\varepsilon_E = \frac{E_{dis}}{E_{char}} \tag{7}$$

where E_{char} is the energy invested during cell charge and E_{dis} is the energy recovered during cell discharge.

According to Eq. (6), the specific energy is the area beneath the cell voltage profile determined by galvanostatic measurement (Fig. 6). Since the shape of the voltage profile is triangular for supercapacitors, Eq. (6) can be simplified to yield Eq. (8):

$$E_{s,cap} = \frac{C_d V_c^2}{2 \bullet 3600} \tag{8}$$

The device specific capacitance C_d is defined via Eq. (9):

$$C_d = \frac{Q}{m_a \Delta V} \tag{9}$$

where Q is the accumulated electric charge during the cell operation in the cell voltage window (ΔV). For batteries, the specific energy is roughly the multiple of operating potential, specific current, and discharge time by galvanostatic measurement.

For REHES and many hybrid EES systems, the performance values are often incorrectly calculated by use of Eq. (8) despite the non-capacitive behavior of the device [25,39,95]. When a Faradaic activity of the redox electrolyte enhances the specific capacity of the REHES system, an apparent potential plateau can appear in the voltage profile [25]. If the potential plateau is in a low cell voltage range, the use of Eq. (8) may result in a severe overestimation of the actual performance. For instance, the area underneath the cell voltage profile of the REHES system with 1.2 M PFC (Fig. 8A) is apparently smaller than the area depicted by Eq. (8). Even more critical, in some cases, the specific energy has been calculated from the slope over a certain cell voltage range, and the estimated capacitance value has been used in Eq. (8). For example, when calculated at the potential plateau in Fig. 8A, a large virtual capacitance of 2389 F/g (normalized by m_a) is obtained. Furthermore, by assuming the 1.23 V width of the theoretical potential window and applying Eq. (8), the specific energy would appear to be 120 Wh/kg (normalized by m_a), which is far beyond the actual value of 5.6 Wh/kg that the system can deliver [39].

Often, the specific energy of the REHES devices is determined by a sweep of the cell voltage from positive to negative values (Fig. 8B) [97–99]. This approach does not, however, directly represent the actual performance since the negative polarization below

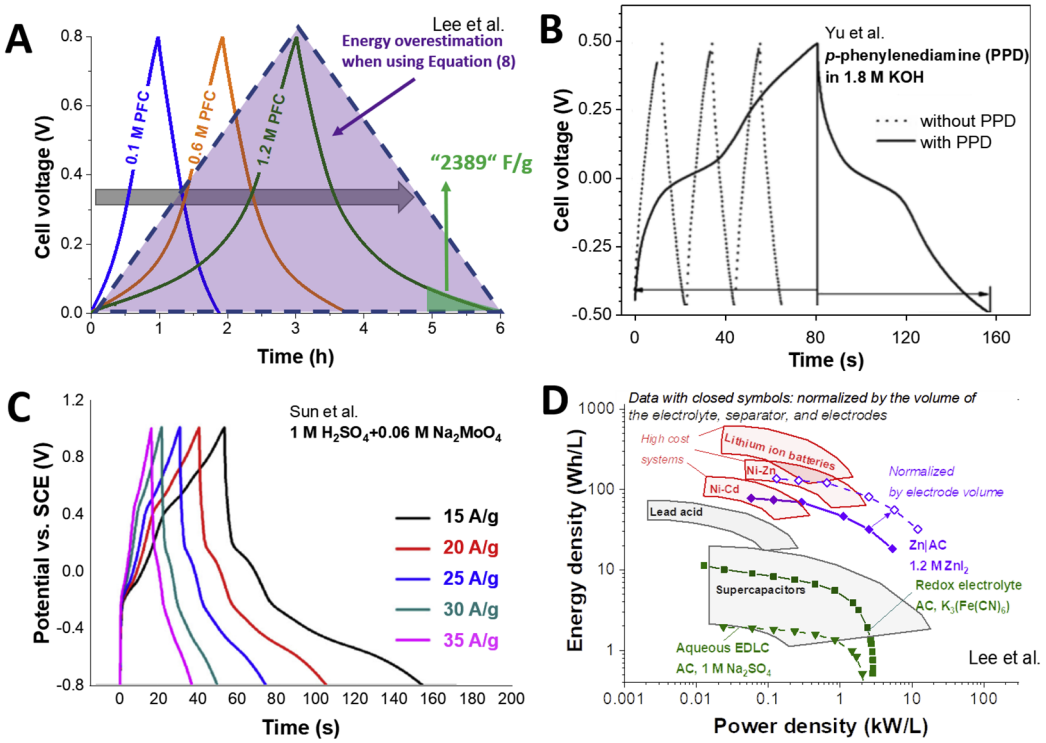

Fig. 8. Performance data for selected REHES systems. (A) An example of the performance overestimation by applying inappropriate equations. Adapted with permission from Ref. [38] Copyright (2017) American Chemical Society. (B) Characterization of the system by polarizing the cell potential from positive to negative values from Ref. [98]. (C) Characterization of the system in half-cell configuration from Ref. [101]. (D) Energy and power density values are normalized by the volume. Adapted from Ref. [43] with permission from The Royal Society of Chemistry.

0 V does not survey energy recovery, but constitutes energy consumption. To understand REHES systems, the potential of the cell can be swept from negative to positive values; however, the data thereof should not be used for the calculation of the specific energy [97–99]. The possible exception is for the symmetric capacitor systems where the slope in the galvanostatic plot does not change. Likewise, reporting of the specific energy based on the half-cell data of the hybrid EES systems should be avoided (Fig. 8C) [100,101]. The specific energy of a hybrid electrode should be calculated based on the assumption of an ideal opposite electrode with a known electrochemical behavior. For instance, the specific energy of a lithium-ion battery can be estimated from the half-cell data for the positive electrode if the redox potential assumed is for the graphite negative electrode with infinite capacity.

Another important performance parameter reflects the charge/discharge rate capability. The specific power (P_s in kW/kg) is often reported based on Eq. (10):

$$P_s = \frac{3600 \bullet E_s}{\Delta t_{dis}} \tag{10}$$

where Δt_{dis} is the discharge duration. In the case of batteries, the multiplication of the operating cell voltage and the discharge current often approximates the electric power of the device. Hence, batteries supply roughly a stable power since their operating potential window is typically very narrow. By comparison, the electric power of supercapacitors significantly drops as the cell voltage decreases during discharge.

Most adequately, the specific power (kW/kg) is calculated from the data obtained during discharge. Often, the specific power is derived from the charging process, which may result in misleading and incorrect data. For higher resistance values, a lower specific power is expected; however, we see an artificial enhancement of the specific power when it is calculated from the charging energy by Eq. (10). For instance, when two devices provide the same specific power during discharge, the one with higher resistance will consume more energy during charging, leading to a higher specific power value calculated from Eq. (10). Thus, the high specific power during charging does not necessarily indicate a rapid charging process. To claim fast charging capability, either high specific current or high upper limit potential can be reported; the latter enables higher charging voltage than the nominal voltage in the case of batteries.

For a comparison of different EES devices, it is convenient to present the performance in a Ragone (pronounced “ru-GO-nee”) diagram, where energy storage capacity and electric power values are plotted. In such diagrams, the performance values are conveniently normalized by the mass or the volume of the device (Fig. 8D) [43]. Normalization by the volume is of particular importance to space-sensitive applications, as in the case of electric vehicles or mobile computing. Porous carbon materials are much lighter than metals and metal oxides; however, their low density is a drawback for volumetric performance. When comparing data in Ragone diagrams, a key issue is the distinction between normalization on a device level and data normalized just by the active material [102]. Ragone himself normalized by device mass because the purpose was the facile comparison of technologies (in contrast to comparing materials). The mass (or volume) of just the electrodes is much smaller than that of assembled cells, and thus a comparison between different technologies (and different devices) becomes complex. For instance, the data for commercial (well-engineered) devices are often compared with electrodes assembled in a laboratory, where only the electrodes (not the optimized cell) are measured. To ensure comparability, at least one should only compare data that were normalized in the same way (e.g., just electrode data or just device data).

As shown in Fig. 8D for the Zn|ZnI_2|AC REHES system, normalization only by the electrode volume can be misleading when the results are compared to commercial devices. Hence, a fair comparison with reported systems requires a clear outline of the way in which the results have been normalized. In the case of REHES systems, not only does the electrode material contribute to the charge storage capacity, but also the electrolyte. The contribution of the latter can lead to performance overestimation, particularly for devices containing a large volume of the redox electrolyte as compared to those with small electrodes. For this reason, normalization of the performance by the volume or mass of the electrolyte, separator, and electrode (Fig. 8D) can provide a more realistic comparison with commercial products with device normalization. Thus, a volume limited cell is recommended to confine the electrolyte to space of the electrode and separator [39,71,103]. When laboratory scale systems are reported, the outer housing and current collectors are often significantly larger than the electrode, electrolyte, and separators.

4.2. Determination of electrochemical stability

Electrochemical stability is a crucial requirement for the robust cycle life of EES systems. In most cases, the electrochemical stability is limited by irreversible decomposition of the electrodes or electrolytes. For REHES systems, the electrochemical stability of the electrolyte is particularly important due to the additional redox activities of the dissolved redox ions. At a certain pH value, the electrochemical stability window is not only limited by irreversible oxygen or hydrogen evolution, but also by the irreversible phase transition of the dissolved ions into solid or gas phases. For instance, in the case of the REHES systems with bromide and ferrocyanide/ferricyanide, the corrosive and volatile nature of bromide or the high toxicity of hydrogen cyanide can lead to severe health and safety issues. Therefore, the electrochemical stability window must be determined carefully.

For the investigation of undesired phase transition of the redox ions, in-situ techniques such as Raman spectroscopy or electrochemical mass spectroscopy can be applied effectively. For example, as demonstrated by Fic et al., [89] electrochemical sorption of hydrogen on microporous carbon can be studied by in-situ Raman for the C-H bond. He et al. used in-situ gas analyses by online electrochemical mass spectrometry and cell pressure measurements (Fig. 9A) to determine ion-current profiles for O_2, H_2, CO, and CO_2 during the electrochemical operation of the cell [82,85]. Their approach provided a unique interpretation of the mechanisms of electrolyte decomposition and side reactions at the carbon surface.

Advanced electrochemical analyses without in-situ or in-operando measurements can also enable detailed investigations of the undesired phase transitions in REHES systems. Conventionally, galvanostatic charge/discharge with potential limitation (GCPL) is applied to report the

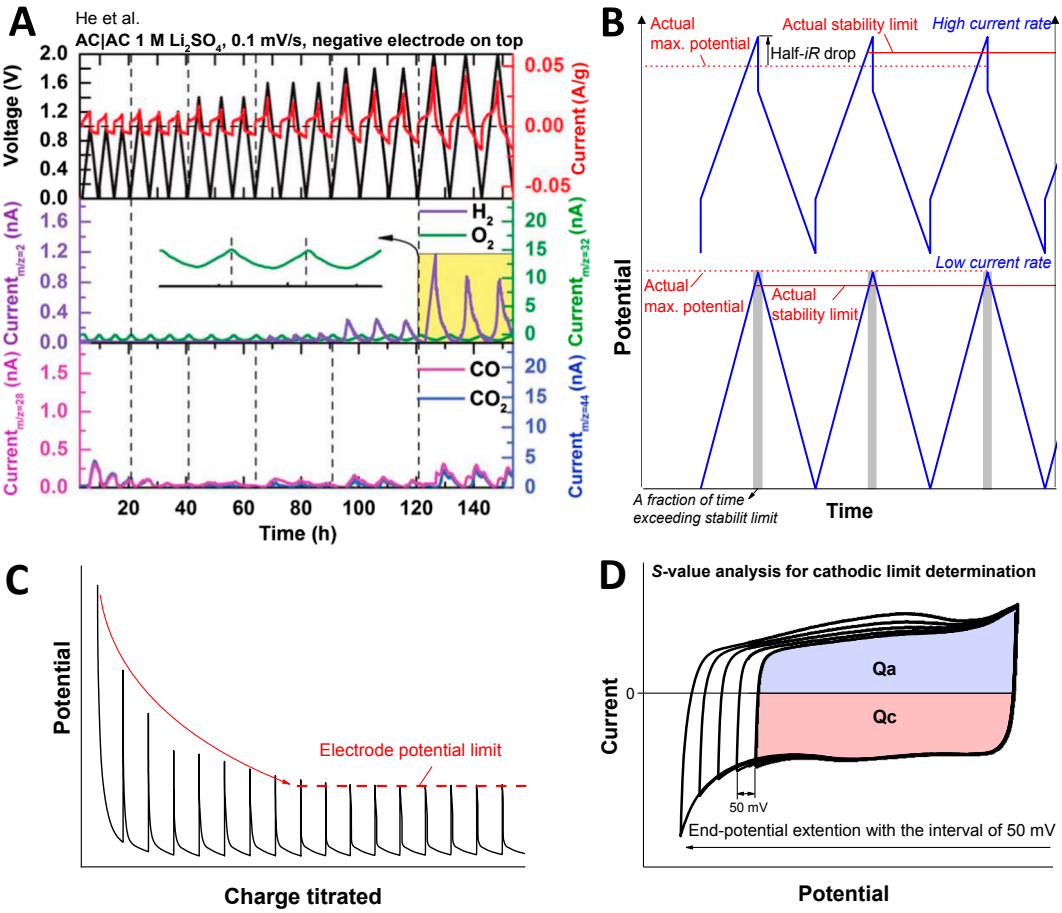

Fig. 9. Advanced characterization techniques for the determination and the investigation of the electrochemical stability of the EES systems. (A) In-situ gas and pressure analysis for the detailed degradation mechanisms of the porous carbon electrodes and aqueous electrolytes. Adapted from Ref. [85]. Published by The Royal Society of Chemistry. (B) Limitations of galvanostatic cycle test (C) Galvanostatic intermittent titration technique for the determination of electrolyte decomposition potential. (D) *R*-value (also known as *S*-value) analysis with cyclic voltammetry.

cyclic stability and the reversibility of the device or individual electrode. The capacity, Coulombic efficiency, equivalent series resistance, and the potential profile at each cycle provide information to identify undesired phase transitions. However, the data from GCPL measurements are often not sufficient to identify the precise origin of the stability degradation. For additional information, other electrochemical analyses such as electrochemical impedance spectroscopy (EIS) can be carried out at specified cycle intervals [81].

During GCPL cycling, the potential of the system exceeds the stability limit in a fraction of time compared to the entire charging/discharging period (Fig. 9B); therefore, the stability limit can be overestimated [104]. Furthermore, GCPL often employs large currents to shorten the measurement time, but this may lead to an overestimation of the apparent cyclic stability. High currents can cause a rather large *iR* drop which prevents the system from reaching the targeted maximum potential for the test. For these reasons, voltage floating can be applied to determine the electrochemical device stability more realistically [104]. During voltage floating, a constant potential, also referred to as floating potential, is applied, and the system is supplied with sufficient current (floating current) to maintain the potential. A detailed analysis of floating currents will be given in Section 4.3. Conveniently, voltage floating is interrupted at pre-set intervals to carry out complementary electrochemical measurements, such as EIS, CV, and GCPL; after these tests, the floating potential is re-established and maintained for a pre-defined duration until the next set of complementary measurements are carried out (e.g., every 10 h over a total duration exceeding 100 h). This approach allows the tracking of changes in electrochemical properties, for example, electrolyte decomposition or other degradation processes. If there is an irreversible phase transition, the capacity will fade rapidly under the harsh floating conditions.

While important for the benchmarking of practical voltage limits, a floating experiment only yields data for one pre-set potential value. For the survey of the potential dependency of the on-set of electrochemical instability, multiple sets of data at different potential limits are required, or other methods can be applied. For instance, galvanostatic intermittent titration (GITT) analysis requires only one set of data in a relatively short time frame (10–40 h) for identifying the potential limits for individual electrodes [89]. For this method, a given amount of charge is titrated to the electrode over a certain time interval during which the potential of the electrode is measured (Fig. 9C). When the potential of the irreversible reaction is exceeded, the electrode potential stagnates despite the continuous titration process due to the charge consumption by the irreversible reaction. Yet, GITT does not provide detailed information about the origin of the potential limit; hence, other complementary electrochemical analyses are still required, such as CVs.

Another helpful electrochemical analytical tool to quantify stability limits is a determination of the *R*-value, or also known as *S*-value analysis. The *R*-value analysis was initially suggested by Xu et al. based on the Butler-Volmer equation that shows that the kinetic current for Faradaic reaction increases exponentially with the potential increase [105]. The criteria for Faradaic decomposition were further refined by the Kötz Group [106] under the name *S*-value analysis (*S* for stability). Instead of the initial criterion that the *R*-value exceeds 0.1 for the onset of decomposition, a new criterion was suggested that a second derivative of the *S*-value ($d^2S/d\varphi^2$) exceeding 0.05 indicates the onset of Faradaic decomposition. *S*-value and *R*-value analyses can be carried out simply by cyclic voltammetry; the maximum potential is extended from a fixed starting potential over a certain potential interval (Fig. 9D). The *S*-values (equal to *R*-values) can be obtained as:

$$S_a = \frac{Q_a}{Q_c} - 1 \tag{11}$$

$$S_c = \frac{Q_c}{Q_a} - 1 \tag{12}$$

where S_a is the *S*-value for the anodic limit, S_c is the *S*-value for the cathodic limit, Q_a is the charge accumulated due to the anodic current, and Q_c due to the cathodic current. The main advantages of the *S*-value analysis are: (i) only one set of data is required over a relatively short time frame (1–3 d), (ii) complementary analyses are available by CVs, and (iii) reversibility of the reaction can be evaluated quantitatively.

The establishment of a universal *S*-value criterion is a challenging task since electrochemical behavior differs from system to system and may also depend on the applied scan rate. For instance, application of the *R*-value criterion ($R > 0.1$) or *S*-value criterion ($d^2S/d\varphi^2 > 0.05$) can lead to misinterpretation of the cathodic limit of porous carbon in aqueous solution (Fig. 10A) [107]. In general, the onset of a substantial cathodic current increase in the cyclic voltammogram is interpreted as the cathodic limit by hydrogen gas evolution. This approach cannot be applied to porous carbon electrodes because of the reversible C-H_{ad}/H^+ redox reaction (Fig. 5D). The latter also contributes to the cathodic current increase which does not necessarily mean an irreversible reaction. Hence, the *S*-value analysis is particularly useful for the quantitative evaluation of the reversibility regarding the hydrogen reaction at the porous carbon electrode (Fig. 10A, AC in 1 M NaCl aqueous solution). A linear slope in an *S*-value plot from 0.60 V to −0.95 V vs. Ag/AgCl implies operation in a regime where hydrogen can be reversibly stored while the exponent increase below −0.95 V vs. Ag/AgCl indicates irreversible hydrogen gas evolution. These results correspond to the studies with high voltage aqueous

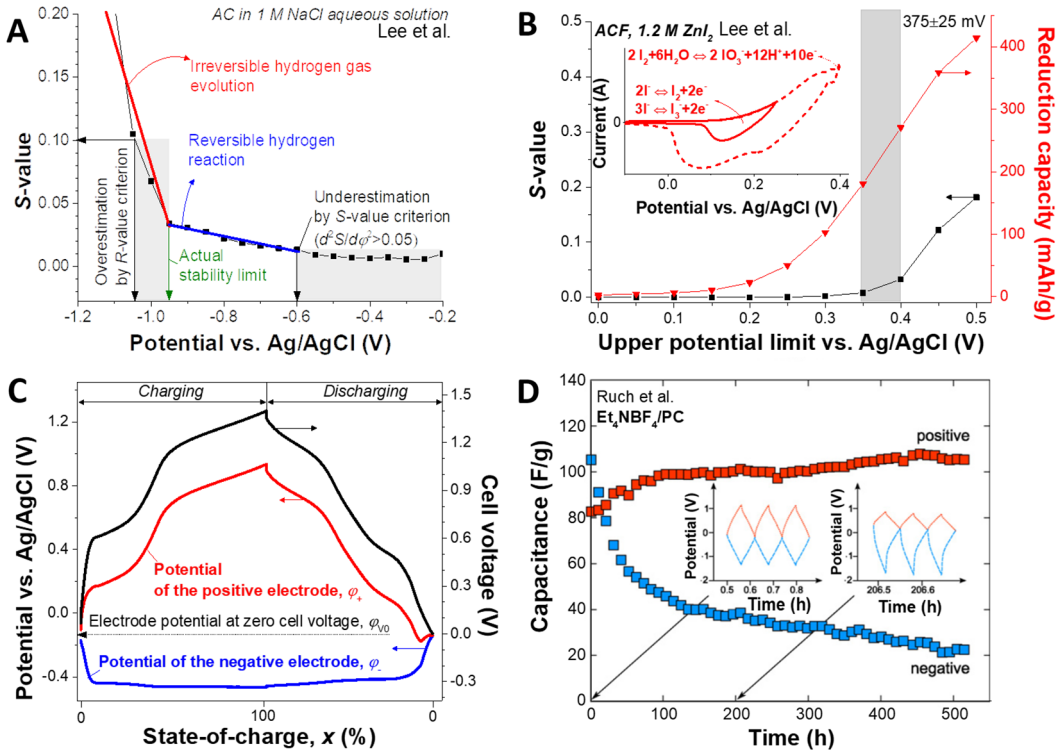

Fig. 10. Electrochemical analyses to characterize the system stability. (A) The evaluation of S-value for the reduction limit in aqueous solution. Reproduced from Ref. [107] with permission from John Wiley and Sons. (B) The *S*-value analysis of the activated carbon fiber electrode (ACF) in 1.2 M ZnI_2 aqueous solution. The inset shows redox activities of the ZnI_2 solution in cyclic voltammogram. Adapted from Ref. [43] with permission from The Royal Society of Chemistry. (C) The cell and cable configuration with a spectator reference electrode allow tracing the individual potentials for the positive and negative electrodes while operating the device voltage. Adapted from Ref. [70]. Published by The Royal Society of Chemistry. (D) Long-term stability test for a double-layer capacitor (AC|AC) with 1 M tetraethylammonium tetrafluoroborate (Et_4NBF_4) in propylene carbonate (PC). The inset shows the potential profiles of the positive and negative electrodes in the device. Reprinted from Ref. [108], Copyright (2018), with permission from Elsevier.

EDLCs (1.6–1.8 V) and in-situ gas analyses [35,81,85,90,91,93,94]. For reversible electrochemical hydrogen storage, the cathodic limit can be overestimated from the *R*-value analysis and underestimated when using the *S*-value criterion (Fig. 10A).

The *S*-value analysis can be applied effectively even in the presence of multiple redox activities whose redox potentials are close to each other. In the case of AC electrodes with an iodide-containing electrolyte, the main limitation for the positive potential limit seems to be not by OER, but by the low Coulombic efficiency through the conversion to iodate [43]. Since the *S*-values are obtained from the cyclic voltammograms at each potential step, they provide complementary information such as specific capacity and the types of redox reactions. Thereby, the potential limit of the activated carbon fiber (ACF) electrode operated in aqueous 1.2 M ZnI_2 is determined to be 0.35–0.40 V vs. Ag/AgCl according to the exponential increase in the *S*-value (Fig. 10B). The origin of the latter can be identified as the iodine/iodate reaction based on the redox peak around 0.40 V vs. Ag/AgCl in the CV (Fig. 10B, *inset*). By comparison, the redox reactions with polyiodide in the range of 0.10–0.35 V vs. Ag/AgCl are reversible in terms of stable *S*-values. Up to the cathodic limit of 0.35 V vs. Ag/AgCl, the charge storage capacity significantly increases to 200 mAh/g (normalized by m_a).

In contrast to supercapacitors, the voltage limits of REHES devices cannot be estimated merely based on the cathodic and anodic limits determined from half-cell experiments. During charging/discharging of a REHES device, redox activities contribute to charge storage capacities differently at each electrode, which leads to difficulties in prediction of the potential development of an individual electrode. Therefore, the device stability still must be evaluated in a full-cell configuration even when the potential limits are carefully determined for the individual electrodes in half-cell configurations. Only in this way it is possible to obtain data based on the actual device performance for practical EES applications. For the investigation on how the individual electrode potential develops in a device, it is convenient to add a spectator reference electrode to a full-cell setup to observe the potential of the counter electrode while operating at the cell voltage (Fig. 10C) [13,70]. By this way, the cell works like the actual device for energy storage while basic electrochemical benchmarking is still enabled. The working electrode potential is obtained by subtracting the counter electrode potential from the cell voltage. For the analysis, the electrode potential at zero cell voltage, φ_{V0}, the potentials of the positive (φ_+) and the negative electrode (φ_-) at various states-of-charge are particularly important. First, the most critical point is that the φ_+ and φ_- do not cross the stability limits; the shift in φ_{V0} is also important since it could lead to the situation that either φ_+ or φ_- crosses the stability limit. Furthermore, if the capacity fades differently for each electrode (Fig. 10D), the device could exceed the stability limit because the potential at the electrode with more capacity fade will develop more rapidly than that of the other electrode (Fig. 10D, *inset*) [108]. Therefore, careful evaluation of each electrode is needed for full-cell devices.

4.3. Time-dependent potential decay (self-discharge)

Despite the importance of the self-discharge by redox shuttling for efficient energy storage of REHES systems, the self-discharge rate of the REHES systems remains ill-explored. Instead of investigating the energy efficiency, researchers mostly report high Coulombic efficiency values (> 90%) to validate efficient energy storage performance. However, the Coulombic efficiency values at high current rate do not adequately represent the self-discharge characteristics of the system. For instance, when a system has a high self-discharge rate caused by redox shuttling, the Coulombic efficiency values increase as a function of the specific current because the time frame for the charging/discharging process is shorter than the time for the self-discharge current at a higher current rate (Fig. 11A).

For the characterization and the analysis of self-discharge behavior, either a full-cell or a half-cell configuration can be applied. The full-cell configuration allows characterization of a more application-realistic performance of the entire system, while the detailed analyses of the individual influences of each electrode are challenging. Often, full-cells with a spectator reference electrode are applied. Such setups enable the operation with a full-cell configuration and still allow measurement of the individual potential of each electrode. For a detailed analysis of the self-discharge behavior of one electrode, the half-cell configuration is still necessary. The combined studies with the half-cell and the full-cell can provide a comprehensive understanding of the self-discharge behavior of redox electrolyte systems [109].

The two most common methods to quantify and investigate self-discharge are the open-circuit potential (OCP) measurement (Fig. 11B) and floating current analysis (Fig. 11C and D). The monitoring of the open-circuit potential may provide information closest to that needed for the actual application; furthermore, it conveniently allows analysis of the underpinning mechanisms when modeling is implemented. For the comparison and the interpretation of the OCP profile, the characteristic differences between batteries and capacitors must be considered correctly and reflected to describe the self-discharge process. In the case of capacitors and capacitor-like devices (Fig. 1C), the potential varies linearly with the total accumulated charge; hence, the OCP loss is due to self-discharge (loss in stored charge) in the absence of the charge redistribution (see more details in Section 5.3.1). For batteries (Fig. 1B), the loss in charge is not linearly correlated with the OCP loss. For that reason, restored electric charge as a function of resting time is much more representative for the self-discharge rate; the restored electric charge can be obtained by discharging the cell after the resting period.

Instead of plotting the OCP change over time, one can also calculate the restored energy to evaluate how much energy was lost due to cell self-discharge and voltage decay. Such values are only meaningful when benchmarking full-cell devices and not half-cells. The specific energy must be understood as the combined data for both positive and negative electrodes. For the interpretation, the decrease in specific energy should not be directly interpreted as the sole result of self-discharge, because the cell resistivity can also contribute to the energy loss. The measured restored energy without resting time can help to identify energy loss due to the cell resistance (Fig. 7C). For a comprehensive understanding of the self-discharge process, it is important to report the restored electric charge, the restored energy, and the actual OCP profile; conveniently, all three parameters can be obtained from one experimental setup.

The floating current analysis can be carried out by measuring the current response after the desired potential is reached and held

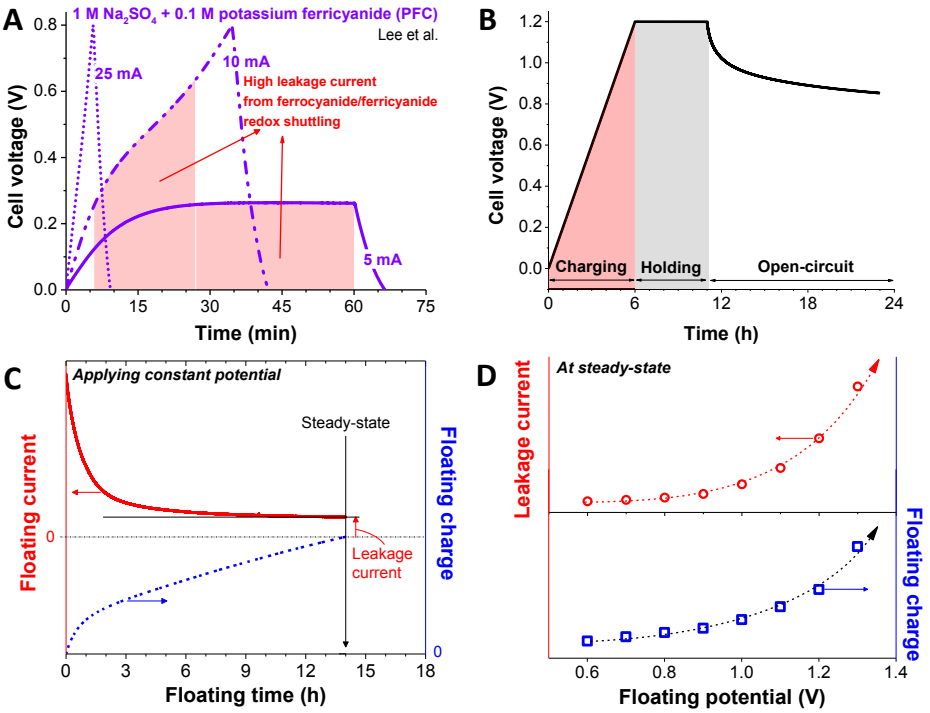

Fig. 11. Electrochemical analyses for self-discharge phenomena. (A) Galvanostatic charging/discharging profiles of the REHES system with AC electrodes in potassium ferricyanide at various applied currents. Adapted with permission from Ref. [39]. Copyright (2017) American Chemical Society. (B) Open-circuit potential measurement. (C-D) Analyses with the floating current and floating charge.

(Fig. 11C). This current response indicates that the system is still being charged because of the electrochemical kinetics and that the system consumes current by self-discharge. Therefore, a constant current response at steady-state (no reversible charging current is flowing) is interpreted as the leakage current of the system (Fig. 11D, *top*). Integration of the measured floating current over floating time until steady-state is reached yields the total accumulated charge, or floating charge (Fig. 11D, *bottom*) which is helpful to identify and characterize the discharge mechanisms [110].

Based on the considerations introduced in this section, we see that thorough characterization of self-discharge is necessary for REHES systems, particularly, in the case that redox shuttling is expected. For practical applications, it is crucial to quantify the self-discharge rate and to compare it with reference systems such as commercially available double-layer capacitors. Further improvements of REHES systems will then require a firm understanding of the self-discharge mechanism(s). More discussion on the state of the art of theoretical and modeling work regarding self-discharge is found in Section 5.3.1.

5. Recent progress on REHES systems

According to the solvent used for the REHES systems, three different types of redox electrolytes can be identified: (i) aqueous redox electrolytes, (ii) organic redox electrolytes, and (iii) IL redox electrolytes. In earlier works, Senthilkumar et al. categorized the redox electrolyte systems as (i) redox active liquid electrolytes, (ii) redox additive liquid electrolytes, or (iii) redox-polymer electrolytes [37]. Accordingly, the redox additive liquid electrolytes were defined as electrolytes in which redox additives or compounds are added. However, the definition of redox additive liquid electrolytes is rather ambiguous. For instance, potassium ferricyanide with KOH aqueous solution [111] would be a redox additive liquid electrolyte, whereas a potassium ferricyanide aqueous solution [39,66] would be a redox active liquid electrolyte. Potassium ferricyanide can be used without additives since its cations and anions enable sufficient ionic conductivity and EDL formation along with the redox reaction of ferrocyanide/ferricyanide [39]. The performance of REHES systems employing the ferrocyanide/ferricyanide redox couple can be further modified in basic media, with the latter acting as an additive [112]. Therefore, a more suitable classification would be based on the state-of-charge of redox ions [25]:

(i) Cationic redox electrolytes (e.g., Cu^{+}/Cu^{2+}).
(ii) Anionic redox electrolytes (e.g., ferrocyanide/ferricyanide).
(iii) Neutral redox electrolytes (e.g., quinone/hydroquinone).

Unlike the cationic and anionic redox electrolytes, redox species in neutral redox electrolytes, such as quinone/hydroquinone and *p*-phenylenediamine, do not contribute to the electrical double-layer formation. Furthermore, their charge neutrality is responsible

Table 1
Electric energy storage with cationic aqueous redox electrolytes. The values are taken from the full-cell configuration unless otherwise noted as half-cell. The specific single electrode capacitance values were taken to report the capacity unless otherwise noted as cell capacitance. Specific current is normalized to the projected area of the electrode unless otherwise noted.

Electrolyte[1)]	Electrode configuration[1)]	Separator	EES type	Capacity	Specific energy (Wh/kg)	Potential window (V)	Maximum rate[2)]	Specific power (kW/kg)	Normalization	Capacity stability (%)[3)]	Self-discharge[4)]	Coulombic efficiency	Ref.
Transition metals													
Fe^{2+}, Cu^{2+}, H_2SO_4	MC-GP|MC-GP	–	Battery-like	223 mAh/g	–	–	2 A/g	–	–	−26% (400 cycles, 0.5 A/g)	–	92% (0.5 A/g)[16)]	[60]
$VOSO^4$|KI	MC|MC	PEM	Capacitor-like	500 F/g[5)]	20	0/0.8		2	–	–	–	100% (0.5 A/g)	[46]
$VOSO_4$, H_2SO_4	MC, half-cell	–	Battery-like	2.1 F/cm^2		0.2/1.3 (Ag/AgCl)	0.1 A/cm^2		BET SSA	−8% (5000 cycles, 0.1 A/g)	–	22% (30 mA/g)[16)]	[174]
$VOSO_4$, $SnSO_4$, H_2SO_4	MC|MC	AEM	Battery-like	–	75	0/1.4	–	1.5	m_a	−15% (4500 cycles, 1 A/g)	17% (voltage, 10 h)	95% (0.1 A/g)	[13]
SnF_2, H_2SO_4|$VOSO_4$, H_2SO_4	MC|MC	AEM	Battery-like	–	58.4	0/1.4	–	3.8	m_a	−20% (6500 cycles, 1 A/g)	13% (voltage, 10 h)	96% (0.1 A/g)	[45]
$CuCl_2$, HNO_3	PCMS|PCMS	PS	Capacitor-like	294 F/g[5)]	73	0/1.35		7.5	m_a	−0.9% (1000 cycles)	–	100% (15 A/g)	[80]
$(NH_4)_2Fe(SO_4)_2$, H_2SO_4	MC-GP	–	Battery-like	1499 F/g	58.7	−0.5/0.5		100	m_a	−6.2% (10,000 cycles, 0.1 A/g)	–	100% (10 A/g)[16)]	[115]
Lanthanide													
$Ce_2(SO_4)_3$, H_2SO_4	MGP|MWCNT	–	Battery-like	64 F/g	13.84	0/1.5	88.4 mA/cm^2	–	m_a	−6% (3000 cycles, 44 mA/cm^2)	–	68% (17.7 mA/cm^2)[16)]	[114]
Organic cations													
Methylene blue[17)], H_2SO_4	MWCNT|MWCNT	PS	Battery-like	23 F/g[5)]	–	0/1	88.4 mA/cm^2	–	m_a	–	–	88% (0.88 mA/cm^2)[16)]	[116]
Methylene blue[17)], H_2SO_4	MWCNT|MWCNT	PEM	Capacitor-like	14 F/g[5)]	–	0/1	8.8 mA/cm^2	–	m_a	–	–	100% (8.8 mA/cm^2)[16)]	[116]
Methyl viologen dichloride[18)], KBr	MC|MC	PS	Battery-like	49.8, 13.3[10)]-	51, 13.9[10)]	0/1.4	–	0.52, 0.14[10)]	m_a, m_b[10)]	–	76% (energy, 6 h)	99% (0.5 A/g)	[71]
Heptyl viologen dichloride[19)], KBr	MC|MC	PS	Battery-like	44.0, 12.1[10)]	39.3, 10.8[10)]	0/1.4	–	0.45, 0.12[10)]	m_a, m_b[10)]	–	14% (energy, 6 h)	99% (0.5 A/g)	[71]
Pentyl viologen dibromide[20)], NaBr	MC|MC	PS	Battery-like	–	48.5	0/1.2	–	0.44	m_a	−3% (10,000 cycles, 2.5 A/g)	23% (energy, 6 h)	99.7% (0.5 A/g)	[70]
	MC|MC	PS	Capacitor-like	408[9)]	23[22)]	0/0.9	10 A/g	–	–		–	95.6%	[117]

(*continued on next page*)

Table 1 (*continued*)

Electrolyte[1)]	Electrode configuration[1)]	Separator	EES type	Capacity	Specific energy (Wh/kg)	Potential window (V)	Maximum rate[2)]	Specific power (kW/kg)	Normalization	Capacity stability (%)[3)]	Self-discharge[4)]	Coulombic efficiency	Ref.
Ethyl viologen dibromide[21)], H_2SO_4										+30% (1000 cycles, 2.5 A/g)			
EVBr, Tetrabutylammonium bromide, NaBr	MC|MC	PS	Battery-like	–	64	0/1.35	–	3	m_a	−10% (5000 cycles, 2 A/g)	55% (energy, 6 h) 16% (voltage, 6 h)	97% (1 A/g)	[69]

[1)]"|" symbol is used to describe the asymmetric feature. For instance, electrolyte at negative electrode | electrolyte at positive electrode and negative electrode material | positive electrode material.
[2)]In case that the specific power is not reported, the maximum applied current rate or scan rate is taken from the reference.
[3)]The negative sign is given to express the fading and the positive sign for the enhancement.
[4)]The self-discharge rates are summarized either by voltage, capacity, or energy loss after certain resting time.
[5)]Cell capacitance which is 4 times lower than the specific capacitance.
[6)]Calculated by Eq. (8).
[7)]Value from the half-cell.
[8)]No description of whether the cell was a half-cell or full-cell.
[9)]It is unclear whether the reported specific capacitance is the cell capacitance or electrode specific capacitance.
[10)]Performance is normalized by the mass of the electrolyte and electrodes in the cell, m_b.
[10)]Performance is normalized by the mass of the electrolyte, electrodes, and separator, m_c.
[12)]Performance is normalized by the volume of the electrolyte, electrodes, and separator, U_c.
[13)]Performance is normalized by the total mass of the electrode, m_e.
[14)]Performance is normalized by the projected area of the electrode, A_e.
[15)]Specific power is calculated by ESR.
[16)]In case of not reported Coulombic efficiency, the values are recalculated based on the reported GCPL curve at the lowest current density.
[17)]3.9-bis(dimethylamino)phenazothionium chloride.
[18)]1,10-dimethyl-4,40-bipyridinium dichloride.
[19)]1,10-diheptyl-4,40-bipyridinium dibromide.
[20)]1,1′-dipentyl-4,4′-bipyridinium dibromide.
[21)]1,1′-diethyl-4,4′-bipyridinium dibromide.
[22)]Calculated by Eq. (8). According to the reported value, the cell capacitance should be 204 F/g and the specific electrode capacitance of 816 F/g. The reported specific capacitance is 408 F/g.

for poor ionic conductivity leading to the necessity of ionic additives such as H_2SO_4, KOH, or KNO_3. For the prevention of redox shuttling of the neutral redox species, proton exchange membranes are required. Cation or anion exchange membranes can provide selective diffusions for the anionic or the cationic redox electrolytes, respectively.

Often, polymers are applied for liquid, gel, or solid electrolytes, where the energy storage can be enhanced by the redox activities of the conducting polymers. An essential aspect of redox active polymer gel or solid electrolytes is that the charge transfer is enabled by the solid phase components in the electrolyte [25]. In that regard, the primary distinction between polymer based redox electrolytes and conventional redox electrolytes is the location of the boundary for the electron charge transfer in the system. In the case of conventional redox electrolyte systems, the charge transfer occurs at the electrode/electrolyte interface and the redox ions diffuse to the bulk electrolyte. For polymer gel or solid electrolytes, the charge transfer boundary depends on how the electrically conductive network was established in the system. Even if there is a clear charge transfer boundary at the electrode/electrolyte interface, the diffusion of redox species to the bulk electrolyte in a gel or solid phase is slow. In a continuous charge transfer network with solid phase conducting polymers in the electrolyte, the separator is a practical boundary only if the polymer network is not connected through the pore structure of the separator. If the separator does not block the electron charge transfer, the cell will suffer from excessive self-discharge. For that reason, semi-permeable or non-porous separators are necessary [113]. The aspect of the charge transfer boundary raises the question whether one considers solid or gel electrolytes to be a part of the electrode. In this work, the solid or gel type redox electrolyte system will not be considered as a REHES system, and the focus will be on the conventional liquid type redox electrolytes.

5.1. Aqueous systems

5.1.1. Cationic redox electrolytes

The reported cationic aqueous redox electrolytes are based on lanthanides (e.g., Ce) [114], transition metals (Fe, Cu, and V) [46,60,115], and organic molecules like methylene blue [116] or viologens [11,69–71,117]. Table 1 provides an overview of the performance characteristics of reported REHES systems with aqueous cationic redox electrolytes. A lanthanide system was demonstrated with a cerium-containing acidic solution [114]; however, the major challenge of lanthanide systems is their inappropriate redox potential range. In general, lanthanides exhibit redox potentials beyond the potentials of HER and OER; for instance, the standard redox potential of a Ce^{3+}/Ce^{4+} couple (ca 1.61 V vs. SHE) is way above the standard OER potential (ca. 1.23 V vs. SHE). Additionally, the difficulty in mining and extraction processes for lanthanides is considered as an obstacle for their broad applications.

In general, transition metals exist as insoluble solid phases in neutral and basic solutions (Fig. 5C, as an example for a Fe-containing system). Therefore, an acidic medium may be necessary for transition metal-based REHES systems. In addition, transition metal ions are reduced to solid metal at low electric potential; for instance, $Zn(s)/Zn^{2+}$, $Sn(s)/Sn^{2+}$, $Mn(s)/Mn^{2+}$, $Fe(s)/Fe^{2+}$, $Ni(s)/Ni^{2+}$, or $Cu(s)/Cu^{2+}$. Such electrodeposition reactions, however, do not meet the previously given definition of REHES systems in Section 1 because they do not lead to a notable change in the oxidation state of the electrolyte. Nonetheless, they can be effectively coupled with REHES systems; for example, Zn coupled with iodide redox activities [43] and Sn coupled with the activities of a vanadium complex [13,45].

When electrodeposition reactions are applied to REHES systems, irreversible HER can occur before the reduction of transition metal ions. This undesired HER can be avoided either by introducing a large overpotential for HER or by enabling reversible hydrogen storage in microporous carbons (details in Section 4.2). In the latter case, the presence of halides in the electrolyte should be considered because their adsorption to the carbon electrode can block the active sites for reversible hydrogen reaction [43,89]. Fic et al. reported negligible electrosorption of hydrogen at ACF electrodes in 1 M KI solution as evidenced by cyclic voltammograms (Fig. 12A) [89]. In which, no visible peak for hydrogen oxidation was seen, and an irreversible reduction current was dominant through hydrogen gas evolution. Therefore, electrodeposition of transition metal ions may not be efficient for carbon electrodes in halide-containing electrolytes in cases where the desired deposition redox potential is below the HER potential. As demonstrated by us [43], cells using ACF electrodes show low Coulombic efficiencies (60–77%) in zinc and iodide-containing electrolyte (1.2 M ZnI_2). Our work indicates that the $Zn(s)/Zn^{2+}$ reaction is not effectively utilized at microporous carbon electrodes due to the irreversible HER reaction possibly caused by the blocking of active sites through iodide adsorption. Even if the electrodeposition reaction occurs without HER at the porous carbon electrode, reduction of the pore volume (also a decrease in the specific surface area) may occur. Because the solid products are often formed inside the pores [45], the pore volume must be recovered during the oxidation to maintain the system's performance stability (Fig. 12B, AC $SnF_2|VOSO_4$ AC).

An alternative solution for the undesired HER is to apply an electrode which has large overpotential, but still incorporates the redox reactions of transition metal ions. For instance (Fig. 12C, 1 M KI) [43], the onset potential of HER on a zinc disc electrode is about −1.31 V vs. Ag/AgCl, which is about 300 mV lower than that of the $Zn(s)/Zn^{2+}$ redox potential (ca. −0.97 V vs. Ag/AgCl). High Coulombic efficiency (98%) values were obtained in the cells with a zinc disc electrode (1.2 M ZnI_2), where the zinc redox reaction occurs before dihydrogen gas evolution [43].

If deposition-type redox reactions are not desired, liquid/liquid phase redox couples of transition metals such as Fe^{2+}/Fe^{3+} can be applied effectively to REHES systems [115]. Mai et al. demonstrated a high performance REHES system (73 Wh/kg, 7.5 kW/kg, normalized by m_a) with porous carbon electrodes in a $CuCl_2$ redox electrolyte by exploiting the Cu^{+}/Cu^{2+} redox couple to avoid the deposition of copper [80]. In principle, the electrosorption of transition metal cations is not favored at the positive electrode [25]; however, functionalized positive carbon electrodes with cation affinity groups can be applied to transition metal based redox couples [25,46,60,115]. Functionalized polymers with cationic or anionic functional groups can lead to enhanced electron transfer and

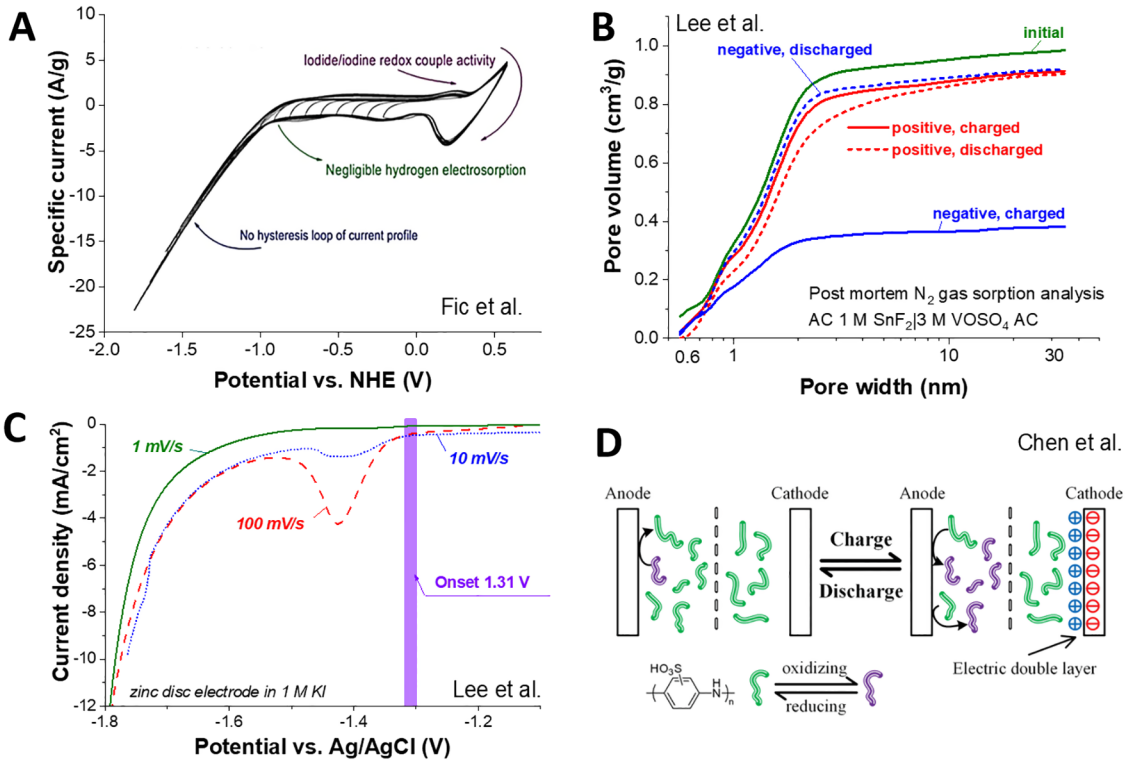

Fig. 12. Cyclic voltammograms of AC electrode in 1 M KI solution (A) and zinc disc electrode in 1 M KI (C). (B) Post mortem N_2 gas adsorption analysis for the AC electrodes prepared with different charge states. (D) Prevention of redox shuttling of dissolved conducting polymer by semi-permeable membrane.

selective electrosorption of a variety of redox and non-redox electrolytes, including ferricyanide, cyanomolybdates, ruthenium couples and other transition metal containing compounds [118].

In the case of transition metal based redox electrolytes, the use of ion selective membranes (ISM) such as proton exchange membranes (PEM) [46] and anion exchange membranes (AEM) [13] is necessary to prevent the high leakage current caused by redox shuttling. As demonstrated by Chun and Evanko et al., [11,69–71] the viologen-based REHES systems without ISM provide reasonably slow self-discharge rates enabled by strong adsorption of the viologens on porous carbon electrodes. The solubility of the organic molecules is often limited, however, and the large molecular chain can limit the power performance of the system [43,119].

5.1.2. Anionic redox electrolytes

Anionic redox electrolytes are based on halides (Br, I) [57,100,120,121], organic (indigo carmine) [122] and organometallic complexes such as ferricyanide and ferrocyanide [111,123–125], and pseudohalide (inorganic thiocyanate) [119]. The performance data of REHES systems with aqueous anionic redox electrolytes are summarized in Table 2. Whereas halide systems have been investigated since 1981 [47], the history of organometallic complexes is relatively short. Anionic redox electrolytes based on organometallic complexes were first applied to electric energy storage in 2009 by Su et al. using potassium ferricyanide and ferrocyanide [47,66]. Despite the promising performance, the major challenge of ferricyanide- or ferrocyanide-containing redox electrolytes is the high self-discharge rate caused by redox shuttling. A general sign of redox shuttling is the low Coulombic efficiency at a low current (Fig. 11A). The performance summary in Table 2 shows how the REHES systems with ferrocyanide/ferricyanide couple suffer from redox shuttling as evidenced by low Coulombic efficiency (< 90%). Only those systems with CEM or PEM showed reasonable Coulombic efficiency (> 90%) as redox shuttling was suppressed by the ion selective nature of the applied membranes [39 126].

Among anionic redox electrolytes, halide-based redox electrolytes provide an advantage regarding redox shuttling. By rather strong halide adsorption on the polymer-based or carbon-based electrodes, the level of redox shuttling can be sufficiently suppressed even without applying ISMs. While initial studies with halide ions for REHES systems had focused on the polymer-based electrodes [56], research activity has grown subsequently with the development of MC electrodes. The possible reasons are: (i) high natural abundancy of carbon, (ii) huge capacity enhancement through high specific surface area (SSA), (iii) fast charge/discharge reaction of halides in carbon micropores with electrically conductive carbon networks, and (iv) strong halide adsorption to carbon micropores. In general, the redox activity of halides at the positive electrode has been balanced either by metal deposition reactions like $Zn(s)/Zn^{2+}$ [54,55,57], viologen redox couple [69,117], and MC electrodes at the negative electrode [61,62]. In the case of coupling with metal deposition reactions, the formation of metal dendrites should be minimized by a dendrite suppression additive [127,128],

Table 2
Electric energy storage with anionic aqueous redox electrolytes. The values are taken from the full-cell configuration unless otherwise noted as half-cell. The specific capacitance values were taken unless otherwise noted as cell capacitance. Specific current is normalized to the projected area of the electrode unless otherwise noted.

Electrolyte[1)]	Electrode configuration[1)]	Separat-or	EES type	Capacity	Specific energy (Wh/kg)	Potential window (V)	Maximum rate[2)]	Specific power (kW/kg)	Normalization	Capacity stability (%)[3)]	Self-discharge[4)]	Coulombic efficiency	Ref.
Organic anion													
Indigo carmine, H_2SO_4	MWCNT|MWCNT	PS	Battery-like	50 F/g	1.7	0/1	50 mV/s, 360 mA/g	–	m_a	−30% (10,000 cycles, 360 mA/g)	–	95% (360 mA/g)[16)]	[122]
Organometallic complex													
$K_3Fe(CN)_6$, KOH	Co-Al-LDH, half-cell	–	Battery-like	712 F/g	–	−0.1/0.5 (SCE)	2 A/g	–	m_a	–33% (200 cycles, 2 A/g)[7)]	–	62% (2 A/g)[16)]	[66]
$K_3Fe(CN)_6$, KOH	M_xCl_y-CB[25)], half-.cell	–	Battery-like	12.7 F/cm^2[2,14)]	–	−0.1/0.45 (SCE)	200 mA/cm^2	–	A_e[14)]	–	–	51% (30 mA/g)[16)]	[112]
$K_3Fe(CN)_6$, KOH	MC-CF|CuO-CWT	PS	Capacitor-like	269 mF/cm^2[5)]	82 Wh/cm^2[6)]	0/1.5	–	0.01 W/cm^2	*BET SSA*	+48% (2000 cycles, 4 mA/cm^2)[7)]	–	87% (2 mA/cm^2)[16)]	[111]
$K_3Fe(CN)_6$, KOH	MC|Ni-Co-O-RGO	–	Capacitor-like	126 F/g[5)]	39[6)]	0/1.5	–	0.75	m_a	−40.2 (3000 cycles, 2.5 A/g)	–	66% (1 A/g)[16)]	[123]
$K_3Fe(CN)_6$, KCl	CNT, half-cell	–	Battery-like	28 mAh/cm^2	–	−0.6/0.6 (SCE)	0.2 A/cm^2		A_e[14)]	−10% (5000 cycles, 0.2 A/cm^2)[7)]	–	97% (0.2 A/g)	[42]
$K_3Fe(CN)_6$, Na_2SO_4	Fe_2O_3|MWCNTs-MnO_2	–	Capacitor-like	226 F/g[9)]	54.4[21)]	0/2	–	0.67	m_a	−17% (500 cycles, 200 mV/s)	–	73% (2.6 A/g)[16)]	[124]
$K_3Fe(CN)_6$	MC|MC	CEM	Capacitor-like	304 mAh/g	28.3	0/1.8	–	7.1	m_a	−20% (9000 cycles, 1 A/g)	14% (voltage, 10 h)	96% (50 mA/g)	[39]
$K_3Fe(CN)_6$, $K_4Fe(CN)_6$, KOH	NiO, half-cell	–	Battery-like	156 F/g	–	−0.1/0.55 (SCE)	2 A/g	–	–	−3.6% (1000 cycles, 2 A/g, 20 °C)[7)]	–	–	[175]
$K_3Fe(CN)_6$, $K_4Fe(CN)_6$, Na_2SO_4	DN|DN	PEM	Battery-like	73 mF/cm^2[2,7),14)]	56.5	0/2.4	–	13.7	m_a, A_e[14)]	0% (5 mA/cm^2)	–	100% (1 mA/cm^2, at 1 V)	[126]

(*continued on next page*)

Table 2 (*continued*)

Electrolyte[1)]	Electrode configuration[1)]	Separator	EES type	Capacity	Specific energy (Wh/kg)	Potential window (V)	Maximum rate[2)]	Specific power (kW/kg)	Normalization	Capacity stability (%)[3)]	Self-discharge[4)]	Coulombic efficiency	Ref.
PPD[26)], KOH|$K_3Fe(CN)_6$, KOH	AC-CFP|$Co(OH)_2$-GNS[17)]	SPD	Battery-like	205 F/g[5)]	114.5[6)]	0/2.0	–	4	m_a	0% (20,000 cycles, 10 A/g)	–	128% (1 A/g)[29)]	[176]
$K_4Fe(CN)_6$, KOH	Co-Al-LDH, half-cell	–	Battery-like	304 F/g	–	−0.1/0.5 (SCE)	2 A/g	–	m_a	−6% (200 cycles, 2 A/g)[7)]	–	61% (2 A/g)[16)]	[66]
$K_4Fe(CN)_6$	MC|MC	PS	Capacitor-like	272 F/g	–	0/1.2	0.25 A/g	–	m_a	–	–	55% (0.25 A/g)[16)]	[65]
$K_4Fe(CN)_6$, H_2SO_4	PANI-CB	–	Capacitor-like	912 F/g	20.3[6)]	0/1	–	0.55	m_a	0% (100 cycles, 5 mA/cm^2)		51% (1 mA/cm^2)[16]	[125]
Halides													
MgI_2	Zn|poly(2,5-thienylene)	–	Battery-like	–	–	–	–	–	–	–	–	–	[47]
ZnI_2	iodine-6-nylon, half-cell	–	Battery-like	–	–	−0.2/0.5 (Ag/AgCl)	–	–	–	–	–	–	[48]
ZnI_2	Zn|iodine-6-nylon	–	Battery-like	–	–	–	0.5 mA/cm^2	–	–	–	–	40% (0.5 mA/cm^2)	[49]
ZnI_2	Zn|iodine-6-nylon	CEM	Battery-like	–	–	–	2 mA/cm^2	–	–	–23% (300 cycles, 2 mA/cm^2)	–	100% (2 mA/cm2)[16)]	[50]
ZnI_2	Zn|polypyrrole-I_2	PS	Battery-like	–	–	–	6 mA/cm^2	–	–	–	90% (capacity, 8 h)	65% (6 mA/cm^2)	[53]
ZnI_2	Zn|ferrocene-DCA compound[23)]	–	Battery-like	800 mAh/g[24)]	–	–	0.5 mA/cm^2	–	m_a	–	–	97% (0.5 mA/cm^2)	[57]
ZnI_2	Zn|MC	PS	Battery-like	64 mAH/mL[12)]	226, 50.9[11)]	–	–	20, 4.7[11)]	m_a, m_c[11)]	−14% (500 cycles, 2.26 mA/cm^2)	–22% (capacity, 12 h)	96% (2.26 mA/cm^2)	[43]
ZnI_2, NH_4I	Zn|polyaniline	PS	Battery-like	143 mAh/g	–	–	120 mA	–	–	–	39% (capacity, 284 h)	95% (30 mA)	[51]
ZnI_2, NH_4I	Zn|iodine-6-nylon-CB-CF	PEM	Battery-like	60 mAh/mL[12)]	72 Wh/L[12)]	–	54 mA/cm^2-	–	V_c[12)]	–	–	100% (3 mA/cm^2)	[55]
KI	MC|MC	–	Capacitor-like	300 F/g	–	0/0.8	50 A/g	–	m_a	+28% (10,000 cycles, 1 A/g)	–	110% (0.5 A/g)[27)]	[61]

(*continued on next page*)

Table 2 (*continued*)

Electrolyte[1)]	Electrode configuration[1)]	Separator	EES type	Capacity	Specific energy (Wh/kg)	Potential window (V)	Maximum rate[2)]	Specific power (kW/kg)	Normalization	Capacity stability (%)[3)]	Self-discharge[4)]	Coulombic efficiency	Ref.
KI	MC|MC	–	Capacitor-like	234 F/g	–	0/0.8	0.5 A/g	–	m_a	–	–	–	[62]
KI	MC|MC	–	Capacitor-like	126 F/g[5)]	33	0/1.6	0.1 A/g	–	m_a	–	–	91% (0.1 A/g)	[95]
KI	MC|MC	CEM	Capacitor-like	493 F/g	33	0/1.4	–	12.3	m_a	+4% (10,000 cycles, 1 A/g)	–	98% (50 mA/g)	[44]
KI, H_2SO_4	PANI-MWCNTs|MWCNTs	–	Battery-like	726 F/g[5)]	98[6)]	0/1	–	0.5	m_a	−3% (500 cycles, 1 A/g)	–	–	[120]
KI, H_2SO_4	MC|MC	–	Battery-like	912 F/g	19	−0.2/0.8	–	1.37	m_a	+26% (4000 cycles, 5 mA/cm^2)	67% (voltage, 6 h)	89% (2 mA/cm^2)[16)]	[100]
KI, Na_2SO_4	MC|MC	–	Battery-like	604 F/g	12.3	−0.2/0.8	–	1.15	m_a	–	–	88% (2 mA/cm^2)[16)]	[100]
Ki, Li_2SO_4	A-Bi_2O_3|MC	–	Battery-like	99.5 F/g[5)]	35.4	0/1.6	6 mA/cm^2	0.5	m_a	−28% (1000 cycles, 4 mA/cm^2)	–	67% (1.5 mA/cm^2)[16)]	[177]
KI, KOH	RGO-CB|RGO-CB	–	Capacitor-like	500 F/g	44[26)]	0/0.8	–	1.62	m_a	−14% (5000 cycles, 8.3 A/g)	–	100% (1 A/g)	[121]
KI, Na_2MoO_4, H_2SO_4	MC|MC	PS	Battery-like	470 F/g[5)]	65.3	0/1	–	7	m_a	−35% (5000 cycles, 8 A/g)	–	66% (4 A/g)[16)]	[178]
$VOSO^4$|KI	MC|MC	PEM	Capacitor-like	500 F/g[5)]	20	0/0.8		2	–	–	–	100% (0.5 A/g)	[46]
LiI	MC|MC	–	Capacitor-like	178 F/g	–	0/0.8	0.5 A/g	–	m_a	–	–	–	[62]
NaI	MC|MC	–	Capacitor-like	203 F/g	–	0/0.8	0.5 A/g	–	m_a	–	–	–	[62]
RbI	MC|MC	–	Capacitor-like	220 F/g	–	0/0.8	0.5 A/g	–	m_a	–	–	100% (0.5 A/g)[16)]	[62]
CsI	MC|MC	–	Capacitor-like	234 F/g	–	0/0.8	0.5 A/g	–	m_a	–	–	–	[62]
$ZnBr_2$	Zn|polypyrrole-Br_2	PS	Battery-like	–	–	–	6 mA/cm^2	–	–	–	72% (capacity, 16 h)	85% (6 mA/cm^2)	[53]
$ZnBr_2$, NH_4Br	Zn|polyaniline	PS	Battery-like	100 mAh/g	–	–	120 mA-	–	–	–	60% (331 h)	99% (30 mA)[16)]	[52]

(*continued on next page*)

Table 2 (*continued*)

Electrolyte[1)]	Electrode configuration[1)]	Separator	EES type	Capacity	Specific energy (Wh/kg)	Potential window (V)	Maximum rate[2)]	Specific power (kW/kg)	Normalization	Capacity stability (%)[3)]	Self-discharge[4)]	Coulombic efficiency	Ref.
$ZnBr_2$, NH_4Cl	CC|Polyacrylamide-MC	PEM	Battery-like	–	40 Wh/L	–	2 mA/cm^2	–	–	–	–	85% (2 mA/cm^2)	[56]
KBr, H_2SO_4	MC|MC	–	Battery-like	572 F/g	11.6	−0.2/0.8	–	2.52	m_a	–	–	82% (2 ma/cm^2)[16)]	[100]
KBr, Methyl viologen dichloride[18)]	MC|MC	PS	Battery-like	49.8, 13.3 mAh/g[10)]-	51, 13.9[10)]	0/1.4	–	0.52, 0.14[10)]	m_a, m_b[10)]	–	76% (energy, 6 h)	99% (0.5 A/g)	[71]
KBr, Heptyl viologen dichloride[19)]	MC|MC	PS	Battery-like	44.0, 12.1 mAh/g[10)]	39.3, 10.8[10)]	0/1.4	–	0.45, 0.12[10)]	m_a, m_b[10)]	–	14% (energy, 6 h)	99% (0.5 A/g)	[71]
NaBr, Pentyl viologen dibromide[20)]	MC|MC	PS	Battery-like	–	48.5	0/1.2	–	0.44	m_a	−3% (10,000 cycles, 2.5 A/g)	23% (energy, 6 h)	99.7% (0.5 A/g)	[70]
Ethyl viologen dibromide[21)], H_2SO_4	MC|MC	PS	Capacitor-like	408 F/g[9)]	23[22)]	0/0.9	10 A/g	–	–	+30% (1000 cycles, 2.5 A/g)	–	95.6% (2.5 A/g)	[117]
EVBr, Tetrabutylammonium bromide, NaBr	MC|MC	PS	Battery-like	–	64	0/1.35	–	3	m_a	−10% (5000 cycles, 2 A/g)	55% (energy, 6 h) 16% (voltage, 6 h)	97% (1 A/g)	[69]
Pseudohallide													
KSCN	CB|CB	PS	Capacitor-like	–	10	0/1.6	–	8	m_a	−31% (10,000 cycles,-)	−45% (voltage, 8 h)	–	[119]
NaSCN	MC|MC	PS	Capacitor-like	64 F/g	–	0/1.4	2 A/g	–	m_a	–	–	96% (1 A/g)	[119]
LiSCN	MC|MC	PS	Capacitor-like	97 F/g	–	0/1.6	2 A/g	–	m_a	–	–	97% (1 A/g)	[119]
NH_4SCN	MC|MC	PS	Capacitor-like	43	–	0/1.2	2 A/g	–	m_a	−13% (10,000 cycles,-)	–	96% (1 A/g)	[119]
Redox surfactants													
TPAB, KOH	MC-CB|MC-CB	PS	Capacitor-like	161 F/g	–	–	50 A/g	–	m_a	–33% (5000 cycles, 1 A/g)	62% (voltage, 22 h)	–	[131]
TPAI, KOH	MC-CB|MC-CB	PS	Capacitor-like	165 F/g	–	–	50 A/g	–	m_a	−5% (5000 cycles, 1 A/g)	83% (voltage, 22 h)	–	[132]

(*continued on next page*)

Table 2 (*continued*)

Electrolyte[1)]	Electrode configuration[1)]	Separator	EES type	Capacity	Specific energy (Wh/kg)	Potential window (V)	Maximum rate[2)]	Specific power (kW/kg)	Normalization	Capacity stability (%)[3)]	Self-discharge[4)]	Coulombic efficiency	Ref.
TPAI, Na_2SO_4	MC|MC	PS	Capacitor-like	81 F/g	–	0/0.6	10 A/g	–	m_a	–	–	99% (50 mA/g)	[35]
Sodium lignosulfonates, H_2SO_4	MC-CB|MC-CB	–	Capacitor-like	181 F/g[13)]	–	0/0.8	10 A/g	–	m_e[13)]	–	–	–	[133]

[1)]"|" symbol is used to describe the asymmetric feature. For instance, electrolyte at negative electrode | electrolyte at positive electrode and negative electrode material | positive electrode material.
[2)]In case that the specific power is not reported, the maximum applied current rate or scan rate is taken from the reference.
[3)]The negative sign is given to express the fading and the positive sign for the enhancement.
[4)]The self-discharge rates are summarized either by voltage, capacity, or energy loss after certain resting time.
[5)]Cell capacitance which is 4 times lower than the specific capacitance.
[6)]Calculated by Eq. (8).
[7)]Value from the half-cell.
[8)]No description of whether the cell was a half-cell or full-cell.
[9)]It is unclear whether the reported specific capacitance is the cell capacitance or electrode specific capacitance.
[10)]Performance is normalized by the mass of the electrolyte and electrodes in the cell, m_b.
[11)]Performance is normalized by the mass of the electrolyte, electrodes, and separator, m_c.
[12)]Performance is normalized by the volume of the electrolyte, electrodes, and separator, U_c.
[13)]Performance is normalized by the total mass of the electrode, m_e.
[14)]Performance is normalized by the projected area of the electrode, A_e.
[15)]Specific power is calculated by ESR.
[16)]In case of not reported Coulombic efficiency, the values are recalculated based on the reported GCPL curve at the lowest current density.
[17)]Graphene-supported $Co(OH)_2$ nanosheet.
[18)]1,10-dimethyl-4,40-bipyridinium dichloride.
[19)]1,10-diheptyl-4,40-bipyridinium dibromide.
[20)]1,1′-dipentyl-4,4′-bipyridinium dibromide.
[21)]1,1′-diethyl-4,4′-bipyridinium dibromide.
[22)]Calculated by Eq. (8). According to the reported value (408 F/g), the cell capacitance should be 204 F/g or the specific electrode capacitance of 816 F/g.
[23)]Inclusion compound of ferrocene and deoxycholic acid (DCA).
[24)]Normalized by the mass of the inclusion compound.
[25)]Colloid electrodes prepared by mixing transition metal chloride salts ($CoCl_2{\cdot}6H_2O$, $CuCl_2{\cdot}2H_2O$ $NiCl_26H_2O$, or $FeCl_3{\cdot}6H_2O$), carbon black, and poly(vinylidene fluoride).
[26)]Energy density is reported by single electrode mass by Eq. (8) with the specific electrode capacitance. This calculation brings 4 times higher value than the value obtained by the cell capacitance with total mass via Eq. (8).
[27)]Coulombic efficiency should not exceed 100% in a full-cell. The discharging and charging current might not have been the same due to the device accuracy.

Table 3
Electric energy storage with neutral aqueous redox electrolytes. The values are taken from the full-cell configuration unless otherwise noted as half-cell. The single electrode specific capacitance values were taken unless otherwise noted as cell capacitance. Specific current is normalized to the projected area of the electrode unless otherwise noted.

Electrolyte[1)]	Electrode configuration[1)]	Separator	EES type	Capacity	Specific energy (Wh/kg)	Potential window (V)	Maximum rate[2)]	Specific power (kW/kg)	Normalization	Capacity stability[3)]	Self-discharge[4)]	Coulombic efficiency	Ref.
HQ, H_2SO_4	MC|MC	–	–	901 F/g	31.32[6)]	0/1	88 mA/cm^2	–	m_a	−65% (4000 cycles, 4.42 mA/cm^2)	–	–	[64]
HQ, H_2SO_4	MC|MC	PS	Capacitor-like	220 F/g[5)]	30.6[6)]	0/1	85 mA/cm^2	–	m_a	–	–	92% (8.8 mA/cm^2)[16)]	[63]
HQ, H_2SO_4	RGO-PANI|RGO-PANI	PS	Battery-like	553 F/g	–	0/0.7	30 A/g	–	m_a	−36% (50,000 cycles, 10 A/g)	–	90% (5 A/g)[16)]	[179]
HQ, H_2SO_4	PANI-CB|PANI-CB	–	Battery-like	773 F/g	–	0/0.7-	30 A/g	–	m_a	−48% (10,000 cycles, 10 A/g)	–	86% (10 A/g)[16)]	[180]
HQ, H_2SO_4	CNT, half-cell	PEM	Battery-like	2250 F/g[13)]	–	0/1 (SCE)	4 A/g	–	m_e[13)]	−50% (500 cycles, 5 mV/s)	–	61% (4 A/g)[16)]	[181]
HQ, H_2SO_4	PANI-SnO_2[8)]	–	Capacitor-like	857 F/g	116.6[18)]	−0.5/0.5	–	7.3	m_a	−17.8% (2000 cycles, 0.5 A/g)	–	94% (0.5 A/g)[16)]	[136]
HQ, H_2SO_4	GHG|GHG	PEM	Capacitor like	88.5 F/g[5)]	–	0/0.8	6.9 A/g	–	m_a	–	96% (voltage, 12 h)	75% (1 A/g)[16)]	[103]
HQ, BQ, H_2SO_4	PEB|PEB	PS	Battery-like	2646 F/g	–	0/0.65	30 mA/cm^2	–	m_a	+ 15% (50,000 cycles, 12.5 mA/cm^2)	–	93% (1 mA/cm^2)[16)]	[137]
AQDS, KNO_3	MC|MC	–	Capacitor-like	225 F/g	21.2[6)]	0/1.8	–	0.41	m_a	–	–	98% (1 A/g)[16)]	[182]
Brominated hydroquinones, KOH	MC-CB|MC-CB	PS	Capacitor-like	314 F/g	13	0/1.1	0.5 A/g	–	m_a	−25% (5000 cycles, 2 A/g)	–	88% (0.5 A/g)[16)]	[135]

(*continued on next page*)

Table 3 (*continued*)

Electrolyte[1)]	Electrode configuration[1)]	Separator	EES type	Capacity	Specific energy (Wh/kg)	Potential window (V)	Maximum rate[2)]	Specific power (kW/kg)	Normalization	Capacity stability[3)]	Self-discharge[4)]	Coulombic efficiency	Ref.
Rutin, H_2SO_4	MC|MC	PS	Capacitor-like	86 F/g[5)]	11.9[6)]	0/1	–	5	m_a	−4.4% (5000 cycles, 10 A/g)	–	68% (1 A/g)[16)]	[138]
Pyrocatechol, H_2SO_4	MC|MC	PS	Capacitor-like	136 F/g[5)]	18.9[6)]	0/1	–	5	m_a	−3.6% (5000 cycles, 10 A/g)	–	58% (1 A/g)[16)]	[138]
Pyrocatechol, H_2SO_4	NMC-CB|NMC-CB	PS	Battery-like	628 F/g	–	0/1	10 A/g	–	m_a	+13.5% (6000 cycles, 5 A/g)	80% (voltage, 12 h)	100% (0.5 A/g)[16)]	[173]
Catechol, H_2SO_4	PANI-RGO|PANI-RGO	PS	Battery-like	409 F/g[5)]	81.81[6)]	0/1.2	–	7.7	m_a	−10.3% (5000 cycles, 10 A/g)[7)]	–	90% (1 A/g)[16)]	[134]
PPD, KOH	MnO_2|MnO_2	–	Battery-like	325 F/g[13)]	10.12[6),13)]	−0.5/0.5	–	2.8[13)]	m_e[13)]	−25 (5000 cycles, 1 A/g)	–	94 (1 A/g)[16)]	[98]
PPD, KOH	MnO_2-CB, half-cell	–	Capacitor-like	156 F/g, −20 °C	–	−0.4/0.55 (SCE)	2 A/g	–	–	−16% (600 cycles, 2 A/g, −20 °C)	–	81% (2 A/g, −20 °C)[16)]	[183]
PPD, KOH	MC-GP|MC-GP	–	Capacitor-like	605 F/g[13)]	19.86[6),13)]	0/1	–	17.0[15),13)]	m_e[13)]	−5.5% (4000 cycles,	62% (voltage, 20 h)	75% (-)[16)]	[184]
PPD, KOH	MC-GP, half-cell	–	Battery-like	852.3 F/g	–	−1/0 (SCE)	10 A/g	–	m_a	−29% (5000 cycles, 40 A/g)	–	76% (2 A/g)[16)]	[185]
PPD, KOH	NC-TEG[17)], half-cell	–	Battery-like	636 F/g	–	−1/0 (Ag/AgCl)	100 mV/s	–	m_a	−12.6% (10,000 cycles, -)	–	90% (1 A/g)[2),16)]	[186]
PPD, KOH|$K_3Fe(CN)_6$, KOH	AC-CFP|Co$(OH)_2$-GNS	SPD	Battery-like	205 F/g[5)]	114.5[6)]	0/2.0	–	4	m_a	0% (20,000 cycles, 10 A/g)	–	128% (1 A/g)[19)]	[176]
MPD, KOH	MC-GP|MC-GP		Battery-like	78 F/g[5),13)]	9.99[13)]	−0.5/0.5	–	5.78[15),13)]	m_e[13)]	−9.3% (10,000 cycles, 1 A/g)		100% (0.5 A/g)[16)]	[99]
PPD, H_2SO_4	MC-CB|MC-CB	–	Battery-like	121 F/g[5)], −18 °C	37.8[6)], −18 °C	0/1.5	–	1.5, −18 °C	m_a	–	–	77% (0.5 A/g)[16)]	[187]

(*continued on next page*)

Table 3 (*continued*)

Electrolyte[1)]	Electrode configuration[1)]	Separator	EES type	Capacity	Specific energy (Wh/kg)	Potential window (V)	Maximum rate[2)]	Specific power (kW/kg)	Normalization	Capacity stability[3)]	Self-discharge[4)]	Coulombic efficiency	Ref.
Soluble conducting polymer													
SPANI, H_2SO_4	GHG|GHG	SPM	Capacitor-like	64 F/g[5),13)]	–	0/0.8	5.22 A/g	–	m_e[13)]	−1% (1000 cycles, 1 A/g)	79% (voltage, 14 h)	100% (0.26 A/g)[16)]	[113]
p-nitroaniline, KOH	Carbon-DMG, half-cell	–	Battery-like	386 F/g	–	−1/0 (SCE)	40 A/g	–	m_a	+13% (5000 cycles, 10 A/g)	–	91% (3 A/g)[16)]	[139]

[1)]"|" symbol is used to describe the asymmetric feature. For instance, electrolyte at negative electrode | electrolyte at positive electrode and negative electrode material | positive electrode material.
[2)]In case that the specific power is not reported, the maximum applied current rate or scan rate is taken from the reference.
[3)]The negative sign is given to express the fading and the positive sign for the enhancement.
[4)]The self-discharge rates are summarized either by voltage, capacity, or energy loss after certain resting time.
[5)]Cell capacitance which is 4 times lower than the specific capacitance.
[6)]Calculated by Eq. (8).
[7)]Value from the half-cell.
[8)]No description of whether the cell was a half-cell or full-cell.
[9)]It is unclear whether the reported specific capacitance is the cell capacitance or electrode specific capacitance.
[10)]Performance is normalized by the mass of the electrolyte and electrodes in the cell, m_b.
[11)]Performance is normalized by the mass of the electrolyte, electrodes, and separator, m_c.
[12)]Performance is normalized by the volume of the electrolyte, electrodes, and separator, U_c.
[13)]Performance is normalized by the total mass of the electrodes, m_e.
[14)]Performance is normalized by the projected area of the electrode, A_e.
[15)]Specific power is calculated by ESR.
[16)]In case of not reported Coulombic efficiency, the values are recalculated based on the reported GCPL curve at the lowest current density.
[17)]Nitrogen-doped carbon layer coated thermally exfoliated graphene (TEG).
[18)]Calculated by Eq. (8). However, the capacitance used for their calculation was specific capacitance. In this case, a four-fold error arises because the cell capacitance is 4 times higher than the specific capacitance.
[19)]The Coulombic efficiency should not exceed 100% in a full-cell. The discharging and charging current might not have been the same due to the device accuracy.

nanoporous or nonporous separators [23,129], or an optimized cell design [130]. For coupling with an MC electrode, careful charge balancing is required since hydrogen storage will not effectively occur due to active sites pre-occupied by adsorbed halides (Fig. 12A) [95].

Since bromide reactions have a higher redox potential than iodide reactions, bromide-based redox electrolytes are more beneficial for REHES systems; the high redox potential at the positive electrode is essential for maximizing the specific energy of the system as discussed in Section 3.1. However, the standard redox potential of bromide activities is very close to that of the oxygen evolution potential, and bromide has corrosive features and is volatile. Therefore, bromide-based redox electrolytes must be used with care [69]. Despite the lower redox potential, iodide-based redox electrolytes may be preferred as they are more stable and safer as compared to bromide-based systems. Often, enhanced performance after long-term cycles has been reported for iodide-based REHES systems. The possible reason is the improved accessibility of iodide at the carbon surface or potential shifts of the electrodes after long-term cycles [37,43,61].

Recently, a REHES system with a pseudohalide (inorganic thiocyanates) was introduced by Gorska et al. [119]. This work shows that the thiocyanate system still suffers from self-discharge but at a significantly lower rate as compared to that of organometallic systems. Most probably, pseudohalides adsorb to porous carbon electrodes in the same manner as halides. Hence, pseudohalide-based redox electrolytes may provide a flexible choice for anionic redox electrolytes without applying ISM.

One attractive approach is to introduce redox active surfactants such as tetrapropylammonium bromide (TPAB) [131], tetrapropylammonium iodide (TPAI) [35,132], and sodium lignosulfonates [133]. These redox surfactants can be applied to hydrophobic electrode materials, particularly, in the case of highly porous materials. In addition, the capacity of the system can be enhanced by the redox activity of the electrolyte. However, the concentration of redox active surfactants should be adjusted carefully to avoid exceeding their critical micelle concentration as micelles may block the active sites of the porous electrode [35,132]. The use of redox active surfactants seems to be particularly promising for flow electrode applications [32,33,35].

5.1.3. Neutral redox electrolytes

The known neutral redox electrolytes for the REHES systems are based on the redox couples of organic compounds such as HQ [134–137], rutin [138], and catechol [134], and soluble conducting polymers like sulfonated polyaniline (SPANI) [113] or p-nitroaniline (PNA) [139]. The performance of REHES systems with aqueous neutral redox electrolytes is summarized in Table 3. Due to charge neutrality, the neutral organic compounds cannot be applied effectively to the energy storage systems without the aid of supporting ions. To provide sufficient ionic conductivity and the possible benefits of EDL formation with highly porous carbon electrodes, supporting ionic species are required; for instance, H_2SO_4 (acidic), KNO_3 (neutral), and KOH (basic) can be used.

In comparison to cationic and anionic redox electrolytes, REHES systems with neutral redox electrolytes require PEMs to prevent the redox shuttling of neutrally charged redox couples. Since PEMs are more expensive than AEMs and CEMs, the need for PEMs is a major drawback of neutral redox electrolyte systems. Among the reported REHES systems with neutral redox electrolytes, just a few studies can be found where PEMs were applied (Table 3). The reported systems without PEMs, in general, provide insufficient Coulombic efficiency ($< 90\%$) even at a high current rate (> 0.5 A/g). The HQ-based REHES system with H_2SO_4 electrolyte reported by Chen et al. demonstrated a greatly suppressed redox shuttling rate after a PEM (Nafion 117) was introduced; however, the system still suffered from a rapid self-discharge (96% voltage loss after 12 h resting time) [103].

Another approach to prevent the redox shuttling was demonstrated by Chen et al. (Fig. 12D) who used polymeric SPANI as a redox electrolyte [113]. This work shows that the migration of polymeric SPANI can be suppressed by a semipermeable membrane (SPM) while selectively allowing the free migration of the supporting ions like SO_4^{2-} and H^+. This concept is beneficial in terms of lower price than that of proton exchange membranes. So far, only a few cases have been reported for soluble conducting polymers with limited solubility (< 100 mM). In general, highly concentrated redox species in the electrolyte are desired to enhance the charge storage capacity. Therefore, a broader investigation of new, soluble conducting polymers with higher solubility is necessary.

Generally, we see that for REHES systems, cationic and anionic redox electrolytes are more attractive than neutral redox electrolytes due to the favorable electrosorption of ions with oppositely charged electrodes [25]. Furthermore, the low solubility of the neutral redox electrolytes is a limiting factor for practical applications.

5.2. Non-aqueous redox electrolyte system

The main appeal of non-aqueous redox electrolytes is the high operating cell voltage (1.25–3.7 V, Table 4) in comparison to aqueous systems. With IL electrolytes, redox activities can be introduced to carbon-based double-layer capacitors as additives for the enhancement of charge storage capacity and specific energy. As demonstrated by Sun et al., [68] copper can be added to 1-ethyl-3-methylimidazolium tetrafluoroborate ([EMIm]BF_4) by dissolution of copper chloride (0.36 M). As a result, the capacity of the system was enhanced by reversible redox reactions of Cu (II)/Cu(I)/Cu(s) [68]. Similar work had been reported with the addition of 0.3 M hydroquinone to a protic IL, triethylammonium bis(trifluoromethane)sulfonimide ([TEA]TFSI) [140].

For a significant contribution of redox couples in an IL, a high concentration of the redox active species is required. In one approach, Yamazaki et al. [141] applied a mixed IL of 1-ethyl-3-methylimidazolium bromide ([EMIm]Br) and ([EMIm]BF_4) with a concentration of [EMIm]Br of 1 M in [EMIm]BF_4. Owing to the strong redox activities of Br_2/Br_3^- and Br^- at 0.5 V vs. Pt at the positive electrode, the capacity of the system was enhanced significantly from 18 mAh/g to 33 mAh/g (normalized to m_e). Furthermore, a low level of redox shuttling was observed as inferred by a low leakage current (same level as that of a double-layer capacitor) and high Coulombic efficiency of 99.7% (at 100 mA/g). In contrast, HQ and Cu(II)-containing ILs showed lower Coulombic efficiencies ($< 80\%$) indicating redox shuttling issues. The negligible level of redox shuttling by [EMIm]Br/[EMIm]BF_4 can be

Table 4
Electric energy storage with non-aqueous redox electrolytes. The values are taken from the full-cell configuration unless otherwise noted as half-cell. The single electrode specific capacitance values were taken unless otherwise noted as cell capacitance. Specific current is normalized to the projected area of the electrode unless otherwise noted.

Electrolyte[1)]	Electrode configuration[1)]	Separator	EES type	Capacity	Specific energy (Wh/kg)	Potential window (V)	Maximum rate[2)]	Specific power (kW/kg)	Normalization	Capacity stability[3)]	Self-discharge[4)]	Coulombic efficiency	Ref.
Il with redox additives													
Cu(II) IL[17)], [EMIm]BF_4	MC, half-cell	PS	Capacitor-like[d]	225 F/g	45 Wh/kg[6)]	0/2 (SCE)	5 mA/cm^2	0.22	m_a	−9% (500 cycle,-)	–	53% (1 mA/cm^2)[16)]	[68]
HQ IL[18)], [TEA]TFSI,	MC|MC	PS	Capacitor-like	70 F/g[9)]	31.22 Wh/kg[22)]	0/2.5	14.2 mA/cm^2	–	m_a	−15% (1000 cycles, 4.25 mA/cm^2)	–	77% (0.57 mA/cm^2)[16)]	[140]
Redox active ILs													
[EMIm]Br IL[19)], [EMIm]BF_4	MC|MC	PS	Capacitor-like	59 F/g[13)]	–	0.5/2.0	1 A/g	–	m_e[13)]	−2% (10,000 cycles, 500 mA/g)	–	99.7% (100 mA/g)	[141]
Biredox IL[20)], [BMIm]TFSI	MC|MC	Li-conducting ceramic	Capacitor-like	200 F/g[13)]	70 Wh/kg[6),13)]	0/2.8	–	5 kW/kg[23)]	m_e[13)]	−17% (2000 cycles, 1.5 A/g)	37% (voltage, 50 h)	100% (1.5 A/g)[16)]	[146]

(*continued on next page*)

Table 4 (*continued*)

Electrolyte[1)]	Electrode configuration[1)]	Separator	EES type	Capacity	Specific energy (Wh/kg)	Potential window (V)	Maximum rate[2)]	Specific power (kW/kg)	Normalization	Capacity stability[3)]	Self-discharge[4)]	Coulombic efficiency	Ref.
Organic solvent													
[EMIm]$FcNTf_2$ in AN[21)]	MC-CB-GP|MC-CB-GP	PS	Capacitor-like	–	32.5 Wh/kg[13)]	0/2.5	722 mA/g	–	m_e[13)]	–	23% (voltage, 0.58 h)	83% (0.56 mA/cm^2)[16)]	[145]
PPD, $LiClO_4$ in AC	MC-GP|MC-GP	–	Capacitor-like	69 F/g[5),13)]	54.5 Wh/kg[6),13)]	−1.25/1.25	500 mA/g	13.11 kW/kg[15)]	m_e[13)]	−7% (5000 cycles, 0.5 A/g)	–	100% (500 mA/g)[16)]	[188]

[1)]"|" symbol is used to describe the asymmetric feature. For instance, electrolyte at negative electrode | electrolyte at positive electrode and negative electrode material | positive electrode material.
[2)]In case that the specific power is not reported, the maximum applied current rate or scan rate is taken from the reference.
[3)]The negative sign is given to express the fading and the positive sign for the enhancement.
[4)]The self-discharge rates are summarized either by voltage, capacity, or energy loss after certain resting time.
[5)]Cell capacitance which is 4 times lower than the specific capacitance.
[6)]Calculated by Eq. (8).
[7)]Value from the half-cell.
[8)]No description of whether the cell was a half-cell or full-cell.
[9)]It is unclear whether the reported specific capacitance is the cell capacitance or electrode specific capacitance.
[10)]Performance is normalized by the mass of the electrolyte and electrodes in the cell, m_b.
[11)]Performance is normalized by the mass of the electrolyte, electrodes, and separator, m_c.
[12)]Performance is normalized by the volume of the electrolyte, electrodes, and separator, U_c.
[13)]Performance is normalized by the total mass of the electrodes, m_e.
[14)]Performance is normalized by the projected area of the electrode, A_e.
[15)]Specific power is calculated by ESR.
[16)]In case of not reported Coulombic efficiency, the values are recalculated based on the reported GCPL curve at the lowest current density.
[17)]Cu(II) containing 1-ethyl-3-methylimidazolium tetrafluoroborate ([EMIm]BF_4).
[18)]HQ containing triethylammonium bis(trifluoromethane)sulfonimide ([TEA]TFSI).
[19)]1-ethyl-3-methylimidazolium bromide ([EMim)Br) in [EMIm]BF_4.
[20)]biredox IL comprising a perfluorosulfonate anion bearing anthraquinone and a methyl imidazolium cation bearing 2,2,6,6-tetramethyl-piperidinyl-1-oxyl.
[21)]1-ethyl-3-methylimidazolium ferrocenylsulfonyl-(trifluoromethylsulfonyl)-imide in acetonitrile (AN).
[22)]According to the reported specific energy, the system should give an electrode specific capacitance of 140 F/g or a cell specific capacitance of 35 F/g. Instead, the specific capacitance of 70 F/g is reported.
[23)]Specific power is obtained from the CV by multiplying specific energy and scan rate and by dividing with the potential window.

explained by strong adsorption of bromide to the electrode materials [71,142–144]. The adsorption of bromide on the electrode prevents the diffusion of oxidized bromide to the negative electrode. The relation between the adsorption of halide ions and redox shuttling mechanisms in IL systems are also in line with the thorough investigations reported on halide adsorptions on porous carbon electrodes in aqueous systems [43,71].

Another approach to utilize redox activities had been demonstrated by Xie et al. with the redox-active IL dissolved in an organic electrolyte (acetonitrile, AN) [145]. Through a highly concentrated 3 M 1-ethyl-3-methylimidazolium ferrocenylsulfonyl-(trifluoromethylsulfonyl)-imide ([EMIm]FcNTf), the capacity of the positive electrode was enhanced significantly owing to the reversible oxidation of $[FcNTf]^-$ anions to $[Fc^+NTf^-]^0$ at around 1.7 V vs. Pt. However, like the bromide, HQ, and Cu containing IL systems, introducing redox couples only at one electrode causes an imbalanced potential development leading to the rapid potential surge at the negative electrode. For effective charge balance, a bi-redox IL was introduced by Mourad et al. with a perfluorosulfonate anion bearing anthraquinone (AQ) and a methyl imidazolium cation bearing 2,2,6,6-tetramethyl-piperidinyl-1-oxyl (TEMPO) [146]. A high specific energy of 70 Wh/kg (normalized to m_e) was obtained after the charges of the redox activity of AQ at the negative electrode and the redox activity of TEMPO at the positive electrode were balanced. The uniqueness of the latter work is that the pure bi-redox IL works as a redox active electrolyte at 60 °C without supporting ions like [BMIm]TFSI, exhibiting a capacitance of 370 F/g (normalized to m_e). In comparison, a lower value was obtained (210 F/g, normalized to m_e) with the 0.5 M bi-redox IL in supporting [BMIm]TFSI at room temperature.

Most IL systems suffer from low specific power originating from low ionic conductivity, which is related strongly to the high viscosity of these electrolytes (especially at or below room temperature) [26]. For REHES systems with redox ILs, this issue is particularly critical when the redox species are introduced as additives [141]. In that regard, organic redox electrolyte systems can play an important role by providing higher operating cell voltages than can aqueous systems, and better power performance (10 kW/kg, Table 4) than redox ILs. For instance, upon the introduction of 0.05 M P-phenylenediamine (PPD) to 1 M $LiClO_4$ in AN, a cell with activated carbon electrodes showed a specific energy of 55 Wh/kg (normalized by m_e) while still providing a high specific power up to 13 kW/kg (normalized by m_e).

Compared to aqueous redox electrolyte systems, non-aqueous redox electrolyte systems remain far less investigated. As shown by Gong et al., [147] this leaves room for more exploration. In the latter work, possible redox couples in non-aqueous electrolyte systems were surveyed with 35 metal based redox pairs and 17 metal-free redox pairs. Therefore, there remain many possible new REHES systems with organic solutions.

5.3. Diffusion, adsorption, and kinetics of REHES

The use of highly porous carbon electrodes allows the design of REHES systems with attractive performance values. For a comprehensive understanding of the latter, it necessary to study fundamental aspects of redox kinetics, ion diffusion, and adsorption of redox ions under the unique conditions of nanoconfinement inside carbon pores. The redox kinetics in carbon micropores are known to be different from processes occurring on flat surfaces, where we can assume semi-infinite planar diffusion [148–154]. For example, the works of Narayanan, Bandaru, and coworkers explained the high power handling performance of REHES systems by adopting key concepts of thin-layer electrochemistry (TLE) [27,42]. The TLE theory, initially developed by Hubbard and Anson in the 1960s, addresses electrochemical processes in the confined diffusion length, or thin layer [148,149]. The core aspect of the theory is the concept of diffusion-less reaction under thin-layer conditions. Further fundamental studies with advanced simulations and models indicate that the diffusion-less TLE behavior is an intrinsic feature. Hence, it should not be interpreted as a kinetic enhancement leading to the conclusion of a catalytic effect [151,152,154]. Nonetheless, TLE behavior is considered to be a critical factor for the high power performance of REHES systems with microporous carbon electrodes.

The diffusion of redox ions is an important aspect not only for redox kinetics, but also for efficient energy storage. The diffusion of redox ions may lead to a severe energy loss caused by redox shuttling from one electrode compartment to the other [39,71,103]. While the use of ion selective membranes can prevent redox shuttling, an alternative solution is to capitalize on strong adsorption of halide species in carbon micropores [69–71,89]. Thereby, an effective immobilization of otherwise mobile redox ions can be achieved. In the following sections, the diffusion, adsorption, and redox kinetics on REHES systems will be discussed.

5.3.1. Self-discharge and time-dependent potential decay

Self-discharge is an important parameter with an impact on energy and charge efficiency, life time of the system, and safety [109,110,155–158]. The theories and models on self-discharge mechanisms for supercapacitors were pioneered by Conway et al. [110,159] and recent progress has been summarized by Andreas et al. [109] and Ike et al. [160]. In this section, the current state-of-the-art of time-dependent potential decay and self-discharge will be reviewed, and be categorized as follows:

(i) Self-discharge due to short-circuit of the electrodes
(ii) Self-discharge due to activation-controlled Faradaic processes.
(iii) Self-discharge due to diffusion-controlled Faradaic processes.
(iv) Potential decay due to charge non-uniformity.

Type-(i) self-discharge occurs due to the imperfect sealing of the positive and negative electrodes which causes short-circuit between the electrodes. Therefore, it is often considered to be a trivial origin of self-discharge which is not related to the electrochemical system [109,110]. To prevent this type of self-discharge, one needs to fabricate a cell with complete insulation and tight

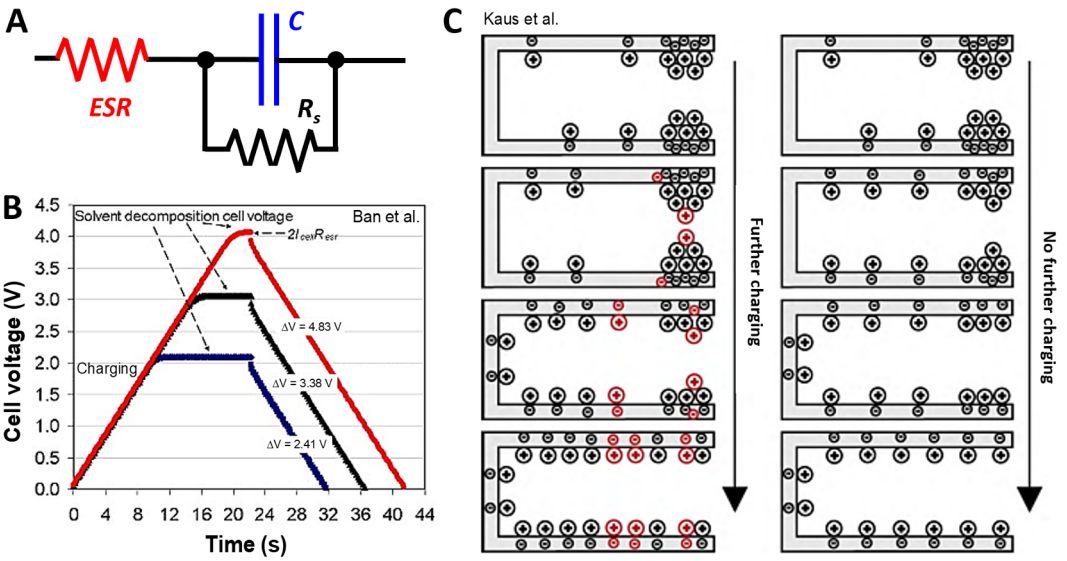

Fig. 13. Various models and simulations for self-discharge mechanisms of supercapacitors. (A) A simple RC model for the self-discharge mechanisms with the short-circuiting element in the cell. (B) Self-discharge mechanisms due to the solvent decomposition. Reprinted from Ref. [189], Copyright (2018), with permission from Elsevier. (C) Charge redistribution theory for double-layer capacitors. Reprinted from Ref. [166], Copyright (2017), with permission from Elsevier.

sealing between the electrodes. The time-dependent OCP, V_t, can be derived from a simple *RC* circuit model where the short-circuiting resistance element, R_s, is introduced (Fig. 13A) [110,161]. A characteristic of this mechanism is that $\ln(V_t)$ has a linear relationship with time (t), as seen in Eq. (13):

$$ln\left(\frac{V_t}{V_i}\right) = -\frac{t}{R_s C} \tag{13}$$

where V_i is the initial potential and C is the double-layer capacitance.

At equilibrium, the leakage current (i_s) at an applied potential (V_a) can be defined via Eq. (14):

$$i_s = \frac{V_a}{R_s} \tag{14}$$

The type-(ii) mechanism originates from the non-diffusion-controlled reaction with the electrode or electrolyte and exhibits no transport limitations. The latter effects are enabled when the reaction species are part of the electrode or are highly concentrated [156,161]; for instance, decomposition of a solvent (Fig. 13B). In the case of the activation-controlled Faradaic process, the OCP varies linearly with $\ln(t)$, as seen from Eq. (15) [110,161].

$$V_t = \frac{RT}{\alpha F} ln\left(\frac{RTC}{\alpha F i_0}\right) - \frac{RT}{\alpha F} ln\left(t + \frac{Ct_0}{i_0}\right) \tag{15}$$

where i_0 is the exchange current density in A/cm^2 which passes reversibly in both the anodic and cathodic directions, t_0 is an integration constant, and α is the transfer coefficient. The leakage current of this type follows the Tafel equation which is a function of overpotential (η), as seen in Eq. (16) [161]:

$$i_s = i_0 e^{\frac{\alpha\eta F}{RT}} \tag{16}$$

Since the leakage current strongly relies on the overpotential of the reaction, any catalytic influence of the system must be considered.

This model can be further advanced by introducing a potential-dependent capacitance ($C_\varnothing$) which arises due to the partially reversible Faradaic reaction on carbon surfaces in addition to the electrical double-layer capacitance. For instance, Faradaic adsorption of hydrogen on the electrode surface leads to a potential-dependent additional charge storage capacity on the electrode [161]. In this case, $C_\varnothing$ is defined by the areal fractional coverage θ by the Faradaically adsorbed species via Eq. (17):

$$C_\varnothing = q_1\left(\frac{d\theta}{dV}\right) \tag{17}$$

where q_1 is the charge for the formation or desorption of a monolayer of the intermediate (e.g., adsorbed H). In contrast to what is shown in Eq. (15), more than one slope can arise in the case of Faradaically adsorbed species described in Eq. (17); that is, one slope for small θ and another slope for $\theta > 1$ [88]. This theoretical consideration is expected to play a critical role in REHES systems with

reversible hydrogen reaction [81–83]. Not only the solvent decomposition reaction (e.g., H_2 or O_2 gas evolution), but the decomposition of highly concentrated redox ions must also be considered. One such example is a ferricyanide-containing acidic solution, where hydrogen cyanide gas evolution may occur (with all related issues regarding device safety) [125].

The main difference between type-(iii) and type-(ii) cases is that the activation-controlled self-discharge arises from the Faradaic reaction via the overcharge beyond the specific activation potential. By comparison, diffusion-controlled self-discharge occurs through the Faradaic reaction within the operating potential window at the electrode/electrolyte interface where the reactants should diffuse to the interface. For instance, in the presence of Fe-ion impurities, the leakage current arises due to the redox shuttling of a Fe^{2+}/Fe^{3+} couple which attributes to its characteristic diffusion-controlled features [162]. The diffusion of the redox shuttling process in accord with Fick's law and the semi-infinite diffusion of the planar electrodes, allow the time-dependent potential of the system to be derived; see Eq. (18):

$$V_t = V_i - \frac{2nFA\sqrt{D}\,c_0}{C\sqrt{\pi}}\sqrt{t} \tag{18}$$

where D and c_0 are the diffusion coefficient in cm^2/s and the initial molar concentration of the impurity redox reaction in mol/cm^3, respectively, and A is the area of the planar electrode in cm^2.

The diffusion-controlled leakage current is defined by Eq. (19):

$$i_s = nFD\left(\frac{dc_R}{dl}\right) \tag{19}$$

where c_R is the molar concentration of the diffusible redox species in mol/cm^3 and l is the distance from the electrode surface to the electrolyte in cm. As distinguished from the activation-controlled leakage current given by Eq. (16), Eq. (19) shows how the diffusion coefficient and the concentration of redox species influence the leakage current of the system. For semi-infinite diffusion near flat capacitor electrodes, the time-dependent leakage current is defined by Eq. (20):

$$i_s = nFA\sqrt{\frac{D}{\pi t}}\,c_0 \tag{20}$$

In this equation, the linear relationship between the concentration of the redox species and the leakage current can be seen clearly.

The cell voltage decay with time is not necessarily due to the leakage current. The non-uniform charge distribution, or type-(iv), mechanism, can also cause a potential decay in the cell as the potential drops through charge redistribution [110,161]. For that reason the term "self-discharge" may be improper to describe the phenomena associated with potential decay by charge redistribution [162,163]. The non-uniform charge distribution occurs either through double-layer formation in porous carbons [110,163–166] or conversion type Faradaic electrodes [110,155,161]. As originally suggested by De Levie, the equivalent circuit of a porous electrode should be established by considering the series of resistance and capacitive components along the pore [165]. According to the De Levie model, also known as the *RC* ladder circuit or transmission line model, electrochemical interactions for double-layer formation are higher at the pore entrance and lower with increasing pore depth. The extent of the electrical double-layer response, or penetration depth, is a square root function of angular frequency. At high frequency, the electrode behaves just like a flat electrode with its geometric surface area [165]. De Levie also found that the impedance phase angle of the porous electrode can be 45°, similar to that observed with Warburg diffusion. This, however, should not mean that it has the same origin or underpinning mechanism as the latter. When the electrode is rapidly charged, the electrical double-layer will be formed more at the entrance of the pores and the potential of the cell drops at resting condition due to the charge redistribution in the pores (Fig. 13C).

The charge redistribution can also be caused by Faradaic reactions of the electrode material, for instance, RuO_2. Conway et al. reported that the oxidation state of a RuO_2 electrode is non-uniform during the charging process and when the electrode is resting, the oxidation state of the electrode redistributes to reach the uniform state in the bulk electrode [155]. As a result of this redistribution process, the potential decays during the resting period after the charging process.

As discussed initially by Conway et al. and Black et al., [110,156] the potential profile owing to charge redistribution follows a linear relation with respect to $\log(t)$. Later, Kowal et al. reported that the potential decay of commercially available supercapacitors is fit better by two exponential terms with two time constants [163]. However, adopting a suitable mathematical representation of the voltage decay for the charge redistribution is challenging due to the possible concurrence of several self-discharge mechanisms in the system. The process of charge redistribution can be identified from its strong dependency on the applied current and the voltage holding time (Fig. 14A); in contrast, other self-discharge mechanisms do not show this dependency [156]. Additionally, the charge redistribution mechanisms may be identified by assessing the potential recovery after discharge of the cell (Fig. 14B). These intrinsic features of charge redistribution are critical for the investigation of a system containing more than one potential decay mechanism. For example, a sufficiently extended voltage holding time can exclude the contribution of charge redistribution.

For REHES systems, a similar potential decay can be observed as the charge redistribution occurs not at the electrode/electrolyte interface but mainly in the bulk electrolyte solution. As our work demonstrated for potassium ferricyanide (1.2 M) in a symmetric AC|AC cell configuration [39], a rapid cell voltage drop occurs over a period of hours (Fig. 14C). This voltage drop does not originate from redox shuttling since the diffusion of ferricyanide from the negative electrode to the positive electrode is effectively hindered by a cation exchange membrane. The substantial reduction in voltage arises from the incomplete oxidation of ferrocyanide due to the diffusion limit from the bulk electrolyte to the electrode during charging. After charging, the oxidized ferricyanide ions diffuse away from the electrode into the bulk electrolyte reservoir (Fig. 14C, *schematic illustration*). Thereby, the state-of-charge in the electrolyte is redistributed, and the cell voltage decays, particularly, for short charging periods (Fig. 14D).

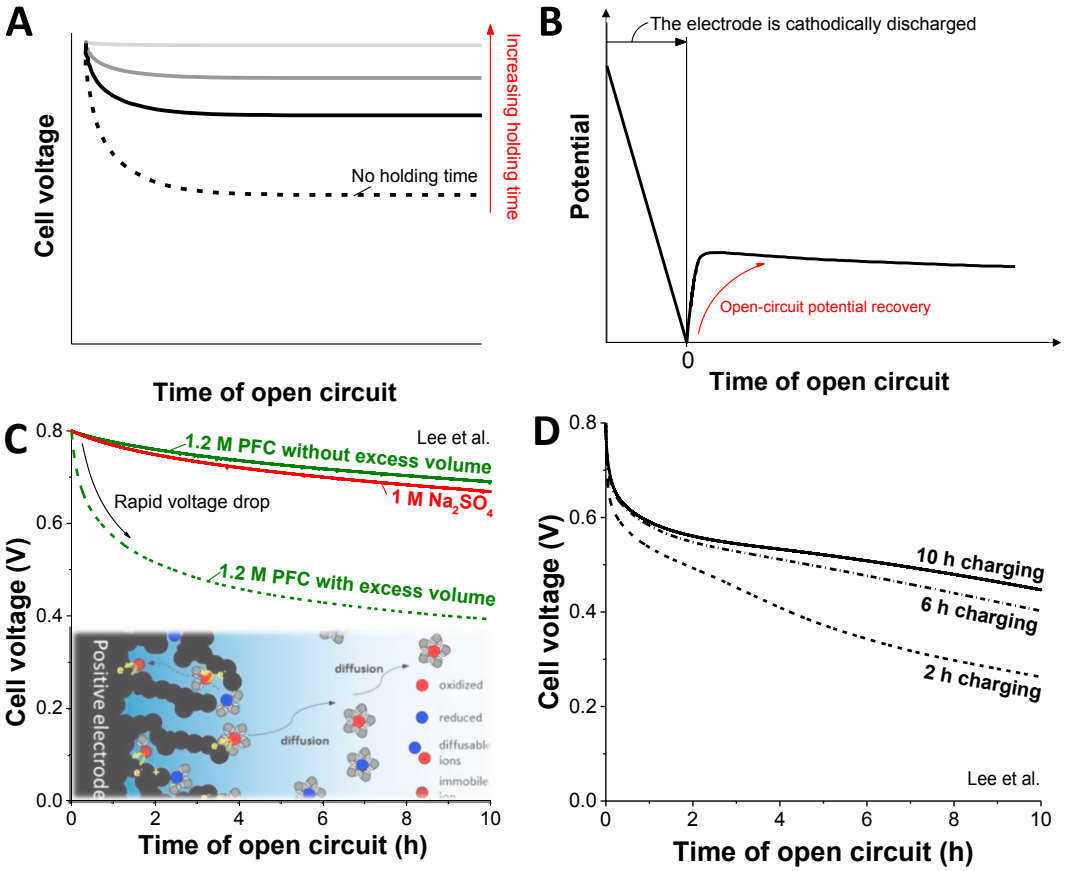

Fig. 14. Open-circuit potential during charge redistribution. (A) The charge redistribution is strongly dependent on the charging history. (B) Slow potential recovery after discharging the system results from charge redistribution. The diffusion-limited charge redistribution throughout the redox electrolyte in REHES systems (C) which depends on the charging time (D). Adapted with the permission from Ref. [39]. Copyright (2017) American Chemical Society.

To minimize the effect of the diffusion-limited charge redistribution, the cell can be charged either by potential holding for a longer time or using a lower current. Both options may not be practical for actual applications because they require a longer charging time for a device. Since the level of redistribution decreases when the size of the bulk electrolyte volume is reduced (Fig. 14C), confinement of the electrolyte to the narrow carbon pores only can be a practical solution. Otherwise, adsorption of redox ions can be considered as an alternative. If the porous carbon can be treated as a flat electrode, a simple mathematical model can be applied to describe this potential decay phenomenon by combining the Nernst and Fick's diffusion equations. A more appropriate model should be developed to reflect the porous nature of the electrode for an adequate description of the process.

The models introduced for the self-discharge and potential decay behavior have mostly been developed for supercapacitors [109,156,160]. Since many REHES systems do not behave like a capacitor in a strict sense, Eq. (13), Eq. (15), and Eq. (18) are not preferred because they assume constant capacitance. Theoretical calculations for the electrochemical and diffusion behavior of the redox species in porous electrodes are complex [160]. Therefore, the interpretation of self-discharge and potential decay of REHES systems should be approached carefully when using conventional models. Nonetheless, these models are of great help, particularly when combined with other analytical tools.

When a REHES system suffers from redox shuttling, the leakage current starts to dominate as soon as the redox potential is reached at the electrode (Fig. 11A). Hence, the potential profile for highly concentrated REHES systems at low current density looks like that of activation-controlled self-discharge (Fig. 13B) despite its diffusion-controlled nature. Therefore, complementary analyses are necessary for an adequate interpretation of self-discharge mechanisms investigated over the range of cell voltages at which the redox reaction occurs. Our previous work examined the redox shuttling behavior by comparing the potential profile during the resting condition with other electrochemical analyses such as EIS and CV techniques [39]. When a system suffers from severe self-discharge caused by redox shuttling, a distorted cyclic voltammogram is obtained (Fig. 15A, AC|AC with potassium ferricyanide, PFC). In contrast, when the redox shuttling is suppressed, a cell with a CEM exhibits a rectangular current response outside of the redox potential window of PFC (e.g., 0.5–0.8 V). In this case, the sign of the current changes from positive to negative when the direction of the cell polarization changes from positive to negative. This indicates that the current is consumed during charging and restored during subsequent discharge. In contrast, a cell without CEM shows no change in the sign of the current even though the scan

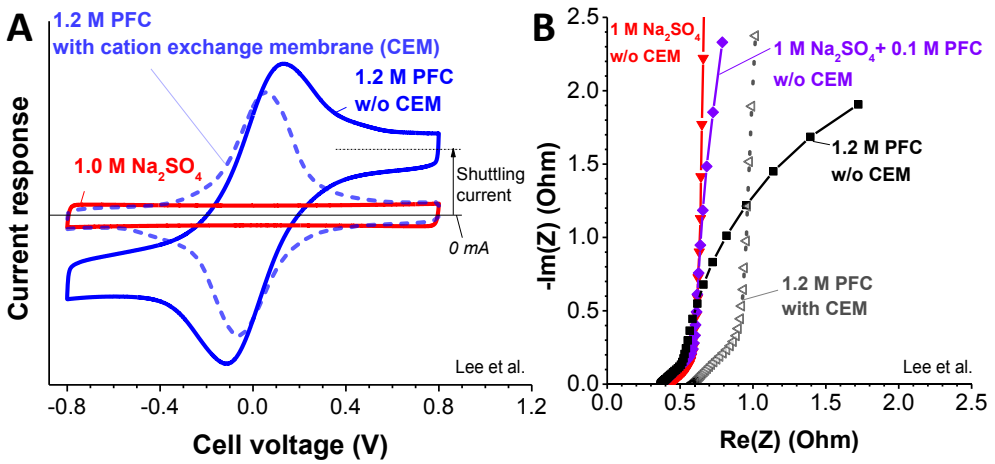

Fig. 15. Characterization of the self-discharge rate by redox shuttling in REHES systems. The cyclic voltammogram (A) and Nyquist plot (B) indicate significant redox shuttling. Adapted with permission from Ref. [39] Copyright (2017) American Chemical Society.

direction is reversed because of high self-discharge current. Therefore, the level of offset current (Fig. 15A) can be assigned to redox shuttling.

The redox shuttling can also be identified with EIS in a Nyquist plot (Fig. 15B, measured at 0 V with a potential amplitude of 5 mV). In general, EDLCs exhibit a regime with a slope close to 90° which originates from the capacitive component in the system: for example, a symmetric AC|AC cell in 1 M Na_2SO_4 (Fig. 15B). In the case of a low concentration PFC solution (1 M Na_2SO_4 + 0.1 M PFC), the curve in the plot deviated from a straight line (with a slope close to 90°). At high concentration (1.2 M PFC), the cell without CEM exhibited a much clearer non-linearity in the plotted data. In contrast, the same cell with CEM showed no sign of deviations from linear behavior. Since the presence of CEM significantly suppresses the redox shuttling, the bending of the curve in the low-frequency regime (where 90° slope appears for EDLCs) can indicate redox shuttling. The possible origin of the bending can be the resistive component of a chemical short-circuit through redox shuttling because the curve bends toward the phase angle of resistive impedance (0°).

5.3.2. Redox kinetics and mass transport for redox electrolyte systems

As reported in previous work [39,43], REHES systems provide not only enhanced energy storage capacity, but may also excel in power handling. For an understanding of the enhanced power performance, the thin-layer electrochemistry model provides an excellent theoretical basis. The development of the theories for TLE was initiated by Anson [150] and Hubbard [149] in the 1960 s in support of their experimental work with a confined thin-layer electrolyte (40–140 μm) on a flat electrode. In general case of cyclic voltammetry, the redox peak current, i_p, is governed by the Randles-Ševčík equations; Eq. (21) for reversible processes and Eq. (22) for irreversible processes [167–169]:

$$I_{p,rev} = \pm 0.446 nFAc\sqrt{\left(\frac{nFD\upsilon}{RT}\right)} \tag{21}$$

$$I_{p,irr} = \pm 0.496 nFAc\sqrt{\left(\frac{\alpha n_0 FD\upsilon}{RT}\right)} \tag{22}$$

In these equations, the plus and minus symbols indicate anodic and cathodic currents, respectively, A is the geometric area of the electrode in cm^2, c is the concentration in mol/cm^3, ν is the scan rate in V/s, and n_0 is the number of electrons transferred before the rate determining step. The Randles-Ševčík theory is based on the assumption that the electrochemical reaction is not only controlled by the charge transfer kinetics near the electrode surface (ca. 1 nm), but also by the mass transport in the diffusion layer. Fig. 16A depicts a schematic representation of molecular arrangements at the interface between the electrode and electrolyte which consists of (i) a compact layer with Inner Helmholtz layer (IHP) and outer Helmholtz layer (OHP), (ii) Gouy-Chapman diffuse layer, and (iii) diffusion layer [167]. According to the model by Hubbard and Hubbard & Anson [148,149], the redox peak current for reversible ($I_{p,rev}$) and irreversible processes ($I_{p,irr}$) can be described by Eq. (23) and Eq. (24) when the diffusion layer thickness is reduced (40 μm).

$$I_{p,rev} = \pm 0.250 nFU_t c\left(\frac{nF\upsilon}{RT}\right) \tag{23}$$

$$I_{p,irr} = \pm 0.368 nFU_t c\left(\frac{\alpha n_0 F\upsilon}{RT}\right) \tag{24}$$

where U_t is the volume of the thin layer in cm^3.

It is important to note that the peak current is not a function of the square root of the scan rate, $\sqrt{\upsilon}$, but a linear function of υ. This has often been observed in recent studies for the high power performing redox enhanced energy storage systems [39,170]. Since the

TLE theories were established, further developments have been made by Compton's group with numerical simulations [151,152,154]. Their simulation works indicate that the electrochemical analysis regarding the charge transfer kinetics should be carried out carefully with cyclic voltammetry. As presented in Fig. 16B, the peak-to-peak separation, $\Delta\varphi_p$, was simulated by semi-infinite diffusion and thin-layer diffusion models with the same value of the heterogeneous rate constant. The results imply that the smaller $\Delta\varphi_p$ value for the electrode modified with the carbon nanotube (CNT) array should not be interpreted as due to electrocatalysis by enhanced electron transfer kinetics. Instead, it is an intrinsic feature of TLE formed in the confined space of the electrode. The TLE simulation has been further extended for cylinder arrays [152] and cylindrical pores [154].

Most of the theoretical works have been developed to investigate fundamental aspects of the relevant processes under study. Recent studies by Narayanan et al. [42] extended the TLE theory to energy storage aspects for vertically aligned carbon nanotubes (Fig. 16C, *inset*) with a spacing between nanotubes of around 350 nm (i.e., macropores). They concluded that the enhanced electrochemical reaction is based on the relative absence of diffusion as the electrolyte is confined to thin layers on the carbon nanotubes. The uniqueness of their work is that the individual redox charge storage capacity by a thin layer (or thin-layer capacity) and by a diffusion contribution was determined experimentally. They assumed that the redox charge storage capacity through diffusion disappears and the thin-layer capacity predominates at high galvanostatic currents (Fig. 16C). The redox kinetics in carbon micropores were further investigated by our team with potassium ferricyanide [43] by comparing the reduction peak currents in cyclic voltammograms. We also observed thin-layer behavior for microporous carbon, while diffusion-controlled redox kinetics was found for the flat glassy carbon electrode [43]. Our work implies that the electrochemical analysis by peak current versus scan rate for microporous carbons should be carried out carefully since the contribution of double-layer current is not negligible. The peak current is the contribution of (i) double-layer formation, i_{EDL}, (ii) diffusion-limited redox current, i_{Diff}, and (iii) redox current under TLE condition, i_{TLE}., as shown in Eq. (25):

$$i_p = i_{EDL} + i_{Diff} + i_{TLE} \tag{25}$$

For significant electrical double-layer currents, plots of the peak current against the scan rate may lead to an incorrect data interpretation. Hence, the electrical double-layer current should be quantified and subtracted, or limited by modifying, if possible, the experimental conditions. An alternative is to perform a kinetic analysis based on the results obtained with rotating disk electrode at a fixed scan rate where the diffusion condition is varied by rotating the electrode at different speeds. The electrical double-layer

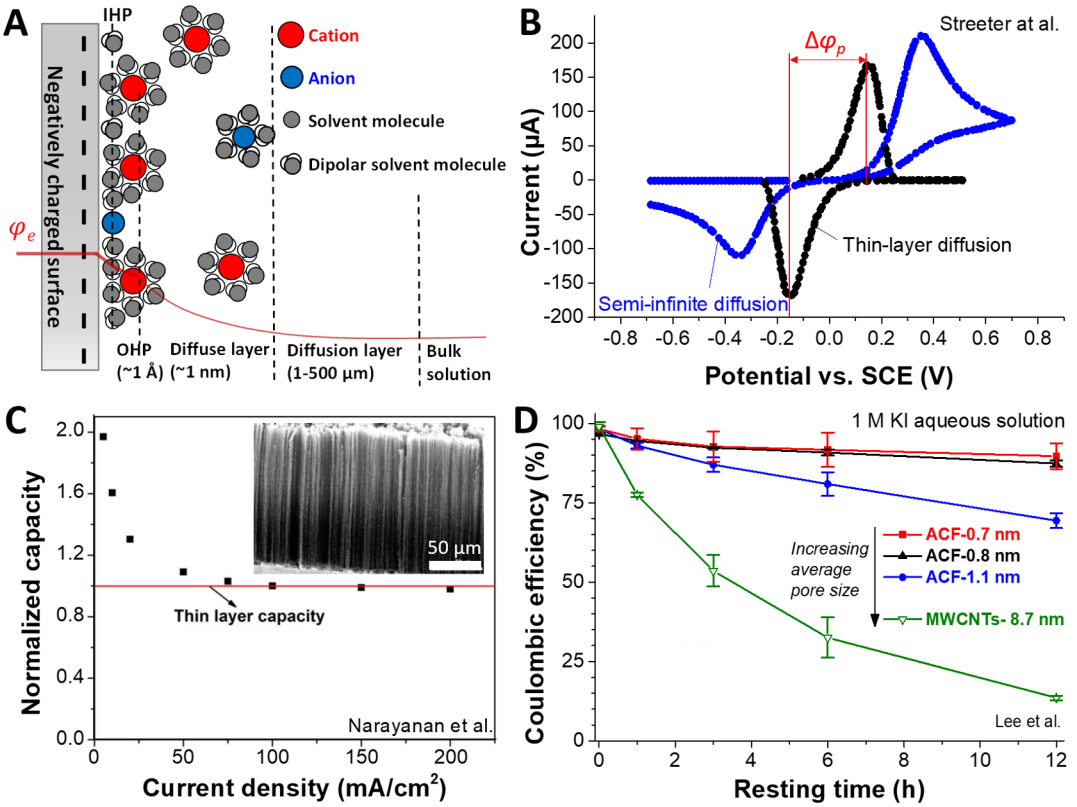

Fig. 16. (A) Schematic illustration of the molecular arrangements and the diffusion in the case of a flat electrode. (B) Simulation work based on the model with the thin-layer electrochemistry from Ref. [151], (C) Identification of the thin-layer capacity with vertically aligned carbon nanotubes. Inset shows the scanning electron micrograph of the vertically aligned carbon nanotubes. Republished with permission of Electrochemical Society, from Ref. [42], Copyright (2017); permission conveyed through Copyright Clearance Center, Inc. (D) The self-discharge rate is different in case of redox ion adsorption which depends on the carbon pore size. Adapted from Ref. [43] with permission from The Royal Society of Chemistry.

contribution will be constant at fixed scan rate while kinetics of the redox species can be studied at various rotation speeds [43].

However, there are further aspects that need to be considered. As reported by Chathoth et al., [171] the diffusion coefficients of ILs are higher in confined carbon mesopores than in a bulk liquid. On the contrary, lower diffusion coefficients in porous carbon for bi-redox ILs were suggested by Mourad et al. [146]. Whether the diffusion of the ions is faster or slower in the confined carbon pores, we see that the diffusion coefficients might not be constant for the pores with different shapes, sizes, and functional groups. Yet, current TLE theories and models typically assume constant diffusion coefficients. Another difficulty is to distinguish the thin-layer diffusion from the adsorption effects since the electrochemical reaction with adsorbed species shows a similar mass transport feature to the TLE condition [152]. For instance, the peak current of a reversible process can be described by introducing a surface covered with adsorbed species by use of Eq. (26) [167]:

$$I_{p,ads} = \pm 0.250 nF\Gamma A\left(\frac{nF\upsilon}{RT}\right) \tag{26}$$

where Γ is the fractional surface coverage. The similarity between Eq. (23) and Eq. (26) can be seen; particularly, because the peak current is a linear function of υ.

As demonstrated by our work (Fig. 16D, ACF in 1 M KI aqueous solution) [43], the iodide diffusion and adsorption behavior is closely related to the size of the carbon pores. We found that iodide shows stronger adsorption in smaller pores and weaker adsorption in larger pores, leading to faster diffusion. The latter causes higher self-discharge rates by redox shuttling. Furthermore, the concentration of the ions in the carbon pores is expected to be different as the diffusion layers can overlap [172]. This aspect is not reflected in recent theoretical or simulation works. New theories and simulations are necessary to account for the influence of pore size and functional groups on the adsorption energy, diffusion coefficients, and local concentrations. This understanding of the redox kinetics and ion diffusion processes in porous carbon electrodes can be advanced and further performance improvement of the REHES systems attained.

5.3.3. Influence of pore structure and functional groups

The pore structure of carbon electrode materials may influence the diffusion, adsorption, and electrochemical kinetics of the redox ions in the REHES systems. If large volume reservoirs are provided for redox electrolytes, carbon electrode materials with high pore volumes are expected to be beneficial for the REHES system. Yu et al. reported such an enhanced charge with a porous diamond electrode in an aqueous Na_2SO_4 solution containing potassium ferrocyanide and ferricyanide [126]. Gorska et al. observed that a porous carbon electrode with a high portion of mesopores provided greater charge storage enhancement in thiocyanate-containing aqueous solution than it did in microporous carbon [119]. Lota et al. and Krüner et al. also reported that AC with higher SSA exhibits higher capacity enhancement in aqueous KI solution [44,61]. However, the introduction of a large reservoir space for the redox electrolyte may have a negative influence due to the diffusion-limited charge redistribution of the electrolyte (Fig. 14C and D) [39]. For the prevention of this effect, the volume of the electrolyte should be confined to narrow carbon pores. In addition, the confinement of the halides in the carbon micropores is the key to cost-effective energy storage applications [11,43].

As demonstrated by our work (Fig. 16D) [43], narrow micropores (< 1 nm) with high total pore volume seem to be ideal for the effective charge storage enhancement with iodide-containing aqueous redox electrolytes. The narrow pores were found to be essential for low self-discharge rates, and the charge storage capacity was enhanced by the high pore volume of the activated carbon fiber electrodes. A hierarchical structure with micro-, meso-, and macropores may be advantageous for effective diffusion of redox ions. However, an optimum must be found because mesopores and macropores possibly exert a negative influence through diffusion-limited charge redistribution of the electrolyte.

The presence of functional groups on carbon electrode materials also influences diffusion, adsorption, and electrochemical kinetics of the redox ions in the REHES systems. Because electrosorption of the cation redox species is not favored at the positive electrode, the introduction of electronegative functional groups can provide cation affinity at the surface of the positive carbon electrode [25]. For instance, Mai et al. reported a synergistic interaction between the $CuCl_2$ aqueous solution and a functionalized carbon surface with oxygen groups [80]. Accordingly, a large capacity enhancement with high cyclic stability was achieved as chloride stabilizes the interaction between the copper and the oxygen surface groups. Frackowiak at al. proposed that VO^{2+} and $VO_2{}^+$ ions can be transported to the interface between the electrolyte and positive porous carbon electrode with the aid of oxygenated functional groups [46]. In addition to the charge transfer aspects of the interactions, the binding of the vanadyl ion to the oxygenated carbon functional group has an interesting impact on ion diffusion. If the ions can be immobilized on the electrode surface, redox shuttling might be reduced without the need for ISMs. In this case, the $VO_2{}^+$ reaction should be prevented as this compound is expected to diffuse back to the solution during oxidation (charging in a full-cell at the positive electrode).

Gao et al. reported catalytic activities of nitrogen-doped carbon electrodes which led to a positive influence on the energy storage performance in a pyrocatechol-containing aqueous redox electrolyte [173]. This work also suggested that the origin of the catalytic activities is pyridinic nitrogen. When carbon is modified with functional groups, the catalytic effects should be considered not only for the redox kinetics of the redox electrolytes, but also for the decomposition of the electrolytes. As discussed in Section 3.1, doping with heteroatoms may cause catalytic effects on both the OER and the HER which indeed reduce the stable potential window of the system.

6. Conclusions

From the performance point of view, non-flow redox electrolyte-aided hybrid energy storage (REHES) systems can provide not only high specific power (up to 20.0 kW/kg, normalized by m_a) but also high specific energy (up to 250 Wh/kg, normalized by m_a)

and robust cyclic stability (over 5000 cycles), particularly with porous carbon electrodes. Even when the performance is normalized by the mass of the electrode, electrolyte, and the separator, a specific energy of up to 50 Wh/kg and specific power up to 5 kW/kg can be achieved. This breaks with the paradigm that power must always be traded for energy storage capacity, and vice versa. The REHES systems can provide power performance as high as commercial supercapacitors (charging on a scale of minutes) while exhibiting specific energy as high as that of nickel-cadmium and nickel-zinc batteries. The high power performance is a unique feature of REHES systems, enabled by thin-layer electrochemistry, particularly through the confined redox electrolytes in carbon micropores. For redox flow batteries, the latter is not beneficial for effective circulation of redox electrolytes.

All results indicate that REHES systems are very promising for the new generation of electric energy storage devices not only because of high device performance but also because of system simplicity. The redox electrolytes can be applied readily to other EES materials and devices. Particularly, REHES systems with porous carbon electrodes are cost-effective relative to other expensive battery materials like nickel, cadmium, and other cathode materials for lithium-ion batteries.

For performance characterizations, many of the reported systems in the literature have issues with the calculation of specific energy and power. Therefore, the performance was mostly overestimated in these reports. First, a common misunderstanding is to assume the tested device works as a capacitor, and then proceed to evaluate the performance with inappropriate equations. Second, the influence of the excess electrolyte in the cell was often ignored despite its possible contribution to additional capacity through diffusion. Any volume of excess electrolyte should be avoided to prevent an overestimation of the performance and the diffusion-limited charge redistribution. Third, the potential window was often not applied carefully, and with no consideration of the solute decomposition or electrode catalytic effects (functionalized carbon or metal oxides) on the solvent decomposition. The decomposition reaction is particularly important when the products are toxic or corrosive. For the determination of the decomposition reaction with porous carbon electrodes, advanced analytical techniques such as the *S*-value test and in-operando gas analysis can be useful.

Redox shuttling is a major issue with REHES systems; however, the self-discharge rate is often not reported. For further developments of the REHES systems, it is necessary also to quantify the self-discharge rates and to identify the transport and kinetic mechanisms by conventional and advanced analytical techniques. To reduce redox shuttling, adsorption of redox ions at the electrode is a promising solution that enables independence from cost-expensive ion selective membranes.

For high performance REHES systems, porous carbon electrodes play essential roles regarding redox kinetics, diffusion, and adsorption. Porous carbon electrodes not only provide sufficient space for redox electrolytes but also enable fast redox reactions through diffusion-less redox kinetics in confined carbon pores. Furthermore, strong adsorption of halides on nanoporous carbon electrodes is attractive to achieve low levels of redox shuttling in the absence of ion selective membranes. Adsorption of halides on polymer-based electrodes is reported; however, these materials are less attractive than nanoporous carbon due to higher production cost and lower electric conductivity.

In contrast to the aqueous redox electrolyte systems, non-aqueous redox electrolyte systems remain ill-explored. They offer the key benefit of enabling a high operating cell voltage (1.2–4 V), while their general drawback is lower power performance in comparison to the aqueous systems due to low ionic conductivity. In the future, non-aqueous REHES systems with improved ion mobility may play an important role as a bridge between aqueous REHES systems for power management and battery systems for energy management.

Acknowledgments

S.P. acknowledges financial support of the German Academic Exchange Service DAAD (award numbers 91579066) within the frame of the GSSP-Program and DocMASE. This work was part of the Carbon Metal Oxide Nanohybrid project (CarMON) supported by the Leibniz Association (SAW-2017). The authors also thank Eduard Arzt (INM) for his kind and continuing support.

References* = citations authored by authors of this paper

[1] Pomerantseva E, Gogotsi Y. Two-dimensional heterostructures for energy storage. Nat Energy 2017;2:17089.
[2] Miller JR, Burke AF. Electrochemical capacitors: challenges and opportunities for real-world applications. Electrochem Soc Interface 2008;17:53.
[3] Miller JR, Simon P. Electrochemical capacitors for energy management. Science 2008;321:651–2.
[4] Lukatskaya MR, Dunn B, Gogotsi Y. Multidimensional materials and device architectures for future hybrid energy storage. Nat Commun 2016;7:12647.
[5] Linden D, Reddy TB. Handbook of batteries. McGraw-Hill Education; 2001.
[6] Krause LJ, Brandt T, Chevrier VL, Jensen LD. Surface area increase of silicon alloys in Li-ion full cells measured by isothermal heat flow calorimetry. J Electrochem Soc 2017;164:A2277–82.
[7] Krause LJ, Jensen LD, Chevrier VL. Measurement of Li-ion battery electrolyte stability by electrochemical calorimetry. J Electrochem Soc 2017;164:A889–96.
[8] Simon P, Gogotsi Y. Materials for electrochemical capacitors. Nat Mater 2008;7:845–54.
[9] Chen GZ. Supercapacitor and supercapattery as emerging electrochemical energy stores. Int Mater Rev 2017;62:173–202.
[10] Mukhopadhyay A, Sheldon BW. Deformation and stress in electrode materials for Li-ion batteries. Prog Mater Sci 2014;63:58–116.
[11] Evanko B, Boettcher SW, Yoo SJ, Stucky GD. Redox-enhanced electrochemical capacitors: status, opportunity, and best practices for performance evaluation. ACS Energy Lett 2017;2:2581–90.
[12] Xia L, Yu LP, Hu D, Chen GZ. Electrolytes for electrochemical energy storage. Mater Chem Front 2017;1:584–618.
[13] *Lee J, Krüner B, Tolosa A, Sathyamoorthi S, Kim D, Choudhury S, et al. Tin/vanadium redox electrolyte for battery-like energy storage capacity combined with supercapacitor-like power handling. Energy Environ Sci 2016;9:3392–8.
[14] Augustyn V, Simon P, Dunn B. Pseudocapacitive oxide materials for high-rate electrochemical energy storage. Energy Environ Sci 2014;7:1597–614.
[15] Herrero E, Buller LJ, Abruña HD. Underpotential deposition at single crystal surfaces of Au, Pt, Ag and other materials. Chem Rev 2001;101:1897–930.
[16] Yoshida N, Yamada Y, Nishimura S-i, Oba Y, Ohnuma M, Yamada A. Unveiling the origin of unusual pseudocapacitance of $RuO_2{\cdot}nH_2O$ from its hierarchical nanostructure by small-angle X-ray scattering. J Phys Chem C 2013;117:12003–9.
[17] Sugimoto W. Ruthenium oxides as supercapacitor electrodes. Encyclopedia of applied electrochemistry. Springer; 2014. p. 1813–21.
[18] Brousse T, Bélanger D, Long JW. To be or not to be pseudocapacitive? J Electrochem Soc 2015;162:A5185–9.

[19] Simon P, Gogotsi Y, Dunn B. Where do batteries end and supercapacitors begin? Science 2014;343:1210–1.
[20] Wang W, Luo Q, Li B, Wei X, Li L, Yang Z. Recent progress in redox flow battery research and development. Adv Funct Mater 2013;23:970–86.
[21] Li L, Kim S, Wang W, Vijayakumar M, Nie Z, Chen B, et al. A stable vanadium redox-flow battery with high energy density for large-scale energy storage. Adv Energy Mater 2011;1:394–400.
[22] Weber AZ, Mench MM, Meyers JP, Ross PN, Gostick JT, Liu Q. Redox flow batteries: a review. J Appl Electrochem 2011;41:1137–64.
[23] Li B, Nie Z, Vijayakumar M, Li G, Liu J, Sprenkle V, et al. Ambipolar zinc-polyiodide electrolyte for a high-energy density aqueous redox flow battery. Nat Commun 2015;6:6303.
[24] Alotto P, Guarnieri M, Moro F. Redox flow batteries for the storage of renewable energy: a review. Renew Sustain Energy Rev 2014;29:325–35.
[25] Akinwolemiwa B, Peng C, Chen GZ. Redox electrolytes in supercapacitors. J Electrochem Soc 2015;162:A5054–9.
[26] *Béguin F, Presser V, Balducci A, Frackowiak E. Carbons and electrolytes for advanced supercapacitors. Adv Mater 2014;26:2219–51.
[27] Bandaru PR, Yamada H, Narayanan R, Hoefer M. Charge transfer and storage in nanostructures. Mater Sci Eng R-Rep 2015;96:1–69.
[28] Yue Y, Liang H. Micro- and nano-structured vanadium pentoxide (V_2O_5) for electrodes of lithium-ion batteries. Adv Energy Mater 2017;7:1602545.
[29] Aravindan V, Gnanaraj J, Lee Y-S, Madhavi S. Insertion-type electrodes for nonaqueous Li-ion capacitors. Chem Rev 2014;114:11619–35.
[30] *Widmaier M, Jäckel N, Zeiger M, Abuzarli M, Engel C, Bommer L, et al. Influence of carbon distribution on the electrochemical performance and stability of lithium titanate based energy storage devices. Electrochim Acta 2017;247:1006–18.
[31] *Widmaier M, Krüner B, Jäckel N, Aslan M, Fleischmann S, Engel C, et al. Carbon as quasi-reference electrode in unconventional lithium-salt containing electrolytes for hybrid battery/supercapacitor devices. J Electrochem Soc 2016;163:A2956–64.
[32] *Porada S, Lee J, Weingarth D, Presser V. Continuous operation of an electrochemical flow capacitor. Electrochem Commun 2014;48:178–81.
[33] *Presser V, Dennison CR, Campos J, Knehr KW, Kumbur EC, Gogotsi Y. The electrochemical flow capacitor: a new concept for rapid energy storage and recovery. Adv Energy Mater 2012;2:895–902.
[34] Hatzell KB, Beidaghi M, Campos JW, Dennison CR, Kumbur EC, Gogotsi Y. A high performance pseudocapacitive suspension electrode for the electrochemical flow capacitor. Electrochim Acta 2013;111:888–97.
[35] *Lee J, Weingarth D, Grobelsek I, Presser V. Use of surfactants for continuous operation of aqueous electrochemical flow capacitors. Energy Technol 2016;4:75–84.
[36] Nguyen T, Montemor MF. Redox active materials for metal compound based hybrid electrochemical energy storage: a perspective view. Appl Surf Sci 2017;422:492–7.
[37] Senthilkumar ST, Selvan RK, Melo JS. Redox additive/active electrolytes: a novel approach to enhance the performance of supercapacitors. J Mater Chem A 2013;1:12386–94.
[38] Frackowiak E, Meller M, Menzel J, Gastol D, Fic K. Redox-active electrolyte for supercapacitor application. Faraday Discuss 2014;172:179–98.
[39] *Lee J, Choudhury S, Weingarth D, Kim D, Presser V. High performance hybrid energy storage with potassium ferricyanide redox electrolyte. ACS Appl Mater Interfaces 2016;8:23676–87.
[40] Cericola D, Kötz R. Hybridization of rechargeable batteries and electrochemical capacitors: principles and limits. Electrochim Acta 2012;72:1–17.
[41] Cericola D, Novák P, Wokaun A, Kötz R. Hybridization of electrochemical capacitors and rechargeable batteries: an experimental analysis of the different possible approaches utilizing activated carbon, $Li_4Ti_5O_{12}$ and $LiMn_2O_4$. J Power Sources 2011;196:10305–13.
[42] Narayanan R, Bandaru PR. High rate capacity through redox electrolytes confined in macroporous electrodes. J Electrochem Soc 2014;162:A86–91.
[43] *Lee J, Srimuk P, Fleischmann S, Ridder A, Zeiger M, Presser V. Nanoconfinement of redox reactions enables rapid zinc iodide energy storage with high efficiency. J Mater Chem A 2017;5:12520–7.
[44] *Krüner B, Lee J, Jäckel N, Tolosa A, Presser V. Sub-micrometer novolac-derived carbon beads for high performance supercapacitors and redox electrolyte energy storage. ACS Appl Mater Interfaces 2016;8:9104–15.
[45] *Lee J, Tolosa A, Krüner B, Jäckel N, Fleischmann S, Zeiger M, et al. Asymmetric tin–vanadium redox electrolyte for hybrid energy storage with nanoporous carbon electrodes. Sustainable Energy Fuels 2017;1:299–307.
[46] Frackowiak E, Fic K, Meller M, Lota G. Electrochemistry serving people and nature: high-energy ecocapacitors based on redox-active electrolytes. ChemSusChem 2012;5:1181–5.
[47] Yamamoto T. Use of polymer-iodine adducts as positive electrodes of cells. J Chem Soc-Chem Commun 1981:187–8.
[48] Yamamoto T, Kuroda S-I, Yamamoto A. Iodine cells: iodine adducts of 6-nylon as cathodes of galvanic cells. Inorg Chim Acta 1982;65:L175–6.
[49] Yamamoto T, Kuroda S-I. Iodine-polymer adducts as active materials for positive electrodes of galvanic cells. J Electroanal Chem Interfacial Electrochem 1983;158:1–11.
[50] Yamamoto T, Hishinuma M, Yamamoto A. Zn|ZnI_2|iodine secondary battery using iodine-nylon-6 adduct as positive electrode, and its charge-discharge performance. Inorg Chim Acta 1984;86:L47–9.
[51] Mengoli G, Musiani MM, Pletcher D, Valcher S. Studies of Zn|ZnX_2|polyaniline batteries. II. X = I. J Appl Electrochem 1987;17:525–31.
[52] Mengoli G, Musiani MM, Pletcher D, Valcher S. Studies of Zn| ZnX_2| polyaniline batteries. IX = Cl and Br. J Appl Electrochem 1987;17:515–24.
[53] Mengoli G, Musiani MM, Tomat R, Valcher S, Pletcher D. On the use of pyrrole black in zinc-halogen batteries. J Appl Electrochem 1985;15:697–704.
[54] Yamamoto T, Kanbara T. Porous and electrically conducting clay-carbon composite as positive electrodes of zinc-oxygen primary cells and zinc-iodine secondary cells. Inorg Chim Acta 1988;142:191–3.
[55] Hishinuma M, Iwahori T, Sugimoto H, Sukawa H, Tanaka T, Yamamoto T, et al. Zinc iodine secondary cell using 6-nylon or poly(ether) based electrode – basic research for industrial use of the secondary cell. Electrochim Acta 1990;35:255–61.
[56] Manassen J, Cabasso I. Nonflow zinc/halogen storage cell made of thin film composite. J Electrochem Soc 1989;136:578–9.
[57] Tsutsumi H, Matsuda Y. Electrochemical behavior of ferrocene-deoxycholic acid 1:2 inclusion compound and its application to positive material of zinc-iodine secondary batteries. Electrochim Acta 1993;38:1373–5.
[58] Wang G, Zhang L, Zhang J. A review of electrode materials for electrochemical supercapacitors. Chem Soc Rev 2012;41:797–828.
[59] Shown I, Ganguly A, Chen L-C, Chen K-H. Conducting polymer-based flexible supercapacitor. Energy Sci Eng 2015;3:2–26.
[60] Li Q, Li K, Sun C, Li Y. An investigation of Cu^{2+} and Fe^{2+} ions as active materials for electrochemical redox supercapacitors. J Electroanal Chem 2007;611:43–50.
[61] Lota G, Frackowiak E. Striking capacitance of carbon/iodide interface. Electrochem Commun 2009;11:87–90.
[62] Lota G, Fic K, Frackowiak E. Alkali metal iodide/carbon interface as a source of pseudocapacitance. Electrochem Commun 2011;13:38–41.
[63] Roldan S, Granda M, Menendez R, Santamaria R, Blanco C. Mechanisms of energy storage in carbon-based supercapacitors modified with a quinoid redox-active electrolyte. J Phys Chem C 2011;115:17606–11.
[64] Roldán S, Blanco C, Granda M, Menéndez R, Santamaría R. Towards a further generation of high-energy carbon-based capacitors by using redox-active electrolytes. Angew Chem Int Ed 2011;50:1699–701.
[65] Tian Y, Yan J, Xue R, Yi B. Capacitive properties of activated carbon in $K_4Fe(CN)_6$. J Electrochem Soc 2011;158:A818–21.
[66] Su LH, Zhang XG, Mi CH, Gao B, Liu Y. Improvement of the capacitive performances for Co-Al layered double hydroxide by adding hexacyanoferrate into the electrolyte. Phys Chem Chem Phys 2009;11:2195–202.
[67] Tachibana M, Tsukada Y, Ohishi T, Yamagishi H, Murakami M. New high capacity electric energy storage device with an electrolyte that contains a conducting polymer. Kobunshi Ronbunshu 2009;66:259–65.
[68] Sun G, Li K, Sun C. Electrochemical performance of electrochemical capacitors using Cu(II)-containing ionic liquid as the electrolyte. Microporous Mesoporous Mater 2010;128:56–61.
[69] Yoo SJ, Evanko B, Wang X, Romelczyk M, Taylor A, Ji X, et al. Fundamentally addressing bromine storage through reversible solid-state confinement in porous carbon electrodes: design of a high-performance dual-redox electrochemical capacitor. J Am Chem Soc 2017;139:9985–93.
[70] Evanko B, Yoo SJ, Chun S-E, Wang X, Ji X, Boettcher SW, et al. Efficient charge storage in dual-redox electrochemical capacitors through reversible counterion-

induced solid complexation. J Am Chem Soc 2016;138:9373–6.
[71] Chun SE, Evanko B, Wang X, Vonlanthen D, Ji X, Stucky GD, et al. Design of aqueous redox-enhanced electrochemical capacitors with high specific energies and slow self-discharge. Nat Commun 2015;6:7818.
[72] Ahmad Z. Principles of corrosion engineering and corrosion control. Principles of corrosion engineering and corrosion control. Elsevier Science; 2006. p. 49.
[73] Baranowski B, Zaginaichenko S, Schur D, Skorokhod V, Veziroglu A. Carbon nanomaterials in clean energy hydrogen systems. Netherlands: Springer; 2008. p. 283.
[74] Cheng Y, Jiang SP. Advances in electrocatalysts for oxygen evolution reaction of water electrolysis -from metal oxides to carbon nanotubes. Prog Nat Sci: Mater Int 2015;25:545–53.
[75] Miles M, Thomason M. Periodic variations of overvoltages for water electrolysis in acid solutions from cyclic voltammetric studies. J Electrochem Soc 1976;123:1459–61.
[76] Qu K, Zheng Y, Zhang X, Davey K, Dai S, Qiao SZ. Promotion of electrocatalytic hydrogen evolution reaction on nitrogen-doped carbon nanosheets with secondary heteroatoms. ACS Nano 2017;11:7293–300.
[77] Li Y, Wang H, Xie L, Liang Y, Hong G, Dai H. MoS_2 nanoparticles grown on graphene: an advanced catalyst for the hydrogen evolution reaction. J Am Chem Soc 2011;133:7296–9.
[78] Su X, Tan K-J, Elbert J, Ruttiger C, Gallei M, Jamison TF, et al. Asymmetric Faradaic systems for selective electrochemical separations. Energy Environ Sci 2017;10:1272–83.
[79] *Su X, Hatton TA. Electrosorption at functional interfaces: from molecular-level interactions to electrochemical cell design. Phys Chem Chem Phys 2017;19:23570–84.
[80] Mai LQ, Minhas-Khan A, Tian X, Hercule KM, Zhao YL, Lin X, et al. Synergistic interaction between redox-active electrolyte and binder-free functionalized carbon for ultrahigh supercapacitor performance. Nat Commun 2013;4:2923.
[81] Fic K, Meller M, Menzel J, Frackowiak E. Around the thermodynamic limitations of supercapacitors operating in aqueous electrolytes. Electrochim Acta 2016;206:496–503.
[82] He M, Fic K, Frąckowiak E, Novák P, Berg EJ. Influence of aqueous electrolyte concentration on parasitic reactions in high-voltage electrochemical capacitors. Energy Storage Mater 2016;5:111–5.
[83] Vix-Guterl C, Frackowiak E, Jurewicz K, Friebe M, Parmentier J, Béguin F. Electrochemical energy storage in ordered porous carbon materials. Carbon 2005;43:1293–302.
[84] Frackowiak E, Béguin F. Electrochemical storage of energy in carbon nanotubes and nanostructured carbons. Carbon 2002;40:1775–87.
[85] He ML, Fic K, Frackowiak E, Novak P, Berg EJ. Ageing phenomena in high-voltage aqueous supercapacitors investigated by in situ gas analysis. Energy Environ Sci 2016;9:623–33.
[86] Abbas Q, Béguin F. High voltage AC/AC electrochemical capacitor operating at low temperature in salt aqueous electrolyte. J Power Sources 2016;318:235–41.
[87] Fic K, Lota G, Meller M, Frackowiak E. Novel insight into neutral medium as electrolyte for high-voltage supercapacitors. Energy Environ Sci 2012;5:5842–50.
[88] Conway BE, Gileadi E. Kinetic theory of pseudo-capacitance and electrode reactions at appreciable surface coverage. Trans Faraday Soc 1962;58:2493–509.
[89] Fic K, Meller M, Frackowiak E. Interfacial redox phenomena for enhanced aqueous supercapacitors. J Electrochem Soc 2015;162:A5140–7.
[90] Khomenko V, Raymundo-Pinero E, Frackowiak E, Beguin F. High-voltage asymmetric supercapacitors operating in aqueous electrolyte. Appl Phys A Mater Sci Process 2006;82:567–73.
[91] Demarconnay L, Raymundo-Pinero E, Béguin F. A symmetric carbon/carbon supercapacitor operating at 1.6 V by using a neutral aqueous solution. Electrochem Commun 2010;12:1275–8.
[92] Gao Q, Demarconnay L, Raymundo-Pinero E, Beguin F. Exploring the large voltage range of carbon/carbon supercapacitors in aqueous lithium sulfate electrolyte. Energy Environ Sci 2012;5:9611–7.
[93] Ratajczak P, Jurewicz K, Skowron P, Abbas Q, Beguin F. Effect of accelerated ageing on the performance of high voltage carbon/carbon electrochemical capacitors in salt aqueous electrolyte. Electrochim Acta 2014;130:344–50.
[94] Ratajczak P, Jurewicz K, Beguin F. Factors contributing to ageing of high voltage carbon/carbon supercapacitors in salt aqueous electrolyte. J Appl Electrochem 2014;44:475–80.
[95] Laheäär A, Przygocki P, Abbas Q, Béguin F. Appropriate methods for evaluating the efficiency and capacitive behavior of different types of supercapacitors. Electrochem Commun 2015;60:21–5.
[96] Tachibana M, Ohishi T, Tsukada Y, Kitajima A, Yamagishi H, Murakami M. Supercapacitor using an electrolyte charge storage system. Electrochemistry 2011;79:882–6.
[97] Qian L, Tian X, Yang L, Mao J, Yuan H, Xiao D. High specific capacitance of CuS nanotubes in redox active polysulfide electrolyte. RSC Adv 2013;3:1703–8.
[98] Yu HJ, Wu JH, Fan LQ, Lin YZ, Chen SH, Chen Y, et al. Application of a novel redox-active electrolyte in MnO_2-based supercapacitors. Sci Chin: Chem 2012;55:1319–24.
[99] Yu H, Fan L, Wu J, Lin Y, Huang M, Lin J, et al. Redox-active alkaline electrolyte for carbon-based supercapacitor with pseudocapacitive performance and excellent cyclability. RSC Adv 2012;2:6736–40.
[100] Senthilkumar S, Selvan RK, Lee Y, Melo J. Electric double layer capacitor and its improved specific capacitance using redox additive electrolyte. J Mater Chem A 2013;1:1086–95.
[101] Sun K, Feng E, Peng H, Ma G, Wu Y, Wang H, et al. A simple and high-performance supercapacitor based on nitrogen-doped porous carbon in redox-mediated sodium molybdate electrolyte. Electrochim Acta 2015;158:361–7.
[102] Gogotsi Y, Simon P. True performance metrics in electrochemical energy storage. Science 2011;334:917–8.
[103] Chen L, Bai H, Huang Z, Li L. Mechanism investigation and suppression of self-discharge in active electrolyte enhanced supercapacitors. Energy Environ Sci 2014;7:1750–9.
[104] Weingarth D, Foelske-Schmitz A, Kötz R. Cycle versus voltage hold – which is the better stability test for electrochemical double layer capacitors? J Power Sources 2013;225:84–8.
[105] Xu K, Ding SP, Jow TR. Toward reliable values of electrochemical stability limits for electrolytes. J Electrochem Soc 1999;146:4172–8.
[106] Weingarth D, Noh H, Foelske-Schmitz A, Wokaun A, Kötz R. A reliable determination method of stability limits for electrochemical double layer capacitors. Electrochim Acta 2013;103:119–24.
[107] *Lee J, Srimuk P, Aristizabal K, Kim C, Choudhury S, Nah YC, et al. Pseudocapacitive desalination of brackish water and seawater with vanadium-pentoxide-decorated multiwalled carbon nanotubes. ChemSusChem 2017;10:3611–23.
[108] Ruch PW, Cericola D, Foelske A, Kötz R, Wokaun A. A comparison of the aging of electrochemical double layer capacitors with acetonitrile and propylene carbonate-based electrolytes at elevated voltages. Electrochim Acta 2010;55:2352–7.
[109] Andreas HA. Self-discharge in electrochemical capacitors: a perspective article. J Electrochem Soc 2015;162:A5047–53.
[110] Niu J, Conway BE, Pell WG. Comparative studies of self-discharge by potential decay and float-current measurements at C double-layer capacitor and battery electrodes. J Power Sources 2004;135:332–43.
[111] Cha SM, Nagaraju G, Sekhar SC, Yu JS. A facile drop-casting approach to nanostructured copper oxide-painted conductive woven textile as binder-free electrode for improved energy storage performance in redox-additive electrolyte. J Mater Chem A 2017;5:2224–34.
[112] Chen K, Song S, Xue D. An ionic aqueous pseudocapacitor system: electroactive ions in both a salt electrode and redox electrolyte. RSC Adv 2014;4:23338–43.
[113] Chen L, Chen Y, Wu J, Wang J, Bai H, Li L. Electrochemical supercapacitor with polymeric active electrolyte. J Mater Chem A 2014;2:10526–31.
[114] Díaz P, González Z, Santamaría R, Granda M, Menéndez R, Blanco C. Enhanced energy density of carbon-based supercapacitors using Cerium (III) sulphate as inorganic redox electrolyte. Electrochim Acta 2015;168:277–84.
[115] Sun XN, Hu W, Xu D, Chen XY, Cui P. Integration of redox additive in H_2SO_4 solution and the adjustment of potential windows for improving the capacitive performances of supercapacitors. Ind Eng Chem Res 2017;56:2433–43.

[116] Roldán S, Granda M, Menéndez R, Santamaría R, Blanco C. Supercapacitor modified with methylene blue as redox active electrolyte. Electrochim Acta 2012;83:241–6.
[117] Sathyamoorthi S, Kanagaraj M, Kathiresan M, Suryanarayanan V, Velayutham D. Ethyl viologen dibromide as a novel dual redox shuttle for supercapacitors. J Mater Chem A 2016;4:4562–9.
[118] *Su X, Hatton TA. Redox-electrodes for selective electrochemical separations. Adv Colloid Interface Sci 2017;244:6–20.
[119] Gorska B, Bujewska P, Fic K. Thiocyanates as attractive redox-active electrolytes for high-energy and environmentally-friendly electrochemical capacitors. Phys Chem Chem Phys 2017;19:7923–35.
[120] Zhang Y, Zu L, Lian H, Hu Z, Jiang Y, Liu Y, et al. An ultrahigh performance supercapacitors based on simultaneous redox in both electrode and electrolyte. J Alloy Compd 2017;694:136–44.
[121] Sankar KV, Kalai Selvan R. Improved electrochemical performances of reduced graphene oxide based supercapacitor using redox additive electrolyte. Carbon 2015;90:260–73.
[122] Roldán S, González Z, Blanco C, Granda M, Menéndez R, Santamaría R. Redox-active electrolyte for carbon nanotube-based electric double layer capacitors. Electrochim Acta 2011;56:3401–5.
[123] Lamiel C, Lee YR, Cho MH, Tuma D, Shim J-J. Enhanced electrochemical performance of nickel-cobalt-oxide@reduced graphene oxide//activated carbon asymmetric supercapacitors by the addition of a redox-active electrolyte. J Colloid Interface Sci 2017;507:300–9.
[124] Chodankar NR, Dubal DP, Lokhande AC, Patil AM, Kim JH, Lokhande CD. An innovative concept of use of redox-active electrolyte in asymmetric capacitor based on MWCNTs/MnO_2 and Fe_2O_3 thin films. Sci Rep 2016;6:39205.
[125] Shanmugavani A, Kaviselvi S, Sankar KV, Selvan RK. Enhanced electrochemical performances of PANI using redox additive of $K_4[Fe(CN)_6]$ in aqueous electrolyte for symmetric supercapacitors. Mater Res Bull 2015;62:161–7.
[126] Yu S, Yang N, Zhuang H, Mandal S, Williams OA, Yang B, et al. Battery-like supercapacitors from diamond networks and water-soluble redox electrolytes. J Mater Chem A 2017;5:1778–85.
[127] Banik SJ, Akolkar R. Suppressing dendrite growth during zinc electrodeposition by PEG-200 additive. J Electrochem Soc 2013;160:D519–23.
[128] Cheng X-B, Zhao M-Q, Chen C, Pentecost A, Maleski K, Mathis T, et al. Nanodiamonds suppress the growth of lithium dendrites. Nat Commun 2017;8:336.
[129] Bai P, Li J, Brushett FR, Bazant MZ. Transition of lithium growth mechanisms in liquid electrolytes. Energy Environ Sci 2016;9:3221–9.
[130] Higashi S, Lee SW, Lee JS, Takechi K, Cui Y. Avoiding short circuits from zinc metal dendrites in anode by backside-plating configuration. Nat Commun 2016;7:11801.
[131] Fic K, Lota G, Frackowiak E. Electrochemical properties of supercapacitors operating in aqueous electrolyte with surfactants. Electrochim Acta 2010;55:7484–8.
[132] Fic K, Lota G, Frackowiak E. Effect of surfactants on capacitance properties of carbon electrodes. Electrochim Acta 2012;60:206–12.
[133] Lota G, Milczarek G. The effect of lignosulfonates as electrolyte additives on the electrochemical performance of supercapacitors. Electrochem Commun 2011;13:470–3.
[134] Mousavi MF, Hashemi M, Rahmanifar MS, Noori A. Synergistic effect between redox additive electrolyte and PANI-rGO nanocomposite electrode for high energy and high power supercapacitor. Electrochim Acta 2017;228:290–8.
[135] Gastol D, Walkowiak J, Fic K, Frackowiak E. Enhancement of the carbon electrode capacitance by brominated hydroquinones. J Power Sources 2016;326:587–94.
[136] Zhu Y, Liu E, Luo Z, Hu T, Liu T, Li Z, et al. A hydroquinone redox electrolyte for polyaniline/SnO_2 supercapacitors. Electrochim Acta 2014;118:106–11.
[137] Vonlanthen D, Lazarev P, See KA, Wudl F, Heeger AJ. A stable polyaniline-benzoquinone-hydroquinone supercapacitor. Adv Mater 2014;26:5095–100.
[138] Nie YF, Wang Q, Chen XY, Zhang ZJ. Nitrogen and oxygen functionalized hollow carbon materials: the capacitive enhancement by simply incorporating novel redox additives into H_2SO_4 electrolyte. J Power Sources 2016;320:140–52.
[139] Nie YF, Wang Q, Chen XY, Zhang ZJ. Synergistic effect of novel redox additives of p-nitroaniline and dimethylglyoxime for highly improving the supercapacitor performances. Phys Chem Chem Phys 2016;18:2718–29.
[140] Sathyamoorthi S, Suryanarayanan V, Velayutham D. Organo-redox shuttle promoted protic ionic liquid electrolyte for supercapacitor. J Power Sources 2015;274:1135–9.
[141] Yamazaki S, Ito T, Yamagata M, Ishikawa M. Non-aqueous electrochemical capacitor utilizing electrolytic redox reactions of bromide species in ionic liquid. Electrochim Acta 2012;86:294–7.
[142] Siinor L, Siimenson C, Lust K, Lust E. Mixture of 1-ethyl-3-methylimidazolium tetrafluoroborate and 1-ethyl-3-methylimidazolium iodide: a new potential high capacitance electrolyte for EDLCs. Electrochem Commun 2013;35:5–7.
[143] Siimenson C, Siinor L, Lust K, Lust E. The electrochemical characteristics of the mixture of 1-ethyl-3-methylimidazolium tetrafluoroborate and 1-ethyl-3-methylimidazolium iodide. J Electroanal Chem 2014;730:59–64.
[144] Siimenson C, Lembinen M, Oll O, Läll L, Tarkanovskaja M, Ivaništšev V, et al. Electrochemical investigation of 1-ethyl-3-methylimidazolium bromide and tetrafluoroborate mixture at Bi (111) electrode interface. J Electrochem Soc 2016;163:H723–30.
[145] Xie HJ, Gélinas B, Rochefort D. Redox-active electrolyte supercapacitors using electroactive ionic liquids. Electrochem Commun 2016;66:42–5.
[146] Mourad E, Coustan L, Lannelongue P, Zigah D, Mehdi A, Vioux A, et al. Biredox ionic liquids with solid-like redox density in the liquid state for high-energy supercapacitors. Nat Mater 2017;16:446–53.
[147] Gong K, Fang Q, Gu S, Li SFY, Yan Y. Nonaqueous redox-flow batteries: organic solvents, supporting electrolytes, and redox pairs. Energy Environ Sci 2015;8:3515–30.
[148] Hubbard AT. Study of the kinetics of electrochemical reactions by thin-layer voltammetry. J Electroanal Chem Interfacial Electrochem 1969;22:165–74.
[149] Hubbard AT, Anson FC. Linear potential sweep voltammetry in thin layers of solution. Anal Chem 1966;38:58–61.
[150] Christensen CR, Anson FC. Chronopotentiometry in thin layer of solution. Anal Chem 1963;35:205–9.
[151] Streeter I, Wildgoose GG, Shao L, Compton RG. Cyclic voltammetry on electrode surfaces covered with porous layers: an analysis of electron transfer kinetics at single-walled carbon nanotube modified electrodes. Sens Actuat, B 2008;133:462–6.
[152] Henstridge MC, Dickinson EJF, Aslanoglu M, Batchelor-McAuley C, Compton RG. Voltammetric selectivity conferred by the modification of electrodes using conductive porous layers or films: the oxidation of dopamine on glassy carbon electrodes modified with multiwalled carbon nanotubes. Sens Actuat, B 2010;145:417–27.
[153] Keeley GP, Lyons MEG. The effects of thin layer diffusion at glassy carbon electrodes modified with porous films of single-walled carbon nanotubes. Int J Electrochem Sci 2009;4:794–809.
[154] Ward KR, Xiong L, Lawrence NS, Hartshorne RS, Compton RG. Thin-layer vs. semi-infinite diffusion in cylindrical pores: a basis for delineating Fickian transport to identify nano-confinement effects in voltammetry. J Electroanal Chem 2013;702:15–24.
[155] Liu T, Pell WG, Conway BE. Self-discharge and potential recovery phenomena at thermally and electrochemically prepared RuO_2 supercapacitor electrodes. Electrochim Acta 1997;42:3541–52.
[156] Black J, Andreas HA. Effects of charge redistribution on self-discharge of electrochemical capacitors. Electrochim Acta 2009;54:3568–74.
[157] Ricketts BW, Ton-That C. Self-discharge of carbon-based supercapacitors with organic electrolytes. J Power Sources 2000;89:64–9.
[158] Lewandowski A, Jakobczyk P, Galinski M, Biegun M. Self-discharge of electrochemical double layer capacitors. Phys Chem Chem Phys 2013;15:8692–9.
[159] Conway BE. Electrochemical supercapacitors: scientific fundamentals and technological applications. Springer US; 2013.
[160] Ike IS, Sigalas I, Iyuke S. Understanding performance limitation and suppression of leakage current or self-discharge in electrochemical capacitors: a review. Phys Chem Chem Phys 2016;18:661–80.
[161] Conway BE, Pell WG, Liu TC. Diagnostic analyses for mechanisms of self-discharge of electrochemical capacitors and batteries. J Power Sources 1997;65:53–9.
[162] Ike IS, Sigalas I, Iyuke SE. The effects of self-discharge on the performance of symmetric electric double-layer capacitors and active electrolyte-enhanced supercapacitors: insights from modeling and simulation. J Electron Mater 2017;46:1163–89.
[163] Kowal J, Avaroglu E, Chamekh F, S'enfelds A, Thien T, Wijaya D, et al. Detailed analysis of the self-discharge of supercapacitors. J Power Sources

2011;196:573–9.
[164] Pell W, Conway B. Voltammetry at a de Levie brush electrode as a model for electrochemical supercapacitor behaviour. J Electroanal Chem 2001;500:121–33.
[165] De Levie R. On porous electrodes in electrolyte solutions: I. Capacitance effects. Electrochim Acta 1963;8:751–80.
[166] Kaus M, Kowal J, Sauer DU. Modelling the effects of charge redistribution during self-discharge of supercapacitors. Electrochim Acta 2010;55:7516–23.
[167] Brownson DA, Banks CE. The handbook of graphene electrochemistry. The handbook of graphene electrochemistry. Springer; 2014. p. 23–76.
[168] Randles JEB. A cathode ray polarograph. Part II. The current-voltage curves. Trans Faraday Soc 1948;44:327–38.
[169] Ševčik A. Oscillographic polarography with periodical triangular voltage. Collect Czech Chem Commun 1948;13:349–77.
[170] *Anjos DM, McDonough JK, Perre E, Brown GM, Overbury SH, Gogotsi Y, et al. Pseudocapacitance and performance stability of quinone-coated carbon onions. Nano Energy 2013;2:702–12.
[171] Chathoth SM, Mamontov E, Dai S, Wang X, Fulvio PF, Wesolowski DJ. Fast diffusion in a room temperature ionic liquid confined in mesoporous carbon. Europhys Lett 2012;97:66004.
[172] Biesheuvel PM, Zhao R, Porada S, van der Wal A. Theory of membrane capacitive deionization including the effect of the electrode pore space. J Colloid Interface Sci 2011;360:239–48.
[173] Gao Z, Liu X, Chang J, Wu D, Xu F, Zhang L, et al. Graphene incorporated, N doped activated carbon as catalytic electrode in redox active electrolyte mediated supercapacitor. J Power Sources 2017;337:25–35.
[174] Liang Z, Wen J, Guo B, Cheng Z, Qiu Y, Xu P, et al. Improved performance of supercapacitors constructed with activated carbon papers as electrodes and vanadyl sulfate as redox electrolyte. Ionics 2016;22:1253–8.
[175] Su LH, Gong LY, Zhao Y. A new strategy to enhance low-temperature capacitance: combination of two charge-storage mechanisms. Phys Chem Chem Phys 2014;16:681–4.
[176] Zhao C, Deng T, Xue X, Chang L, Zheng W, Wang S. Development of novel and ultrahigh-performance asymmetric supercapacitor based on redox electrode-electrolyte system. Electrochim Acta 2017;231:495–501.
[177] Senthilkumar S, Selvan RK, Ulaganathan M, Melo J. Fabrication of Bi_2O_3 AC asymmetric supercapacitor with redox additive aqueous electrolyte and its improved electrochemical performances. Electrochim Acta 2014;115:518–24.
[178] Xu D, Hu W, Sun XN, Cui P, Chen XY. Redox additives of Na_2MoO_4 and KI: synergistic effect and the improved capacitive performances for carbon-based supercapacitors. J Power Sources 2017;341:448–56.
[179] Chen W, Rakhi R, Alshareef HN. Capacitance enhancement of polyaniline coated curved-graphene supercapacitors in a redox-active electrolyte. Nanoscale 2013;5:4134–8.
[180] Chen W, Xia C, Rakhi R, Alshareef HN. A general approach toward enhancement of pseudocapacitive performance of conducting polymers by redox-active electrolytes. J Power Sources 2014;267:521–6.
[181] Wang G, Liang R, Liu L, Zhong B. Improving the specific capacitance of carbon nanotubes-based supercapacitors by combining introducing functional groups on carbon nanotubes with using redox-active electrolyte. Electrochim Acta 2014;115:183–8.
[182] Tian Y, Xue R, Zhou X, Liu Z, Huang L. Double layer capacitor based on active carbon and its improved capacitive properties using redox additive electrolyte of anthraquinonedisulphonate. Electrochim Acta 2015;152:135–9.
[183] Su LH, Gong LY, Lu HT, Xu Q. Enhanced low-temperature capacitance of MnO_2 nanorods in a redox-active electrolyte. J Power Sources 2014;248:212–7.
[184] Wu J, Yu H, Fan L, Luo G, Lin J, Huang M. A simple and high-effective electrolyte mediated with p-phenylenediamine for supercapacitor. J Mater Chem 2012;22:19025–30.
[185] Nie YF, Wang Q, Yi HT, Chen XY, Zhang ZJ. Remarkable capacitive enhancement of templated carbon materials by the redox additive electrolyte of p-phenylenediamine. RSC Adv 2015;5:65100–9.
[186] Yan Y, Kuila T, Kim NH, Lee SH, Lee JH. N-doped carbon layer coated thermally exfoliated graphene and its capacitive behavior in redox active electrolyte. Carbon 2015;85:60–71.
[187] Su L, Gong L, Ma C, Wang X, Sun Z. Outstanding low-temperature capacitance of an AC–AC supercapacitor in acid redox electrolyte. ChemElectroChem 2017;4:46–8.
[188] Yu H, Wu J, Fan L, Hao S, Lin J, Huang M. An efficient redox-mediated organic electrolyte for high-energy supercapacitor. J Power Sources 2014;248:1123–6.
[189] Ban S, Zhang J, Zhang L, Tsay K, Song D, Zou X. Charging and discharging electrochemical supercapacitors in the presence of both parallel leakage process and electrochemical decomposition of solvent. Electrochim Acta 2013;90:542–9.